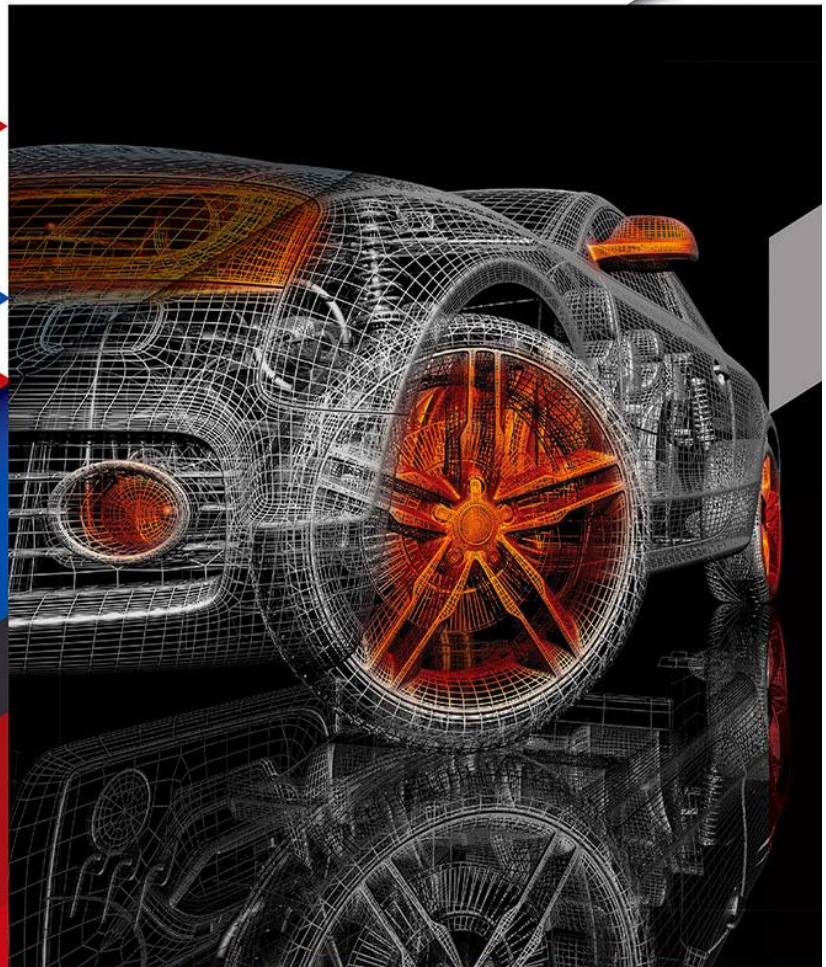




International
Journal of Automotive
Engineering and
Technologies



e-ISSN 2146-9067

e-mail: editorofijaet@gmail.com

Editor: Prof. Dr. Murat CİNİVİZ

**International Journal of Automotive
Engineering and Technologies**

e-ISSN: 2146-9067, **Period:** Quarterly

Founded: 2012, **Publisher:** Murat CİNİVİZ

Year : 2025

Volume : 14

Number : 2

<https://dergipark.org.tr/tr/pub/ijaet>



Editor in Chief

Prof. Dr. Murat Ciniviz

Editors

Prof. Dr. Murat Ciniviz

Assistant Editor

Prof. Dr. Can Haşimoğlu

Prof. Dr. Seyfi Polat

Prof. Dr. Mesut Düzgün

Assoc. Prof. Dr. Fatih Aydın

Editorial Board

SN	Editorial Board Member	University	Country
1.	Assoc. Prof. Dr. Abdul Aziz HAİRÜDDİN	Universiti Putra Malaysia	Malaysia
2.	Prof. Dr. Seyfi POLAT	Hitit University	Türkiye
3.	Prof. Dr. Habib GÜRBÜZ	Süleyman Demirel University	Türkiye
4.	Prof. Dr. Fatih AKSOY	Afyon Kocatepe University	Türkiye
5.	Prof. Dr. Ünal AKDAĞ	Aksaray University	Türkiye
6.	Assoc. Prof. Dr. Fatih AYDIN	Necmettin Erbakan University	Türkiye
7.	Assist. Prof. Dr. Mehmet DEMİRALP	Niğde Ömer Halisdemir University	Türkiye
8.	Assist. Prof. Dr. Aleksandr KABANOV	Kharkiv National Automobile and Highway University	Ukrainian
9.	Assist. Prof. Dr. Sam Dakka	University of Nottingham	United Kingdom
10.	Assist. Prof. Dr. Halil Erdi GÜLCAN	Selçuk University	Türkiye
11.	Assist. Prof. Dr. Nurullah GÜLTEKİN	Tokat Gaziosmanpaşa University	Türkiye

12.	Assoc. Prof. Dr. Sivakumar MUTHUSAMY	K.S.R. College of Engineering	India
13.	Assoc. Prof. Dr. Fuhaid ALSHAMMARI	University of Hail	Saudi Arabia
14.	Prof. Dr. Adrian CLENCI	National University of Science and Technology	Romania
15.	Assoc. Prof. Dr. Ratchagaraja DHAIRIYASAMY	Saveetha Institute of Medical and Technical Sciences, Saveetha University	India
16.	Prof. Dr. Altin DORRİ	Polytechnic University of Tirana	Albania
17.	Assoc. Prof. Dr. Mohamed R. Gomaa	Benha University	Egypt
18.	Dr. Guohong Tian	University of Surrey	United Kingdom

Language Editor

1.	DR. Öznur YEMEZ	Selçuk University	Türkiye
----	-----------------	-------------------	---------

SN	Author(s)	Article Title	Pages
1.	Muhammet Emre Uçak ^{1*} , Abdulkadir Cengiz ²	Independent front suspension lower control arm design with topology optimization approach for electric light-duty vehicle	77 - 85
2.	Aslı Abdulvahitoğlu ^{1*} , Nurten Cengiz ²	Evaluation of Prunus insititia L. Oil: characterization and its potential as a sustainable biodiesel feedstock	86 – 97
3.	Ceyla Güngör ^{1*}	Application of RSM for prediction and optimization of performance and emissions of diesel engine fuelled with butanol-diesel blends	98 - 109
4.	Ali Can Yılmaz ^{1*} , Özlem Erdem Yılmaz ²	Correlation between spark plug electrode gap and engine performance-emission characteristics in a single-cylinder petrol engine	110 – 122
5.	Murat Onat ^{1*}	Investigation of changes in body-in-white components and their impact during the transition from internal combustion engine vehicles to electric vehicles	123 - 141



e-ISSN: 2146 - 9067

International Journal of Automotive Engineering and Technologies

journal homepage:

<https://dergipark.org.tr/en/pub/ijaet>



Original Research Article

Independent front suspension lower control arm design with topology optimization approach for electric light-duty vehicle



Muhammet Emre Uçak^{1*}, Abdulkadir Cengiz²

^{1*} Graduate School of Natural and Applied Sciences, Department of Automotive Engineering, Kocaeli University, Türkiye.

² Faculty of Technology, Department of Automotive Engineering, Kocaeli University, Türkiye.

ARTICLE INFO

Orcid Numbers

1. 0009-0005-3354-1668

2. 0000-0002-7830-5299

Doi: 10.18245/ijaet.1561823

* Corresponding author
muhammetemreucak@gmail.com

Received: Oct 05, 2024

Accepted: Apr 13, 2025

Published: 30 Jun 2025

Published by Editorial Board Members
of IJAET

© This article is distributed by Turk
Journal Park System under the CC 4.0
terms and conditions.

To cite this paper: Uçak, M.E., Cengiz, A., Independent front suspension lower control arm design with topology optimization approach for electric light-duty vehicle, International Journal of Automotive Engineering and Technologies. 2025, 14 (2), 77 – 85. <http://dx.doi.org/10.18245/ijaet.1561823>

ABSTRACT

750 kg load-carrying capacity and, 1000 kg towing capacity of a two-wheel drive, two-axle electric light-duty vehicle with double wishbone independent front suspension has been designed using a topology optimization approach. For this purpose, firstly, the kinematic model of the suspension system and steering system was developed using the multi-body dynamics approach. Using this model, the force and moment values acting on the connection points were defined separately for the quasistatic load cases mentioned in the literature such as braking, cornering, bumping and brake in cornering. In the second step, a preliminary design model of the lower control arm was created, considering the defined positions of the wheel sweep volume, the suspension spring and the brake system components. In the third step, structural static analysis was performed for each load case and the results obtained were used as inputs for topology optimization. This allowed for the identification of non-load-bearing volumetric elements for each load case. In the fourth stage, the volumetric structures obtained from the topology optimization studies were overlaid at the same coordinates, and a manufacturable solid model of the swing arm was designed using reverse engineering. In the final stage, structural static analysis was performed to verify the final design and calculate the minimum safety factor. As a result of the optimization study for the swing arm, planned to be manufactured using 6061-T6 aluminum alloy, a product with 46% less weight and a safety factor of 1.21 was achieved.

Keywords: Electric Light-Duty Vehicle, Multi-Body Dynamics, Quasistatic Load Types, Structural Static Analysis, Topology Optimization.

1. Introduction

The suspension system is one of the critical components of a vehicle, providing the connection between the chassis and the wheels while optimizing ride comfort and handling. These systems absorb vibrations and shocks caused by irregularities in the road surface, improving comfort for both the driver and

passengers [1,2].

It also maintains the vehicle's stability when cornering and ensures continuous wheel-to-road contact during braking [1]. Suspension systems are divided into two main categories: rigid and independent. Both categories have their own advantages and disadvantages.

Figure 1 illustrates the main difference

between rigid and independent suspension when encountering a one-sided bump in the road. With dependent or rigid axles, the movement of one wheel affects the other. However, with independent suspension, the movement of one wheel does not affect the other [1, 2].

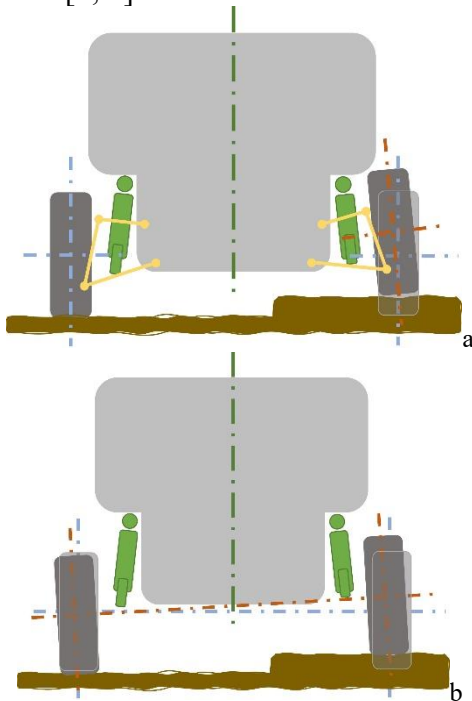


Figure 1 Types of suspension systems a) Independent suspension system b) Rigid axle suspension system

The double wishbone independent suspension system is the preferred choice of electric vehicle manufacturers who wish to differentiate their vehicles through competitive features. These features include a lower installation volume, and mass compared to rigid axle suspension systems, as well as providing minimalist, comfortable, and economical driving experience.

An example of an independent suspension system featuring a double wishbone design and helical springs applied to an electric light-duty vehicle is shown in Figure 2. This study focuses on the structural design of the double wishbone independent front suspension's lower control arm for a two-wheel drive, two-axle electric light-duty vehicle, utilizing topology optimization.

In this context, a half-vehicle model was first constructed using the MSC Adams/Car™ software package, taking the previously determined kinematic connection points of the vehicle, suspension, and steering systems as references.

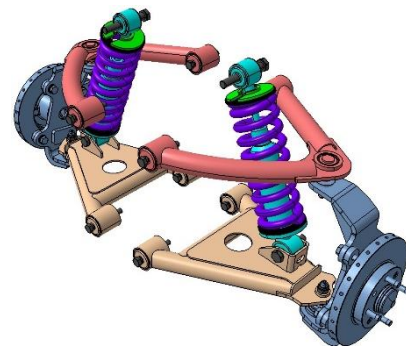


Figure 2 Double wishbone independent suspension system of an electric light-duty vehicle

Considering the literature and field knowledge gained from years of research on suspension systems, the model was simulated based on quasistatic load types, and the highest force values occurring at the connection points of the lower control arm were calculated separately. Subsequently, to create a design volume, lower control arm models available in the market were examined. A preliminary design of the lower control arm was modeled using Catia V5® CAD software, taking into account the connection points of the lower control arm, the volume swept by the wheel, and the system elements connected to the wheel during steering. Using the previously calculated force and moment values, the non-load-bearing elements of the CAD model were identified through topology optimization in ANSYS® Workbench for each load case.

The obtained volumes were overlapped using the Catia V5® Digitized Shape Editor module, resulting in a new and manufacturable lower control arm design that meets the requirements of all driving conditions through a reverse engineering method. To verify the structure, the previously calculated loading conditions were applied again, and the minimum safety factor of the part was determined through structural analysis.

This study aims to perform structural optimization of the lower control arm structure intended for use in an electric light-duty vehicle with a double wishbone independent front suspension, focusing on achieving minimum weight and maximum stiffness based on various analysis outputs.

2. Materials and Methods

In this study, a topology optimization approach is used for the optimal design of the lower control arm in a double wishbone independent

suspension system. The fundamental concept of topology optimization, which allows for obtaining the optimal structural model at the beginning of the design process, is based on the principle of removing certain non-load-bearing regions without altering the connection points of the part to be optimized and without disturbing the stiffness of the structure.

In simpler terms, topology optimization is the process of searching for the optimal material distribution that maximizes stiffness [3,4].

The stages of the optimal design of an embedded beam with specified loading and boundary conditions using the topology optimization approach are illustrated in Figure 3.

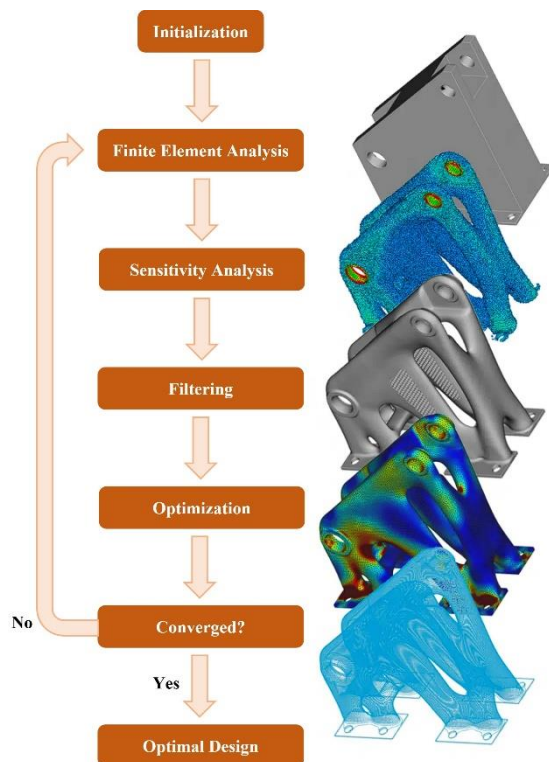


Figure 3 Flowchart of topology optimization based on SIMP method

The SIMP method is widely used approach in topology optimization because it is easy to implement and produces efficient results and it can be formulated as follows (1).

$$E(\rho) = \rho^P E_0 \quad (1)$$

$E(\rho)$ is the modulus of elasticity calculated based on the density ρ . This approach represents the material distribution in the design volume by a density variable (ρ). The material distribution is expressed by the values 0 (empty) and 1 (full). The rigidity is determined by interpolation using (ρ) and the

penalization factor (P) is used to ensure sharp separation between filled and empty regions. Higher values of (P) iteratively force the intermediate densities to values of 0 or 1, creating a distinct material distribution [5,6]. However, the SIMP method is sensitive to the mesh size and may result in angular and non-fabricated surfaces. Therefore, post-optimization surface refinement processes are required.

After establishing the kinematic analysis model to determine the geometric conditions and dimensional values required for topology optimization and to control system operation, analyses should be performed according to various case scenarios to determine the dynamic loads. For this purpose, the following section headings should be applied in order.

2.1. Multi-body dynamics modelling

Before the kinematic model of the suspension system can be constructed, the structure in question must be described in general terms. This description aims to identify the structural elements and their mechanical relationships with one another. In this context, Figure 4 illustrates a simple kinematic model of a double wishbone suspension system [7].

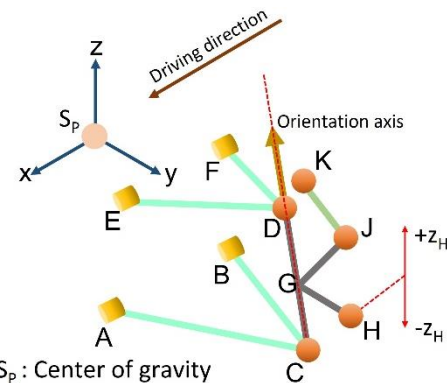


Figure 4 The kinematic model of the suspension system

Accordingly, the suspension system is connected to the vehicle body by revolute joints at points A, B and E, F. Points C and D indicate the connections of the upper and lower control arms to the axle. These two points are commonly referred to as spherical joints, allowing the wheels to translate along the z-axis and rotate around the C-D axis. The C-D axis is also described in literature as the kingpin axis. Point G defines the hub center, while point H defines the wheel center, both of

which are fixed components.

When the vehicle is subjected to different driving conditions, the wheels are compelled to move vertically, resulting in changes to the caster angle of the wheels. Since it is known that this change in caster angle directly affects handling, comfort, and the service life of the system components, efforts are made to minimize these changes.

In Reimpell's publication, the structure illustrated in Figure 5 describes the positioning of the tie rod attachment points [J-K] in double wishbone suspension systems. It provides guidance on how to position the tie rod in scenarios where the control arms are parallel. This drawn axis represents the position of the tie rod. To determine the position of point K, another axis must be created that passes through the virtual center P_2 and is parallel to the tie rod axis [8]. When the control arms are parallel to each other, the steering center (P_1) is in infinity. In this case, to determine the attachment points of the tie rod, another axis must be drawn parallel to the [C-A, B] axis, originating at point J. Additionally, another set of axes must be drawn, passing through the virtual center P_2 and equal to the distance between these two axes. The intersection of this second parallel with the extension of the path [J-D] yields point P_3 , which must be connected to C to obtain point K [8].

To summarize, when designing a system with parallel suspension arms, the tie rod should be positioned parallel to these arms [8]. Additionally, a spherical joint is defined at point J, and a cardanic joint is defined at point K.

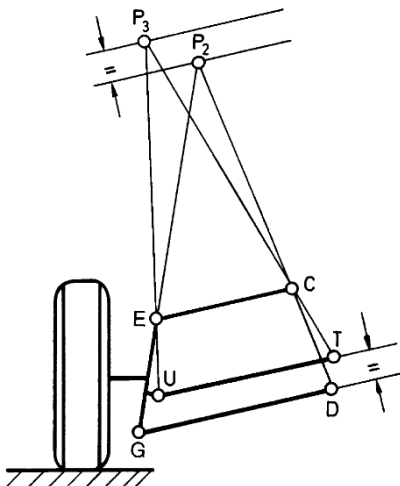


Figure 5 Determination of tie rod connection points [8]

After determining all the physical boundary conditions required for the multi-body dynamics model of the system, the suspension system model was created using the MSC Adams/Car™ software package, as shown in Figure 6, to calculate the forces acting on the connection points of the lower control arm. To enhance the accuracy of the force values acting on the structure, the vehicle's steering system was also modeled and incorporated into the half-vehicle model.

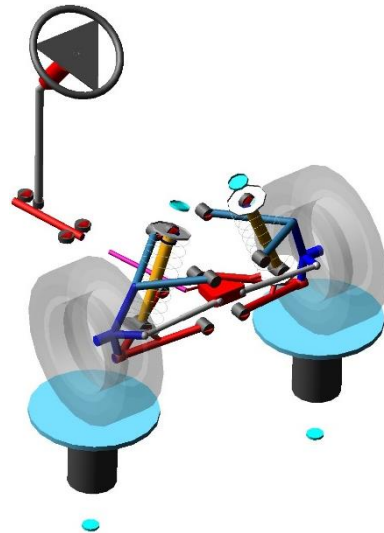


Figure 6 Half-vehicle model

2.2. Determination of loads

Since wheel loads are often unavailable at the early stages of vehicle design or can only be measured on prototypes, the acting loads can be derived from standard driving conditions. These driving conditions are defined as quasistatic and are assumed to be time independent. Many vehicle manufacturers utilize these standard loads, which share similar values.

While these loads are generally expressed as force and moment values, they can also be found in literature in the form of wheel accelerations [1].

To determine the loads acting on the swing connection points, quasistatic standard load types, as defined in the literature, were revised to be suitable for the electric light-duty vehicles discussed in this article. These revised values are based on years of experience with electric vehicles.

Among these load types, four basic load types that are important in the swing development phase were utilized. The acceleration values of

these load types are presented in Table 1 in terms of multiples of gravitational acceleration.

Table 1 Quasistatic load type

No	Load Type	Component of Acceleration (g)		
		X	Y	Z
1.	Bumping	0	0	3
2.	Braking	1	0	1
3.	Cornering	0	0.5	1
4.	Break in Cornering	0.8	0.5	1

The determined acceleration components were applied to the multi-body dynamics model created in the MSC Adams/Car™ program over a duration of 10 seconds and 100 steps, based on the selected vehicle speed. Consequently, the highest force and moment values were determined for points A, B, and C of the lower control arm under loading conditions such as bumping (1), braking (2), cornering (3), and brake in cornering (4), as shown in Table 1. The half-vehicle model obtained in the bumping (1) scenario is illustrated in Figure 7.

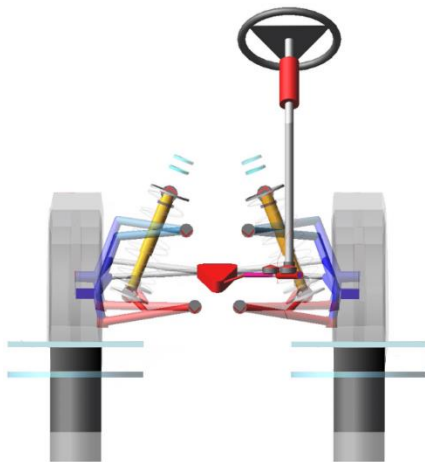


Figure 7 Half vehicle model obtained in the bumping scenario

2.3. Preliminary design

Some volumetric constraints are necessary during the preliminary design phase of the lower control arm. These constraints include positions A, B and C, which represent the connection points of the swing to the vehicle and the axle, as well as the connection point for the shock absorber group, as illustrated in Figure 4.

Additionally, the bushing bearings suitable for the diameter values of the bushings planned for

use in the swing and the thickness of the swing body needed to accommodate these bearings were also determined.

As illustrated in Figure 8, the location of the shock absorber was determined to be as close to the center of the swing as possible, taking into account the packaging of the system elements and the dimensions of the swing. Additionally, point L_1 was moved closer to the spherical joint (C) to ensure that the structure operates under reduced load.

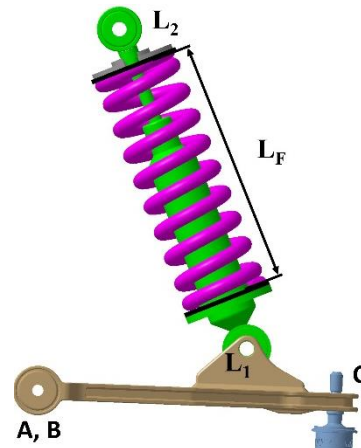


Figure 8 Positioning of the shock absorber

After applying the attachment points to the preliminary design, the external geometry of the swing was developed. The necessary constraints for this process include the area swept by the wheel during full right and left rotation (sweep volume), as well as the dimensions and positions of the structural elements of the braking system.

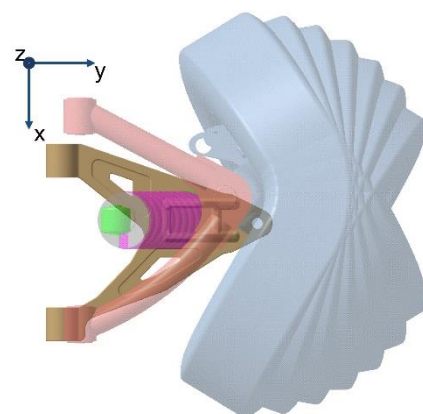


Figure 9 Wheel sweep volume

For this purpose, the steering and suspension system model of the vehicle, created in the Catia V5© software, was executed to determine the sweep volume of the wheels. A representative visualization of the sweep volume is presented in Figure 9 [7-8].

Additionally, the structural elements of the braking system intended for use in the vehicle were positioned in the Catia V5[®] software to avoid interference with the external geometry of the swing.

Given that the designed swing will be installed on an electric service vehicle, it is essential for it to be both lightweight and cost-effective. Since the vehicle in question is not a mass-produced product, unit cost is of secondary importance. Consequently, it was decided to use aluminum alloy due to the weight advantages it offers.

It was decided to utilize 6061-T6 aluminum alloy due to its excellent machinability, weldability, high corrosion resistance, and significantly lighter weight compared to steel. The material properties, including the modulus of elasticity (E), Poisson's ratio (ν), tensile strength, yield strength, and elongation at break, are presented in Table 2.

Table 2 Mechanical properties of 6061-T6 [9]

Material Property	Value
Modulus of Elasticity (GPa)	68.9
Poisson's Ratio (%)	3.3
Tensile Strength (MPa)	310
Yield Strength (MPa)	276
Density (kg/m ³)	2700

Figure 10 illustrates the preliminary design of the lower control arm, which will be optimized using the topology optimization approach. The material to be used, the outer boundaries of the structural volume, and the connection points have been established. The weight of the preliminary design structure was measured at approximately 3.7 kg.

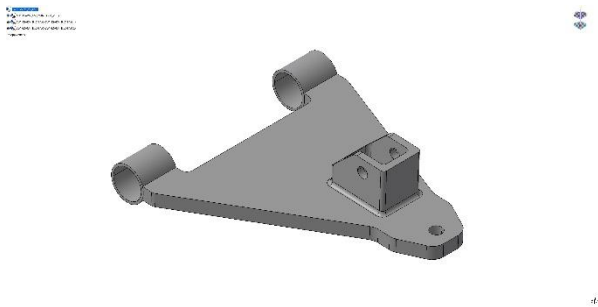


Figure 10 Preliminary design of lower control arm

Finite element analysis will be conducted on the structure using the bearing forces obtained from the multibody dynamics analysis. For this process, the structure must be divided into meshes within the ANSYS[®] Workbench environment. The finite element model created

in ANSYS[®] Workbench is illustrated in Figure 11.

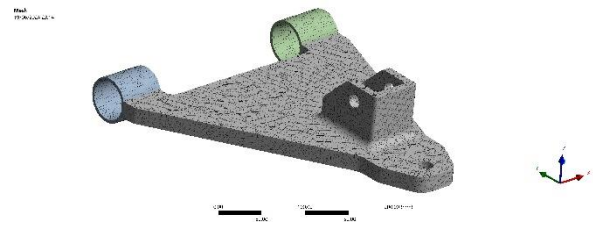


Figure 11 Finite element analysis model

3. Results and Discussion

3.1. Topology optimization

Using the topology optimization approach, the mesh quality of the model created for the lower control arm structure designed to reduce weight while maintaining adequate strength is presented in Figure 12.

The average mesh quality is evaluated at 0.82. Element quality ranges from 0 to 1, with values closer to 1 indicating superior element quality [10].

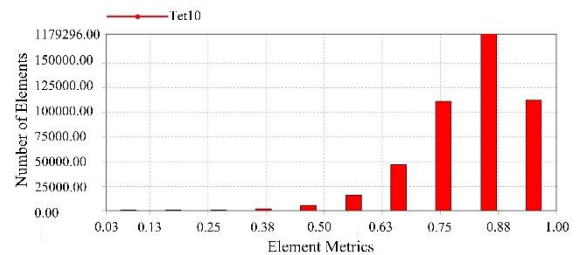


Figure 12 Element quality

As shown Figure 13, revolute joints were defined on the meshed structure to allow only rotational movements at regions A and B. In region C, the load values obtained from the multibody dynamics analysis were applied as specified in Table 1. To simulate the shock absorber system, a spring was defined in the L₁' region using the connections tab.

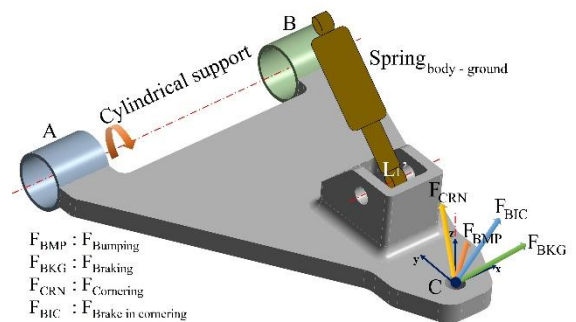


Figure 13 Defining loads and constraints

In the model, the highest equivalent stress value occurs in the bumping scenario (1), with $\sigma_{vmax}=200.23$ MPa, as shown in Figure 14. Considering the yield strength value given in

Table 2, it is seen that the preliminary design is safe. However, the equivalent stress results also indicate the presence of volumetric elements within the structure that either do not carry load or carry minimal load.

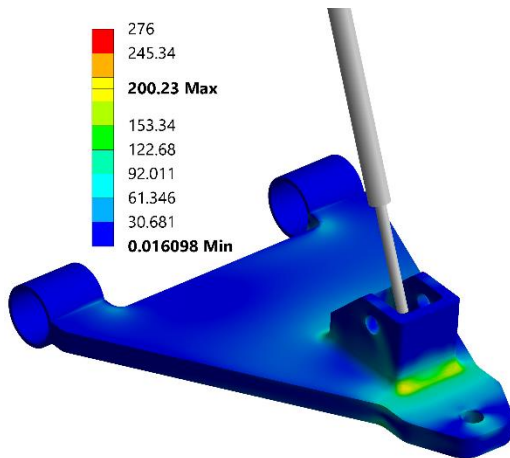


Figure 14 Preliminary design equivalent stress result (Scenario 1)

Lightweight design and low production costs, both crucial for electric vehicles, necessitate the use of minimal materials. As a result, all components that can be optimized for weight are thoroughly evaluated. In this context, the material redundancy in the lower control arm's preliminary design, as shown in Figure 10, was identified using a topology optimization approach. These optimization processes were performed using the structural optimization module in ANSYS® Workbench.

Static structural analyses were performed separately for each loading condition, after which the model was linked to the structural optimization model in ANSYS® Workbench. The first step in this process is to define the design region, where material will be removed, and the exclusion regions, where material must be preserved, such as areas with bearings. The bearings located in regions A, B, C, and L₁' in Figure 15 are defined as exclusion regions, meaning topology optimization will not be applied to these areas.

The results for the swing structure, where topology optimization was performed separately for each loading condition based on the boundary conditions, are shown in Figure 16. The topology results generated for each loading condition were then superimposed in Catia V5®, and the final design was optimized using the reverse engineering method in the Digitized Shape Editor module.

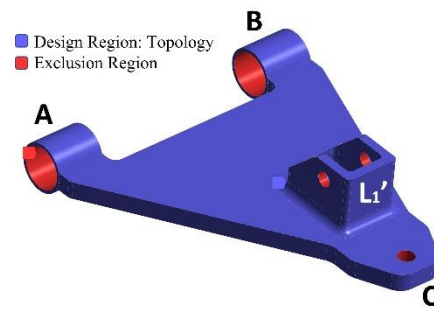


Figure 15 Design and exclusion region

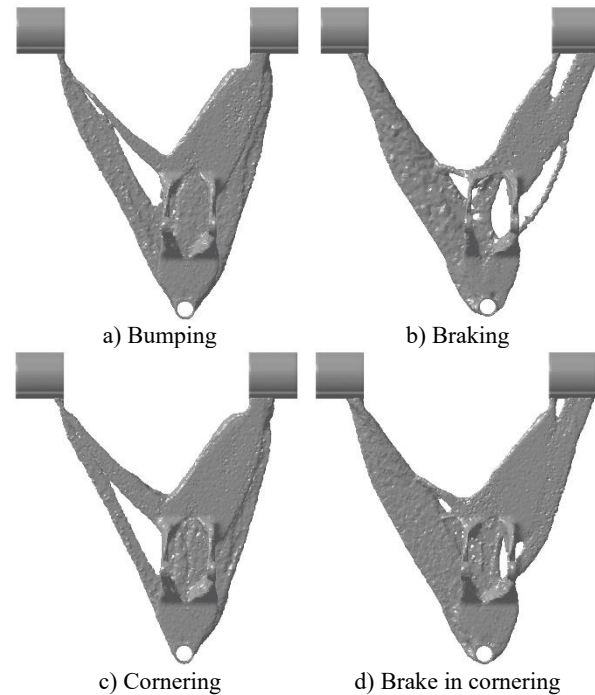


Figure 16 Topology optimization results for quasistatic load type

Necessary clearances were made on the structure, and its form was reshaped according to the topology results. The weight of the structure was measured at approximately 2 kg, resulting in a structure that is about 46% lighter than the model prepared in the preliminary design phase. The final design is shown in Figure 17.

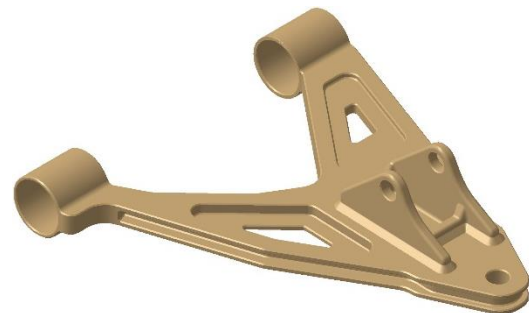


Figure 17 Final design

To verify the final design, finite element analyses were conducted for each load type listed in Table 1.

The results of these analyses are shown in Figure 18. The highest equivalent stress on the swing occurs under the first load type, corresponding to the bumping scenario with a vertical acceleration of 3g, as in the initial analysis.

The highest equivalent stress value obtained is 228.45 MPa, which is approximately 83% of the yield strength given in Table 2. The factor of safety is calculated as $S=1.21$.

4. Conclusions

In this study, the design of the lower control arm for the double wishbone independent front suspension system of an electric light-duty vehicle was conducted using a topology optimization approach. Finite element analyses were repeated to validate the resulting solid model, and it was determined that the most mechanically challenging loading condition was the bump jump at 3g vertical acceleration. The maximum equivalent stress value obtained, 228.45 MPa, was compared to the yield strength of the 6061 T6 material planned for the structure, resulting in a safety factor of $s=1.21$. In the final design, a weight reduction of approximately 46% was achieved compared to the preliminary design. The model, prepared based on four key driving conditions used in the design of the control arm, can evolve into different configurations for varying driving scenarios. Furthermore, it is critical to investigate potential fatigue damage, as vehicle suspensions are primary structures that directly impact driving safety and operate under repetitive loads. A fatigue analysis using road inputs will be possible in further studies.

Acknowledgements

The authors would like to thank CDMTech Engineering Solutions and Kocaeli University for their licensed software support.

CRedit authorship contribution statement

Muhammet Emre Uçak: Conceptualization, Investigation, Software (CAD modeling, FEA and MBD analyses), Formal analysis, Visualization, Writing – original draft, Writing – review & editing, Lead author. Abdulkadir Cengiz: Conceptualization, Supervision, Writing – review & editing.

Declaration of Competing Interest

The authors declare that they have no known competing financial interests or personal relationships that might appear to have influenced the work reported in this article.

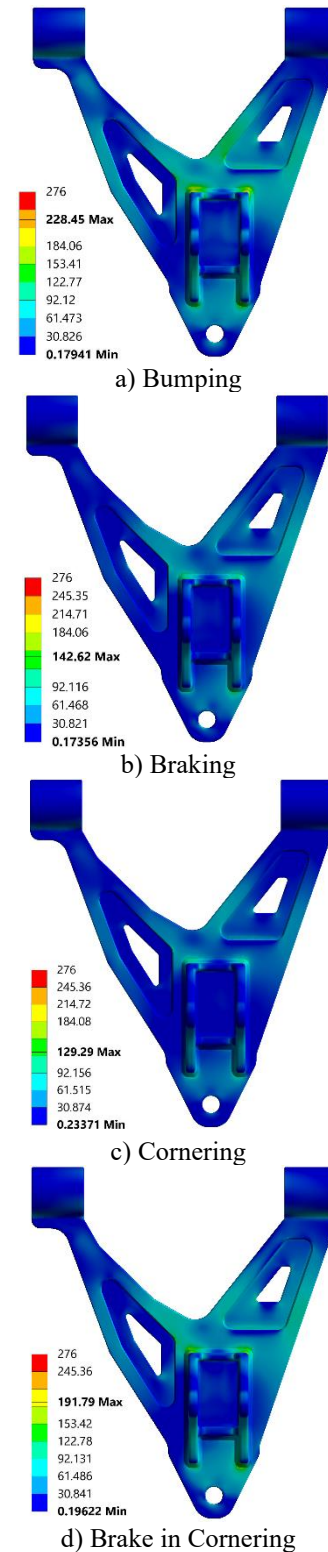


Figure 18 Validation Analysis

5. References

1. Heißing, B., Ersoy, M., Gies, S., "Fahrwerkandbuch, Grundlagen,

Fahrdynamik, Komponenten, Systeme, Mechatronik”, Vieweg+Teubner Verlag-Springer Fachmedien Wiesbaden GmbH, 2011.

2. Güler, D., “Dynamic Analysis of Double Wishbone Suspension”, Master of Thesis, İzmir Institute of Technology, 2006.

3. Bendsøe, M.P., Sigmund, O., “Topology Optimization, Theory, Methods And Applications”, Springer, 2003.

4. Christensen, P.W., Klarbring, A., “An Introduction to Structural Optimization”, Springer, 2009.

5. Kip, M., Gören, A., “Topology Optimization Study for Rear Swing Arm of a Lightweight Solar-Powered Vehicle”, Journal of Science, Technology and Engineering Research, 42-49, 2022.

6. Botsalı, H., “Design for Additive Manufacturing of Automotive Components Via Topology Optimization”, Master of Thesis, Karabük University, 2022.

7. Topaç, M.M., Bahar, E., “Design of a Lower Wishbone for a Military Vehicle Independent Front Suspension Using Topology Optimization”, IDEFIS 2017, 2nd International Defence Industry Symposium, 333-342, 2017.

8. Reimpell, J., Stoll, H., Betzler, J.W., “The Automotive Chassis: Engineering Principles”, Butterworth-Heinemann, 2001.

9. <https://asm.matweb.com/search/SpecificMaterial.asp?bassnum=MA6061t6>, 28/06/2025.

10. https://ansyshelp.ansys.com/public/account/secured?returnurl=/////Views/Secured/corp/v242/en/wb_msh/msh_Element_Quality_Metric.html, 28/06/2025.

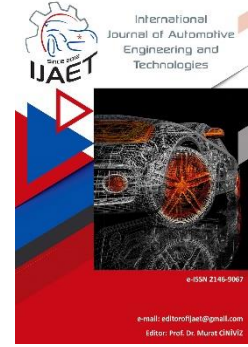


e-ISSN: 2146 - 9067

International Journal of Automotive Engineering and Technologies

journal homepage:

<https://dergipark.org.tr/en/pub/ijaet>



Original Research Article

Evaluation of *Prunus insititia* L. Oil: characterization and its potential as a sustainable biodiesel feedstock



Aslı Abdulvahitoğlu ^{1*}, Nurten Cengiz ²

¹*Engineering Faculty, Mechanical Engineering Department, Adana Alparslan Türkeş Science and Technology University, Türkiye.

²Engineering Faculty, Food Engineering Department, Adana Alparslan Türkeş Science and Technology University, Türkiye.

ARTICLE INFO

Orcid Numbers

1. 0000-0002-3603-6748

2. 0000-0002-6640-4927

Doi: 10.18245/ijaet.1604765

* Corresponding author
aabdulvahitoglu@atu.edu.tr

Received: Dec 20, 2024

Accepted: Apr 13, 2025

Published: 30 Jun 2025

Published by Editorial Board Members of
IJAET

© This article is distributed by Turk Journal
Park System under the CC 4.0 terms and
conditions.

To cite this paper: Abdulvahitoğlu, A,
Cengiz, N., Evaluation of *prunus insititia*
l. Oil: characterization and its potential
as a sustainable biodiesel feedstock,
International Journal of Automotive
Engineering and Technologies. 2025, 14
(2), 86 – 98.

<http://dx.doi.org/10.18245/ijaet.1604765>

ABSTRACT

Long-term development and economic growth are closely related to energy. The economy is negatively impacted by any changes in the energy supply. If the energy is consistent, clean, and of a quality that can satisfy the demands of several sources, supply security can be achieved. Nowadays, biofuels made from biomass provide a variety of choices. For many years, research has been conducted on biofuels that can be transformed into liquid fuel. In this situation, biodiesel—which may be used in place of diesel fuel—becomes essential. To lessen dependency on fossil fuels and edible feedstocks, the core purpose of this assessment is to demonstrate the biodiesel potential of *Prunus insititia* L. by describing the oil's composition and predicting the fuel's qualities. The predominant fatty acids found in *Prunus insititia* kernel oil were oleic acid (61.687 %w), linoleic acid (21.405 %w), palmitic acid (5.965 %w), and stearic acid (1.450 %w). The cetane number, flash point, cold flow characteristics, and oxidation stability all fell within the acceptable ranges of EN14214. However, the density and viscosity were computed to be 5.93% and 0.542% lower, respectively, than the standard's minimal values. These results suggest that *Prunus insititia* kernel L. might be a viable option for producing biodiesel.

Keywords: *Prunus insititia* L., fatty acid, biodiesel, fuel property, characterization.

1. Introduction

The world's energy need has been increasing not only from industrialization but also from the humankind population. Many predictions were made on fossil fuel resources and predictions showed that resources are depleted. Even though the global energy supply has grown by 2.6 times during the past 47 years, fossil fuels, particularly oil, have remained dominant in the energy mix [1]. On the other

hand, it has been a goal to reduce the harmful emissions of fossil fuels both to human health and the environment while meeting the energy need. In this context, renewable alternative fuels have been turned towards and biofuels seem to be a suitable solution for internal combustion engines.

For a long time, biodiesel has been utilized as a diesel fuel substitute. Biodiesel is unique in that cause oil can be obtained from a variety of sources. Biodiesel, a methyl-ester of long-

chain fatty acids, is one of these alternative biofuels [2-4]. It is biodegradable and non-toxic [5] has qualities similar to fossil diesel and may be utilized in internal combustion engines without modification. The composition of the oil used as feedstock is related to the overall fuel qualities of biodiesel [6]. Oils may be subdivided into numerous subcategories, such as edible oils (such as soybean, corn, sesame, and palm), inedible oils (such as rubber seed and pongamia), waste frying/recycled oils, animal fats, and macroalgae, all of which can be used to produce biodiesel. [7-10]. For decades, biodiesel has been evaluated as a substitute for diesel fuel. Biodiesel can be produced in four different ways. Processes include thermal cracking, blending, microemulsions, and transesterification [11]. Since it can be used in engines without any changes, biodiesel has long been a powerful alternative fuel in our lives. Many countries have used biodiesel with various regulations they have implemented. According to BP Statistical Review of World Energy 2022, global total biodiesel production in 2021 was 734 thousand barrels of oil equivalent per day, with consumption at 787 thousand barrels of oil equivalent per day [12]. According to a recent FAO analysis, international prices for oilseeds and associated goods have risen dramatically in recent months, reflecting tighter market circumstances. The COVID-19 scenario, as well as meteorological circumstances in South America and Southeast Asia (especially in light of the next La Niña cycle), international trade regulations, mineral oil prices, and the future direction of national biodiesel initiatives, are projected to impact oil crops prices [13]. However, the possibility of a problem related to the food supply in plant-based production has emerged and biodiesel production from non-edible oils has grown in popularity. Many alternatives have been explored in this context such as *Jatropha*, *Karanja*, *Mahua*, *Bay laurel*, *Neem*, *Eucalyptus*, *Sisymbrium irio*, *Linseed*, *Watermelon seed*, *Rubber seed*, *Polanga*, *Sisymbrium Sophia*, *Yellow oleander* etc [14-16].

In the literature, scientists concentrated on examining alternative feedstocks, performance

characteristics, optimal mixes, and additive effects. Dmytryshyn et al. [17] evaluated a variety of feedstocks, such as processed and unprocessed waste frying oil, Canola oil, and green seed oil. The largest yield was reported to be from canola oil. The physicochemical features of canola methyl ester and green seed methyl ester are quite similar to those of petrodiesel fuel. They advocated utilizing a lubricity improver while running with green seed biodiesel to protect the engine because it has a low lubricity feature. Rao et al. [18] used an electrical dynamometer to conduct testing on a single-cylinder, 4-stroke, naturally aspirated air-cooled diesel engine and found that *jatropha* methyl ester and its blends had a shorter ignition delay, maximum heat release rate, and combustion duration. Apart from NO_x, other exhaust pollutants were reduced when biodiesel was used instead of diesel. In a four-cylinder, four-stroke direct injection diesel engine with water cooling, Mbarawa [19] tested clove stem oil and diesel mixtures with a proportion of 25 and 50. There was a modest reduction in power, an increase in SFC, and a drop in bte. The amount of CO and HC emissions in the smoke was dramatically reduced. The amount of NO_x emitted rose dramatically, notably in the 50 % mixture. The FA content of a variety of vegetable oil was studied by Ramos et al. [20]. They discovered that increasing the length of the carbon chain and lowering unsaturation, increased cetane number and oxidation stability. Puhan et al. [21] evaluated the methyl ester of linseed oil in a steady state direct injection diesel engine with fuel injection pressures that vary 200, 220 and 240 bar respectively. The optimal injection pressure was discovered to be 240 bar, and thermal efficiency was comparable to diesel at this pressure. CO, HC, and smoke emissions fell; however, NO_x emissions rose. Two distinct solvent types (n-hexane and n-heptane) were studied by Abdulvahitoglu and Aydin [22] as additions to enhance the viscosity and cold flow characteristics of rapeseed biodiesel. Blends containing 5% to 10% alkenes were found to have fuel characteristics that were close to the typical limits of diesel fuel standard EN 590, meaning that they may be used directly in diesel engines. Simsek et al [23] stated that Petroselinic acid which is

(68.5% by weight) is an uncommon fatty acid found in coriander (*Coriandrum sativum*) that has not been identified as a significant component in biodiesel fuels. Methyl ester of *Coriandrum sativum* seed oil was shown to exhibit exceptional oxidative stability, a distinct fatty acid content, and qualities appropriate for diesel engines, meeting ASTM D6751 and EN 14214 criteria. The effects of FAME content and biodiesel physicochemical qualities on engine performance and emissions are investigated by Ruhul et al. [24]. Blends of *Jatropha curcas*, *Calophyllum inophyllum*, and palm biodiesels were studied. In the case of biodiesel blends reduction in brake, power was found. There was a decline in the emissions of Hydrocarbon and Carbon monoxide, on the contrary, NO_x emissions inclined. Abdulvahitoglu and Tüccar [5] assessed the suitability of watermelon seed oil biodiesel (WMB) as a fuel for diesel engines. Tests were conducted on different fuel characteristic values. The results of engine performance tests showed that using WMB lowered pollution levels while somewhat lowering the test engine's torque and brake power ratings. The ester of watermelon seed oil is suggested as a feasible substitute fuel additive for diesel fuel due to its ecologically friendly combustion profile. Devarajan and Selvam evaluated *Sterculia foetida* oil as a sustainable biodiesel feedstock. Using a two-step catalytic process, it achieves a 95.2% conversion rate. Biodiesel blends reduce emissions, including 2.3% CO, 4.1% HC, and 1.9% smoke, highlighting its eco-friendly potential and viability [25]. AlYammahi et al. evaluate *Salicornia* species as sustainable biodiesel feedstock for hypersaline coastal regions. *S. bigelovii* showed superior oil content (20.6 wt%) and yield potential (11,442 kg/ha), surpassing traditional feedstocks. Both species met ASTM D6751 and EN 14214 standards, with advanced analyses revealing valuable insights for future breeding. The findings highlight *Salicornia*'s potential as a high-yield, salt-tolerant crop for sustainable energy on marginal lands [26]. Rajesh et al. [27] studied Coconut fatty acid distillate (CFAD) for biodiesel production. Engine tests revealed that the performance of B20 is closer to that of diesel but emits more nitrogen oxide. They

concluded that CFAD is a promising source. Phillip and Saini emphasized waste cooking oils (WCOs) and waste animal fats (WAFs) as viable biodiesel feedstocks, highlighting their potential despite challenges. They suggest that transesterification is the predominant method for biodiesel production [28]. Emmanouilidou et al compared biodiesel from uncooked sunflower oil and waste cooking oils, finding similar properties that meet EN 14214 standards. However, oxidation stability and viscosity were often outside specified limits, highlighting the impact of feedstock type on biodiesel performance [29]. Khan and Long evaluated six non-edible seed oils, revealing oil contents of 17-51%. Biodiesel quality metrics included viscosity (2.9-5.7), density (868-910), cetane number (49-58), and flashpoint (137-187), indicating favorable properties for biodiesel production from these feedstocks [30].

According to data from the Turkish Institute of Standards, there are 5,524,915 diesel-powered vehicles on the road in Turkey, while the number of gasoline-powered vehicles is 4,819,942 [31]. Diesel vehicles accounted for 34.45 percent of all vehicles on the road. Diesel is widely used as a fuel in Turkey's transportation industry. The Turkish economy is heavily influenced by diesel prices. Concerns about the impacts of climate change and exhaust pollutants on human health, as well as the need to reduce costs as an oil-importing country, have pushed biodiesel research to the forefront. The Turkish Energy Market Regulatory Authority, on the other hand, has implemented diesel-biodiesel blending (at a rate of 7%) through a regulation dated 1.1.2018 [31].

A search on the Web of Science Core Collection with "Biodiesel" as the topic and "fuel property" and "fatty acid" as author keywords returns 7,363 results. This indicates extensive research on biodiesel properties, including cetane number, cold filter plugging point, and other fuel characteristics, often emphasizing engine performance and exhaust emissions, as depicted in Figures 1 and 2 below.

Figure 1 illustrates the keywords utilized in the search, emphasizing "Biodiesel," "Fuel properties," and "fatty acid" as the main terms

used to access relevant literature.

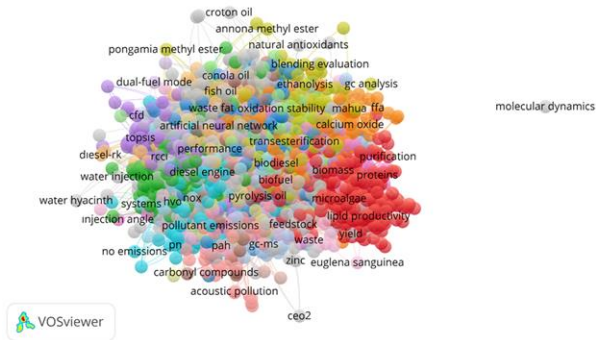


Figure 1. Keywords utilized to access literature (Compiled by the author)

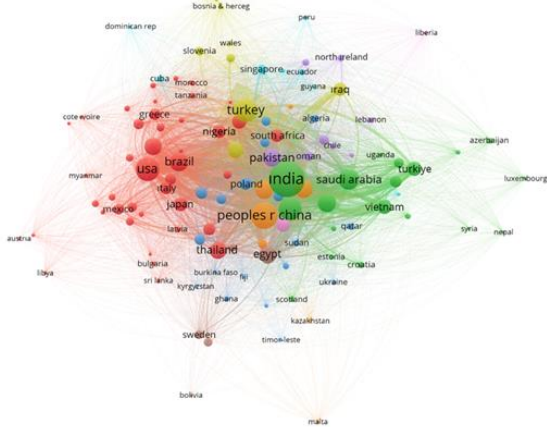


Figure 2 Global interest and spread of scientific efforts (Compiled by the author)

Figure 2 depicts the countries conducting research in this field, illustrating the worldwide interest and spread of scientific efforts related to biodiesel fuel properties.

If biodiesel is to be commercialised as an alternative fuel, it must be produced from non-edible oils. Non-edible oils, which are not part of human nutrition, might be taken into account as a feedstock for biodiesel. According to statistics from 2023, a total of 348,750 tonnes of plums were produced, with roughly 20,000 tonnes wasted and discarded as trash accounting for approximately 5.73 percent of the total production [31]. Within the context of zero waste, plum harvest loss that was not suitable for human consumption was investigated. Therefore to lessen dependency on fossil fuels and edible feedstocks, the core purpose of this assessment is to demonstrate the biodiesel potential of *Prunus insititia* L. by describing the oil's composition and predicting the fuel's qualities.

2. Material and Methods

Plums cultivated in China, Serbia, Romania,

the United States, and Turkey have a global commercial appeal. Although production volumes vary depending on the season and weather conditions, Turkey ranks fifth among plum-cultivating countries [33].

According to 2023 data, 348,750 tonnes of plums were grown in Turkey. The Mediterranean region (which includes the cities of Adana, Mersin, Hatay, Isparta, Burdur, Antalya and Osmaniye) realizes approximately 42 percent of the plum production with 146,161 tonnes [31]. Plum cultivation areas as seen in Figure 3 [34].

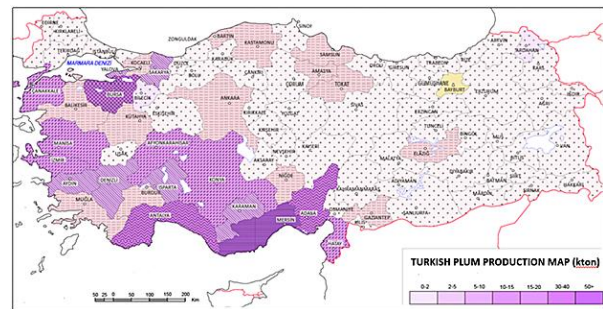


Figure 3. Plum cultivation area of Turkey [34]



Figure 4. *Prunus insititia* L.

Prunus insititia L. can be cultivated from the Mediterranean coast into Norway in the north and Russia in the northeast stretches. It extends from the west of the Himalayas to the east to Kashmir. This type is consumed as jam and marmalade rather than fresh consumption. Trees are stunted, densely branched, with more or fewer thorns and twigs, depending on the species plum. Flowers open with or after the leaves. Fruits in various shapes, mostly oval, small, bluish-black or amber-yellow, thick cloudy, sweet or sour. Its kernels stick to the meat or split [35]. Figure 4 illustrates *Prunus insititia* L. samples collected in Pozantı (a town near the Taurus Mountains) in the Mediterranean region. Fatty acid characterization was carried out using GC, and

the fatty acid profile was determined. *Prunus insititia* L. kernels were prepared (see Figure 5a) by grinding using ground machinery (Figure 5b). The moisture content of the ground kernels (Figure 5c) was found to be 8.47 percent via the Shimadzu moisture analyser (Figure 5d). Soxhlet (Figure 5e) was used to extract the oil.



Figure 5. a- *Prunus insititia* L. kernels b- Grinding machine c- Grounded kernels d- Moisture analyzer e- Soxhlet device

The *Prunus insititia* L. kernel oil (PIO) (Fig. 6a) was analyzed by gas chromatography (GC-FID Agilent 7890 A) as seen in Figure 6b.



Figure 6 a- *Prunus insititia* L. kernel oil b- GC-FID

Fatty acids, which typically include carbon atoms between C8 and C24, make up the majority of vegetable oil [36]. The oil contains both saturated and unsaturated fatty acids [37]. Fatty acids, both saturated and unsaturated, have a substantial impact on the physicochemical properties of biodiesel. The process of transesterification of vegetable oil yields biodiesel [38]. Even after the transesterification process, the fatty acid content of vegetable oils does not change [36]. The essential characteristics of biodiesel, such as its density, calorific value, viscosity, and cold flow characteristics, are thus determined by its fatty acids [36].

In order to determine whether the produced biodiesel can be used in a diesel engine without any problems, it is first necessary to determine whether the quality of the fuel is within the range specified in EN14214. For this reason, the Biodiesel analyzer v2.2 program, which uses empirical equations to estimate the fuel parameters of biodiesel from fatty acids, was used [39]. The given calculations were used to determine the estimated biodiesel properties [16, 40].

Cetane number is affected by iodine (IV) and saponification (SV) values.

$$SV = \sum (560 \times N) / M \quad (1)$$

$$IV = \sum 254 \times DN / M \quad (2)$$

hence

M: fatty ester molecular mass,

N: % ester of FA,

D: the total number of double bonds

Saturated fatty acids (SFA), polyunsaturated fatty acids (PUFA), and monounsaturated fatty acids (MUFA) are the three kinds of fatty acids found in oils. Chemically, hydrogen cannot be added to saturated fatty acids since they are already saturated with it. SFA, which only has one connection between carbon atoms, is crucial to the cold flow characteristics of biodiesel [41, 42]. Only one carbon double bond and one hydrogen atom are present in MUFA. This indicates that saturated fatty acids are more stable than this fatty acid. There are many double bonds in PUFA, and extra hydrogen can be added [43].

After the calculation of Saponification and Iodine values the Cetane Number (CN) can be

calculated by equation 3.

$$CN = 46.3 + (5.458/SV) - (0.225 \times IV) \quad (3)$$

Unsaturation Grade

$$DU = MUFA + (2 \times PUFA) \quad (4)$$

MUFA: monounsaturated FA%,

PUFA: polyunsaturated FA%.

Special indices called Allylic Position Equivalent (APE) and bis-allylic Position Equivalent (BAPE) were created to account for the quantity of allylic or bis-allylic carbons. These indices seem to be more appropriate for evaluating oxidative stability than IV [44]. Chromatographic or spectroscopic techniques like GC or NMR can be used to determine the BAPE and APE indices [45]. Because the relative rate of oxidation of bis-allylic CH₂ locations is substantially larger, the BAPE value is particularly relevant for the oxidation of unsaturated fatty molecules [44]. The quantity and location of double bonds affect how quickly autoxidation occurs. Compared to allylic sites, bis-allylic sites are significantly more susceptible to oxidation [46].

The formulas listed below were utilized to determine the oxidation stability of biodiesel. Equivalents of allylic position

$$APE = \sum ap_n \times A_{cn} \quad (5)$$

ap_n: the overall number of equivalent allylic positions

A_{cn}: FA Content

Equation 6 can be used to calculate bisallylic position equivalents (BAPE).

$$BAPE = \sum(bp_n \times A_{cn}) \quad (6)$$

bp_n: the overall number of Bisallylic positions

Oxidation stability (OS) can be computed using equation 7.

$$OS = (117.9295 / (C18:2 + C18:3) + 2.5905) \quad (7)$$

The most significant disadvantage of using biodiesel as a fuel is its cold flow properties. CFPP, CP, and PP are the cold flow properties predicted [47, 48], in that order.

Saturated long-chain factor (LCSF)

$$LCSF = (0.1 \times C_{16}) + (0.5 \times C_{18}) + (1 \times C_{20}) + (1.5 \times C_{22}) + (2 \times C_{24}) \quad (8)$$

$$\text{Cold Filter Plugging Point} = CFPP = (3.1417 \times LCSF) - 16.477 \quad (9)$$

$$\text{Cloud Point} = CP = (0.526 \times C_{16}) - 4.992 \quad (10)$$

$$\text{Pour Point} = PP = (0.571 \times C_{16}) - 12.24 \quad (11)$$

At 40 °C, the kinematic viscosity was estimated from Equation 12

$$\ln(\nu) = \sum N_i (-12.503 + 2.496 \times \ln M_{wi}) - (0.178 \times D_i) \quad (12)$$

with

Mw_i molecular weight of FA, N_i % FA, D_i double bonds quantity, respectively.

Biodiesel density is calculated by using equation 13 (at 20°C)

$$\rho = \sum Ni(0.8463 + (4.9/(Mwi)) + 0.118 \times Di) \quad (13)$$

Higher heating value can be calculated by equation 14

$$HHV = \sum Ni(46.19 - (1794 / Mwi - 0.21 \times Di))$$

For flashpoint computation equation 15 is used [49].

$$FP(^{\circ}C) = 205.226 + 0.083x_p - 1.727x_s - 0.5717x_o - 0.3557x_{LI} - 0.467x_{LN} - 0.2287x_E \quad (15)$$

with

x_p (C16:0) ratio; x_s (C18:0) ratio; x_o (C18:1) ratio; x_{LI} (C18:2) ratio; x_{LN} (C18:3) ratio; x_E (C22:1) ratio, respectively.

3. Results and Discussion

Obtained sample of plum oil was subjected to GC testing, and the gas chromatography spectra of Prunus insititia kernel oil are shown in Figure 7.

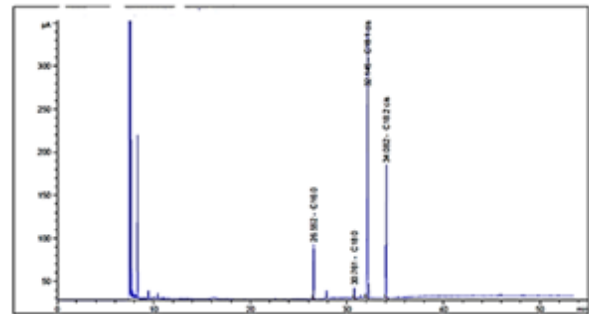


Figure 7. GC result of Purus insititia L kernel oil (PIO)

GC analysis provides detailed information on the hydrocarbons, fatty acid esters, and triglycerides present in the oil, which are crucial for understanding its fuel properties.

The X-axis represents time (minutes), while the Y-axis represents signal intensity (pA – picoampere). The distinct peaks indicate the presence of specific components in the sample. The most prominent peaks correspond to fatty acids. The labeled main fatty acids in the chromatogram are:

First Peak: C16:0 (Palmitic Acid) - 26.552 min. A saturated fatty acid. Increases viscosity

and density. May negatively affect cold flow properties but enhances oxidative stability.

Second Peak : C18:0 (Stearic Acid) - 30.761 min. Another saturated fatty acid. Contributes to higher combustion efficiency at elevated temperatures but may reduce fluidity.

Third Peak: C18:1 (Oleic Acid) - 32.145 min A monounsaturated fatty acid. It improves cold flow properties and combustion efficiency.

Fourth Peak: C18:2 (Linoleic Acid) - 34.082 min A polyunsaturated fatty acid. Enhances cold flow characteristics but reduces oxidative stability, potentially leading to polymerization over time.

The fatty acid profile is based on the corresponding data shown in Table 1.

Linoleic acid (21.405 %w), Oleic acid (61.687 %w), Palmitic acid (5.965 %w), and Stearic acid (1.459 %w) were the primary fatty acids found in *Prunus insititia* L. kernel oil. According to Table 1, the key fatty acids that define the characteristics of the resulting biodiesel are linoleic acid and oleic acid, which have the largest percentage by weight.

Prunus insititia kernel oil biodiesel fuel parameters were predicted using the biodiesel analyzer V2.2. Table 2 gives Saturated Fatty acid (SFA), Bisallylic position equivalents (BAPE), Long-chain saturated factor (LCSF), Allylic position equivalents (APE), and % monosaturated fatty acids (MUFA), % polyunsaturated fatty acids (PUFA).

The estimated physiochemical values of *Prunus insititia* biodiesel (PIB) are given in Table 3.

Saturated fatty acids (C16:0, C18:0); Increase viscosity, reduce cold flow properties.

Unsaturated fatty acids (C18:1, C18:2); Lower viscosity, improve combustion efficiency.

Polyunsaturated fatty acids (C18:2) → Improve cold flow but may require antioxidant additives for stability.

This GC analysis indicates that the oil sample has a suitable fatty acid profile for biodiesel production:

A balanced ratio of saturated and unsaturated fatty acids.

A higher proportion of unsaturated fatty acids improves cold flow properties.

Oxidative stability may need to be enhanced using antioxidants.

Biodiesel instability is caused by oxidation stability (OS), which is defined as the unsaturation of the biodiesel ester molecule [50]. The biodiesel gets increasingly unstable as the unsaturation of the FA chain increases. As a result, the rate of oxidation is determined by the location and amount of allylic and bis-allylic methylene groups adjacent to the double bond. OS is anticipated to be 8.093 hours, which is within the biodiesel standard range [51].

Total unsaturated fat is measured by the iodine value [50]. PIB has an iodine value of 95.55, which is less than the biodiesel standard's maximum iodine value.

PIB has a saponification value of 184.28, which is inversely linked to the average molecular mass of the glycerides in plum oil [16].

Table 1. Fatty acids (FA) profile of *Prunus insititia* L. kernel oil

FA	% w	FA	% w
Butyric (C4:0)	0.098±0.00	Hexanoic (C6:0)	0.077±0.00
Caprylic (C8:0)	0.014±0.00	Capric (C10:0)	0.020±0.00
Lauric (C12:0)	0.011±0.00	Myristic (C14:0)	0.067±0.00
Pentadecanoic (C15:0)	0.019±0.00	Palmitic (16:0)	5.965±0.14
Palmitoleic (C16:1)	0.079±0.01	Margaric (C17:0)	0.036±0.00
Stearic (18:0)	1.459±0.06	Oleic (C18:1)	61.687±1.46
Linoleic (18:2)	21.405±1.02	Linolenic (18:3)	0.027±0.00
Eicosenoic (C20:1)	0.099±0.02	Behenic (C22:0)	0.042±0.00
Docosahexaenoic (C22:6)	0.036±0.00	Lignoceric(C24:0)	0.027±0.00
Ervonc (24:1)	0.277±0.03	Ecucic (C22:1)	0.198±0.01

Table 2. Results of predicted values

SFA	MUFA	PUFA	DU	LCSF	APE	BAPE
7.833	62.857	21.468	105.792	1.442	104.730	21.639

Table 3. Estimated physiochemical values of PIB

Value	Diesel (EN 590)*	Biodiesel (EN 14214)*	PIB
Oxidation Stability	25 g/m ³ max	8 hrs min	8.093
Cetane Number	51	51	54.314
Iodine Value max	-	120 ¹ g iod/100g	95.550
Kinematic Viscosity (mm ² /s)	2.0-4.5	3.5-5.0	3.481
Higher Heating Value (MJ/kg)	-	-	36.420
Density (kg/m ³)	820-845	860-900	809
Saponification Value	-	-	184.936
Flash Point (°C)	55	101	160.083
Pour Point (°C)	-	-	-8.834
Cold Filter Plugging Point (°C)	a	a	-11.947
Cloud Point (°C)	a	a	-1.854

Cetane is affected by iodine and saponification levels. Being a dimensionless descriptor of a diesel fuel's ignition quality CN is very important. CN shows the potential for self-ignition. A high cetane number indicates a rapid self-ignition [50] PIB has an estimated cetane number as 54.314 which is above the Biodiesel standard which means delay time is reduced.

The resistance of one component of a substance moving over another section of the same substance is defined as viscosity. If the viscosity of the fuel is low, leakage will result in a loss of engine power PIB has a calculated viscosity of 3.481 mm²/s, which is slightly below (0.542%) minimum of the biodiesel regulations. Low-viscosity fuels generally result in better atomization, characterized by smaller droplet sizes and more uniform patterns. This is due to enhanced droplet breakup and reduced droplet aggregation, which are crucial for efficient combustion [52, 53]. Improved atomization leads to more complete fuel burns, which can enhance combustion efficiency. This is because smaller droplets have a larger surface area relative to their volume, facilitating faster evaporation and more complete mixing with air [54, 55, 56]. Better atomization and more complete combustion can lead to reduced soot and other particulate emissions. This is particularly beneficial in reducing the environmental impact of combustion engines [55,57,58]. While low viscosity improves atomization, it can also lead to issues such as fuel leakage and power loss due to insufficient lubrication and sealing in engine components [53]. Also, the ignition delay period is reduced because low viscosity

values promote faster atomization of the fuel spray [50]. The use of low-viscosity fuels can reduce emissions of nitrogen oxides (NOx) and carbon monoxide (CO), contributing to cleaner combustion processes [54,56].

Density is a key parameter. The energy content per unit volume rises as density rises [59]. The predicted density of PIB is 809 kg/m³ which is 5.93% below the limits of the EN14214 standard. Hence the density of PIB is low which will cause decreasing in the energy content. Lower fuel density can enhance air-fuel mixing, leading to more uniform combustion and potentially lower emissions. This is supported by studies showing that fuels with lower density can result in better atomization and mixing, which is crucial for efficient combustion and reduced emissions [60,61,62]. Improved mixing from lower density fuels can lead to reductions in emissions such as soot, CO, and hydrocarbons. For instance, better air utilization and mixing can significantly reduce soot and other emissions in diesel engines [62,63]. Enhanced mixing due to lower density can also improve combustion efficiency, as seen in studies where optimized mixing led to increased power delivery and reduced specific fuel consumption [63,64]

The projected Higher Heating Value of PIB is 36.420 MJ/kg. PIB has less energy content than diesel fuel. The engine produces less peak power if fuel is used with a lower energy content per litre [38].

The flashpoint of a fuel is the temperature at which it produces enough vapour to generate a flammable combination. For diesel fuel, the temperature should be between 52 and 66

degrees Celsius. Biodiesel's high flashpoint (>150) suggests that it has a minimal risk of catching fire [47]. PIB's flashpoint is anticipated to be 160.083°C, which is greater than the minimum value in EN14214, indicating that PIB is suitable for storage and transportation.

Cold flow properties (Cloud Point, Pour Point and Cold Flow Plugging Point) are very important properties for biodiesel. Decreasing temperatures promote the creation of submicron-scale solid wax crystal nuclei that are undetectable to the naked eye. These crystals develop as the temperature drops more. The temperature at which crystals become visible is known as the cloud point (CP), because they often produce a hazy or foggy suspension. Larger crystals fuse and create huge agglomerates at temperatures below CP causing startup problems [47]. The cloud point of PIB is estimated as -1.854 °C which is not too low for wintertime. The pour point (PP) is the temperature at which crystal aggregation is prevalent enough to prevent fluid from flowing freely [47]. The predicted PP for PIB is -8.834 °C. The lowest temperature at which 20 mL of oil may safely pass through the filter in 60 seconds is known as the Cold Flow Plugging Point (CFPP)[47]. The calculated value of CFPP for PIB is -11.947 °C.

4. Conclusion

Several more countries are currently attempting to reduce their reliance on foreign energy sources. Simultaneously, biofuels have become an absolute necessity due to the environmental and human health consequences of fossil fuel use. A more attainable goal would be to use biodiesel as a raw material from so-called oil. If biodiesel is to be commercialised as an alternative fuel, it must be manufactured from non-edible oils rather than edible oils. Since price rises are to be expected as a result of the withdrawal of food-grade oils, which will jeopardise long-term economic stability.

Alternative feedstocks, such as *Prunus insititia* L., that were lost and discarded as food waste, would be used at this stage. These wastes, which currently have no economic value, could be used as a new source of raw material for

biodiesel production. *Prunus insititia* L. kernels were analyzed in this study, and the fatty acid content was calculated numerically. Linoleic acid, Oleic acid, Palmitic acid, and Stearic acid were the main fatty acids in *Prunus insititia* kernel oil. The key fatty acids that determine the characteristics of the resultant biodiesel are Linoleic acid and Oleic acid. And the results are as follows:

- The predicted values of oxidation stability, flash point, cold flow properties, and cetane number were within the limits of EN14214 standards.
- However, the viscosity was calculated as 0.542% and the density 5.93% less than the minimum values in the standard. The density of 0.809 g/cm³ means the biodiesel may have slightly lower energy content than standard diesel. More fuel may be needed to achieve the same power output. Since the density of PIB is low, the oxidative stability and long-term storage durability could decrease. Antioxidant additives can be included to enhance stability. Lower density and better atomization could result in higher combustion temperatures. Result: NO_x emissions may slightly increase. This can be controlled using EGR (Exhaust Gas Recirculation) or catalytic converters. As a result of these issues, *Prunus insititia* seed L. appears to be a viable biodiesel feedstock. *Prunus insititia* kernel oil biodiesel is suggested to be produced experimentally, and engine performance aspects are investigated for future research.

Declaration of Competing Interest

The authors declare that there is no conflict of interest in the study.

CRedit authorship contribution statement

Ash Abdulvahitoğlu: Conceptualization, Formal Analysis, Methodology, Visualization, Writing - original draft, Writing - review & editing. **Nurten Cengiz:** Investigation, Writing - Original Draft.

5. References

1. World energy 418625c2c9d7/ balance available from https://iea.blob.core.windows.net/assets/23f096ab-5872-4eb0-91c4-World_Energy_Balances_Overview_2020_edition.pdf accessed 3.6.2021

2. Sakthivel R., Ramesh K., Purnachandran R., Mohamed Shameer P.. A review on the properties, performance and emission aspects of the third generation biodiesels. *Renew Sust Energ Rev.*, 82, pp.2970–2992, 2018. <https://doi.org/10.1016/j.rser.2017.10.037>
3. Shuit S.H., Tan K. T., Lee K. T. Kamaruddin A. H. Oil palm biomass as a sustainable energy source: A Malaysian case study Author links open overlay panel. *Energy.*, 34(9), pp.1225-1235, 2009. <https://doi.org/10.1016/j.energy.2009.05.008>
4. Sugebo, B., Demrew, Z., Feleke, S. Biazen M. Evaluation and characterization of rubber seed oil for biodiesel production. *Biomass Conv. Bioref.* 2021. <https://doi.org/10.1007/s13399-021-01900-4>
5. Abdulvahitoğlu A, Tüccar G. Evaluation of watermelon seed biodiesel as an alternative fuel in diesel engines. *J Fac Eng Archit Gazi*, 32(1), pp.189-194, 2017. <https://doi.org/10.17341/gazimmfd.300610>
6. Aderibigbe F.A., Mustapha S.I., Adewoye T.L., Mohammed I.A., Gbadegesin A.B., Niyi F.E., Olowu O.I., Soretire A.G., Saka H.B. Qualitative role of heterogenous catalysts in biodiesel production from *Jatropha curcas* oil. *Biofuel Research Journal*, 26, pp.1159-1169, 2020. <https://doi.org/10.18331/BRJ2020.7.2.4>
7. Verma P, Sharma M.P. Review of process parameters for biodiesel production from different feedstocks. *Renew Sust Energ Rev.*, 62, pp.1063–1071, 2016. <https://doi.org/10.1016/j.rser.2016.04.054>
8. Latinas A., Geivanidis S., Faliakis A., Courouclis Y., Samaras Z., Keder A., Krasnoholovets V., Gandzha I., Zabulonov Y., Puhach O., Dmytryuk M.. Biodiesel production from high FFA feedstocks with a novel chemical multifunctional process intensifier. *Biofuel Research Journal*, 26, pp.1170-1177, 2020. <https://doi.org/10.18331/BRJ2020.7.2.5>
9. Avinash A., Mahian O., Hollmann F., Zhang W., Environmentally benign solid catalysts for sustainable biodiesel production: A critical review. *Sci Total Environ*, 768, pp.144856, 2021. <https://doi.org/10.1016/j.scitotenv.2020.144856>
10. Cijil B. John, S. Antony Raja, B. Deepanraj, H. C. Ong. Palm stearin biodiesel: preparation, characterization using spectrometric techniques and the assessment of fuel properties *Biomass Conv. Bioref.*, 12, pp.1679–1693, 2022. <https://doi.org/10.1007/s13399-020-01265-0>
11. Azam M. M., Waris A., Nahar N. M. Prospects and potential of fatty acid methyl esters of some non-traditional seed oils for use as biodiesel in India. *Biomass Bioenerg*, 29, pp.293–302, 2005. <https://doi.org/10.1016/j.biombioe.2005.05.001>
12. BP stats are available from <https://www.bp.com/content/dam/bp/business-sites/en/global/corporate/pdfs/energy-economics/statistical-review/bp-stats-review-2022-full-report.pdf> 18.12.2024.
13. FAO available from http://www.fao.org/3/cb1993en/cb1993en_oil_crops.pdf accessed 3.6.2021.
14. Abdulvahitoğlu A., Evaluation of the fuel quality values of bay laurel (*Laurusnobilis* L.) oil as a biodiesel feedstock. *Biofuels*, 9(1), pp. 95-100, 2018. <https://doi.org/10.1080/17597269.2016.1257319>
15. Al-Samaraae R. R., Atabani A. E., Gediz U., Gopalakrishnan K., Arpa O., Ayanoglu A., Mohammed M.N., Farouk H., Perspective of safflower (*Carthamustinctorius*) as a potential biodiesel feedstock in Turkey: characterization, engine performance and emissions analyses of butanol–biodiesel–diesel blends, *Biofuels*, 11 (6), pp.715-731, 2017. <https://doi.org/10.1080/17597269.2017.1398956>
16. Sahafi S. M., Ahmadibeni A., Talebi A. F., Goli S. A. H., Aghbashlo M., Tabatabaei M. Seed oils of *Sisymbriumirio* and *Sisymbriumsophia* as a potential non-edible feedstock for biodiesel production. *Biofuels*, 12(1), pp.103-111, 2021. <https://doi.org/10.1080/17597269.2018.1457315>
17. Dmytryshyn S. L., Dalai A. K., Chaudhari S. T., Mishra H. K., Reaney M. J., Synthesis and characterization of vegetable oil derived esters: evaluation for their diesel additive properties. *Bioresource Technol*,

- 92(1), pp.55–64, 2004. <https://doi.org/10.1016/j.biortech.2003.07.009>
18. Rao G. L. N, Prasad B. D, Sampath S, Rajagopal K., Combustion Analysis of Diesel Engine Fueled with Jatropha Oil Methyl Ester - Diesel Blends, *Int J Green Energy*, 4(6), pp.645-658, 2007. <https://doi.org/10.1080/15435070701665446>
19. Mbarawa M., Performance, emission and economic assessment of clove stem oil–diesel blended fuels as alternative fuels for diesel engines. *Renew Energ*, 33, pp.871–882, 2008. <https://doi.org/10.1016/j.renene.2007.06.009>
20. Ramos M. J., Fernández C. M., Casas A., Rodríguez L., Pérez A. Influence of fatty acid composition of raw materials on biodiesel properties. *Bioresource Technol*, 100, pp.261–8, 2009. <https://doi.org/10.1016/j.biortech.2008.06.039>
21. Puhan S., Jegan R., Balasubramanian K., Nagarajan G., Effect of injection pressure on performance, emission and combustion characteristics of high linolenic linseed oil methyl ester in a DI diesel engine. *Renew Energ*, 34, pp.1227–1233, 2009. <https://doi.org/10.1016/j.renene.2008.10.001>
22. Abdulvahitoglu, A., Aydin, K. Performance and exhaust emission characteristics of a CI engine fueled with synthesized fuel blends *Energy Education Science and Technology Part A: Energy Science and Research*, , 28(2), pp.699–710, 2012.
23. S. Simsek, E. Koç, and A. Öztürk, “Unique fatty acid composition of coriander seed biodiesel”, *International Journal of Automotive Engineering and Technologies*, vol. 13, no. 3, pp. 114–122, 2024. doi: 10.18245/ijaet.1497824.
24. Ruhul Md. A., Abedin Md. J., Ashrafur Rahman S. M., Bin Haji M. H., Alabdulkarem A., Abul Kalam Md., Shancita I., Impact of fatty acid composition and physicochemical properties of Jatropha and Alexandrian laurel biodiesel blends: An analysis of performance and emission characteristics. *J Clean Prod.*, 133, pp.1181-1189, 2016. <https://doi.org/10.1016/j.clepro.2016.06.07>
25. Devarajan Y, Selvam D C, Utilization of stercuria foetida oil as a sustainable feedstock for biodiesel production: optimization, performance, and emission analysis, *Results in Engineering*, Volume 24, 103196, 2024. <https://doi.org/10.1016/j.rineng.2024.103196>.
26. AlYammahi J., Chelaifa H., Hasan A., Darwish A.S., Lemaoui T., Hernandez H.H., Rios-Galvan A., Salicornia seed oil: A high-yielding and sustainable halophytic feedstock for biodiesel and energy in underutilized hypersaline coastal deserts, *Energy Conversion and Management*, Volume 318, 118914, 2024. <https://doi.org/10.1016/j.enconman.2024.118914>.
27. Rajesh K., Natarajan M. P., Devan P. K., Ponnuvel S., Coconut fatty acid distillate as novel feedstock for biodiesel production and its characterization as a fuel for diesel engine. *Renew Energ*, 164, pp.1424-1435, 2021. <https://doi.org/10.1016/j.renene.2020.10.082>
28. Turkstat available from www.turkstat.gov.tr accessed 16.12.2024.
29. Borovalı S. available from www.dunyaenerji.org.tr/wp-content/uploads/2019/04/Selcuk-Borovali-Sunum accessed 3.6.2021.
30. Atlasbig is available from www.atlasbig.com/tr/ulkelerin-erik-uretimi accessed 3.6.2021.
31. Plum cultivation map available from <http://cografyaharita.com/haritalarim/4cturkiye-2019-erik-uretim-haritasi.png> accessed 3.6.2021.
32. Plum available from <https://acikders.ankara.edu.tr/pluginfile.php/112430/modresource/content/0/ER%C4%B0K%20DERS%20NOTU-7.%20HAFTA.pdf> accessed 3.6.2021.
33. A.E. Atabani, A.S. Silitonga, Irfan Anjum Badruddin, T.M.I. Mahlia, H.H. Masjuki and S. Mekhilef. “A comprehensive review on biodiesel as an alternative energy resource and its characteristics”, *Renewable and Sustainable Energy Reviews*, pp. 2070–2093, 2012.
34. Jana Orsavova, Ladislava Misurcova, Jarmila Vavra Ambrozova, Robert Vicha and Jiri Mlcek, “Fatty acids composition of vegetable oils and its contribution to dietary energy intake and dependence of cardiovascular mortality on dietary intake of fatty acids”, *International Journal of Molecular*

Sciences, Vol. 16, pp. 12871-12890, 2015.

35. Gog Adriana, M. Chintoanu, M. Roman, Gabriela Pitl, E. Luca and F. D. Irimie, "Biodiesel as alternative fuel – general aspects", *Agricultura – Stiina si practica*, no. 3-4 (63-64), 2007.

36. Biodiesel Analyzer available from <http://brteam.org/analysis/#id02> "biodiesel Analyzer © Version 2.2" accessed 3.6.2021.

37. Talebi, A.F., Tabatabaei, M., Chisti Y. "Biodiesel analyzer©: a user-friendly software for predicting the properties of prospective biodiesel" *Biofuel Research Journal* 1, 2, pp.55-57, 2014. <https://doi.org/10.18331/BRJ2015.1.2.4>

38. Arjun B. Chhetri, K. Chris Watts and M. Rafiqul Islam, "Waste cooking oil as an alternate feedstock for biodiesel production", *Energies*, Vol. 1, pp. 3-18, 2008.

39. Alok Patel, Neha Arora, Juhi Mehtani, Vikas Pruthi and Parul A. Pruthi, "Assessment of fuel properties on the basis of fatty acid profiles of oleaginous yeast for potential biodiesel production", *Renewable and Sustainable Energy Reviews*, Vol. 77, pp. 604-616, 2017.

40. Nithyananda B S, Prakash G V N, Vinay K B, Mohankrishna S A, Ankegowda N "Investigation on the Effect of Fatty Acids Composition on the Fuel Properties of Biodiesel" *E3S Web of Conferences* 559, 03001 ICSTCE 2024. <https://doi.org/10.1051/e3sconf/202455903001>

41. Knothe G, Dunn R O. Dependence of oil stability index of fatty compounds on their structure and concentration and presence of metals. *Journal of the American Oil Chemists Society*; 80(10):1021–6, 2003.

42. Knothe G. Structure indices in FA chemistry. How Relevant Is the Iodine Value? *Journal of the American Oil Chemists' Society*; 9:847–53, 2002.

43. JPullen, K. Saeed An overview of biodiesel oxidation stability / *Renewable and Sustainable Energy Reviews*, 16, 5924–5950, 2012.

44. Sarin A, Arora R, Singh N, Sarin R, Malhotra R, Kundu K. Effect of blends of Palm-Jatropha-Pongamia biodiesels on cloud point and pour point. *Energy*, 34, pp.2016–2021, 2009.

<https://doi.org/10.1016/j.energy.2009.08.017>

45. Senthamilselvi, D., Kalaiselvi, T., Gamma ray mutants of oleaginous microalga *Chlorella* sp. KM504965 with enhanced biomass and lipid for biofuel production. *Biomass Conv. Bioref.* 2022. <https://doi.org/10.1007/s13399-022-02400-9>

46. Agarwal M, Singh K, Chaurasia S. P. Prediction of Biodiesel Properties from Fatty Acid Composition using Linear Regression and ANN Techniques, *Indian Chemical Engineering* 52, (4), pp.347-361, 2010. <https://doi.org/10.1080/00194506.2010.616325>

47. Knothe G., Van Gerpen J., Krahl J. "The Biodiesel Handbook" AOCS, ISBN 1-893997-79-0. 2005.

48. Dieselnet available from https://dieselnet.com/tech/fuel_biodiesel_std.php accessed 3.6.2021.

49. van Basshuysen R., Schäfer F. "Internal Combustion Engine Handbook" Basics, Components, Systems, and Perspectives. SAE International.; ISBN 0-7680-1139-6. 2004.

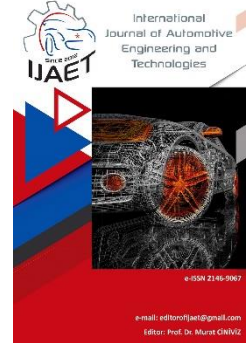


e-ISSN: 2146 - 9067

International Journal of Automotive Engineering and Technologies

journal homepage:

<https://dergipark.org.tr/en/pub/ijaet>



Original Research Article

Application of RSM for prediction and optimization of performance and emissions of diesel engine fuelled with butanol-diesel blends



Ceyla Güngör^{1*}

^{1,*} Energy Systems Engineering Department, Engineering Faculty, Adana Alparslan Türkeş Science and Technology University, Adana, 01250, Türkiye.

ARTICLE INFO

Orcid Numbers

1. 0000-0002-4072-6784

Doi: 10.18245/ijaet.1565350

* Corresponding author
cozgur@atu.edu.tr

Received: Oct 11, 2024

Accepted: May 03, 2025

Published: 30 Jun 2025

Published by Editorial Board Members of IJAET

© This article is distributed by Turk Journal Park System under the CC 4.0 terms and conditions.

To cite this paper: Güngör, C., Application of RSM for prediction and optimization of performance and emissions of diesel engine fuelled with butanol-diesel blends, International Journal of Automotive Engineering and Technologies. 2025, 14 (2), 99 – 110.

<http://dx.doi.org/10.18245/ijaet.1565350>

ABSTRACT

This work investigated the impacts of butanol-diesel fuel blends used in a turbocharged six-cylinder heavy-duty diesel engine on engine performance and exhaust emission parameters. It evaluated their optimization by using response surface methodology. The engine's operational factors, such as engine speed and the proportion of butanol-diesel fuel blend, have been optimized to attain optimal engine performance and exhaust emissions. The model was designed by Central Composite Design using Minitab software (trial version) and confirmed by the experimental results. According to RSM, the optimum blend ratio of butanol-diesel fuel and engine speed were 5% and 1721.4 rpm, respectively. Optimum desirability is found as 0.6260 with a butanol-diesel fuel blend of 5% and 1721.4 rpm engine speed for the heavy-duty diesel engine. The responses obtained under optimal conditions were determined as 821.19 Nm for torque, 158.1 kW for power, 895.7 ppm for NO_x, 104.05 ppm for CO, and 21.14 ppm for HC, respectively. The values for the R² coefficient determination were 99.02%, 99.98%, 99.67%, 99.97%, and 99.95%, respectively.

Keywords: Butanol; performance; emissions; RSM; prediction; optimization.

1. Introduction

The widespread utilization of diesel engines in automobiles, transportation, industry, and agriculture stems from their exceptional fuel efficiency and durability. Conversely, the use of fossil fuels is also increasing, providing the main fuel source for engines [1]. It is commonly acknowledged that the main causes of global climate change are emissions from the burning of fossil fuels, such as carbon monoxide (CO), carbon dioxide (CO₂),

particulate matter (PM), and nitrogen oxides (NO_x) [2,3]. Researchers are compelled to explore clean, sustainable, and economically viable energy sources for engine applications due to the prominent issues of climate change and the energy crisis [4]. Many researchers have conducted studies on oxygenated fuels because of several advantages [5-10]. It has been demonstrated that using diesel fuel blends with alcohols such as methanol, ethanol, and butanol enhances engine performance, improves engine combustion, and decreases

exhaust pollution emissions [1, 11].

Due to its superior fuel properties over lower carbon alcohols like methanol and ethanol, N-butanol generated from lignocellulosic residual feedstocks is now recognized as a promising and sustainable green energy alternative for diesel engines [8]. Compared to other alcohols, butanol provides several advantages as an alternative fuel for diesel engines because of its high cetane number, high heating value, high miscibility, and low vapor pressure. As a result, butanol research has been more well-known recently. Research on butanol-diesel blends and diesel engines has shown that reducing exhaust emissions can be done without a major impact on engine performance [12, 13]. Zhu et al. [14] examined how fuel mixes containing diesel and n-butanol affected particulate matter (PM) emissions using a pilot-main injection technique. Three different mixtures, diesel, D80B20, and D50B50, were made, and tests were carried out experimentally with two different injection pressures (40 MPa, 60 MPa) and two different load levels (~30%, ~60%). Consequently, n-butanol is a viable additive for diesel engines since it can lower PM and NO_x emissions while influencing the soot particles' functional groups, degree of disorder, and oxidative reactivity. Yılmaz et. al. [15] have found that all N-butanol blends such as DBu5, DBu20, and DBu35 reduce both NO_x emissions and total PAH emissions when compared to diesel fuel. Doğan [16] used a modified single-cylinder, four-stroke, naturally aspirated, water-cooled HS DI CI engine to study the influence of n-butanol/diesel fuel blends (at volumetric ratios of 5%, 10%, 15%, and 20%) on engine performance and exhaust emissions. The results of the study showed that while hydrocarbon emissions increased, nitrogen oxide, soot, and carbon monoxide emissions decreased as the amount of n-butanol in the fuel blends increased.

Different optimization methodologies are employed to utilize test results for modeling and analyzing the system [17]. ANN, RSM, Taguchi, and genetic algorithms are a few of the most popular artificial intelligence-based computer programs for optimization [18]. Response Surface Methodology (RSM) is a

statistical and mathematical technique that is widely applied in many industries, including manufacturing, chemistry, and engineering [19, 20]. One of the most important advantages of RSM is that it saves money and time by reducing the number of experiments [21, 22]. RSM techniques have been utilized in numerous studies in internal combustion engine applications [22-25]. Dubey et al. [26] looked into the possibility of using waste soybean cooking oil (WSCO) biodiesel in place of conventional fuel for diesel engines used in agriculture. Response surface methodology (RSM) was used in the study, which varied the EGR rates of mixes of WSCO biodiesel-diesel fuel. Ghanbari et al. [27] examined the impact of alumina nanoparticle concentration and engine speed in combination on the emissions and performance of a four-stroke, six-cylinder diesel engine. Alumina nanoparticles were added in different ratios to diesel-biodiesel fuel blends to form mixtures. Response surface methodology (RSM) was used to analyse the way various variables interacted with the diesel engine's performance and emissions.

The literature has revealed a lack of comprehensive studies on the optimization of butanol-diesel fuel blends' impacts on engine performance and exhaust emissions in heavy-duty diesel engines. This study aims to minimize exhaust emissions while optimizing engine performance values. This will be achieved by applying the RSM technique to optimize the butanol ratio and engine speed.

2. Material and Method

2.1. Test fuels

Blends of butanol and diesel were utilized as fuel in the experimental testing. Diesel fuel was blended at 5, 10, and 15% volumetric rates to create the fuel mixes. Before the start of the experiments, the engine underwent a 15-minute operation using diesel fuel to reach the operating temperature. Table 1 lists the properties of the fuels used for the experiments.

2.2. Engine set up

A six-cylinder, four-stroke diesel engine with an air-cooling turbocharger was used for the experiments. Engine performance and

emission values have been evaluated by running the engine at different speeds using butanol and diesel fuel mixtures. When butanol was used as a fuel additive in diesel engines, the torque, power, and exhaust emissions (NO_x, CO, and HC) of butanol-diesel fuel blends were measured. Figure 1 shows a schematic representation of the test setup. Technical specifications of the engine are given in Table 2.

2.3. RSM (Response surface methodology)

RSM mathematical modelling is employed to

attain a heavy-duty diesel engine's optimum engine performance and exhaust emissions. RSM is computer-based software used for modelling and optimizing, which has been successfully tested in various fields and has no limitations on its application [28, 29]. RSM methods are frequently employed to effectively run the engine by optimizing the preferred output and operational parameters [30]. Using the least necessary experiments, the engine's performance and exhaust emissions were assessed across a range of input parameter variations.

Table 1. Properties of fuel

Fuel Properties	Diesel	Butanol
Heating value (kJ/kg)	45144	33100
A/F Ratio (-)	15	11.2
Density (kg/m ³) at 20°C	0.835	0.810
Cetane Number	61	~25
Kinematic Viscosity (mm ² /s) at 40°C	2.75	2.25
Carbon/Total Mass Ratio (%)	86	64.8
Oxygen/Total Mass Ratio (%)	-	21.6
Molar mass (g/mol)	174	74.12

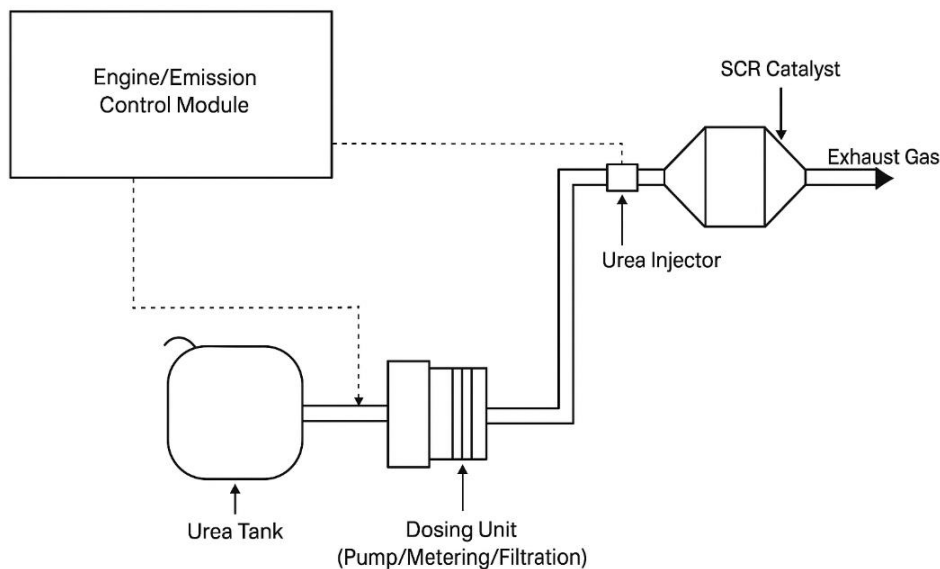


Figure 1. Schematic diagram of engine setup

Table 2. Specifications of engine

Brand	Cummins
Model	ISBE4+250B
Type	Electronic control system
Cylinder	6
Bore/Stroke	107/124 mm
Compression Ratio	17.3
Weight	485 kg
Aftertreatment	SCR
Peak Torque/ Speed (r/min)	1200-1800
Rated Speed	2500 rpm
Displacement	6700cc
Power	184 kW@2500 rpm
Torque	1020Nm @1500 rpm
Oil Cooler	Turbocharger & aftercooled

Table 3. Independent parameters and their corresponding levels

Symbol	Parameter	Unit	Level		
A	Butanol ratio	%	-1	0	+1
			5	10	15
B	Engine speed	rpm	1400	1800	2200

Table 4. Engine performance tests comparison between predicted and experimental values

No	A: Butanol ratio (%)	B: Engine speed (rpm)	Experimental		RSM	
			Torque (Nm)	Power (kW)	Torque (Nm)	Power (kW)
1	5	1400	848.15	136.02	853.79	135.84
2	10	1800	798.42	160.45	799.22	160.37
3	10	1800	798.42	160.45	799.22	160.37
4	10	1400	847.15	134.21	845.30	134.35
5	10	1800	798.42	160.45	799.22	160.37
6	5	2200	715.69	172.41	721.49	172.16
7	10	1800	798.42	160.45	799.22	160.37
8	10	1800	798.42	160.45	799.22	160.37
9	10	2200	712.54	170.15	710.38	170.43
10	15	2200	702.44	168.15	698.81	168.13
11	5	1500	820.45	161.54	809.02	161.98
12	15	1400	840.15	132.25	836.36	132.29
13	15	1800	781.54	158.21	788.96	158.19

Table 5. Exhaust emission tests comparison between predicted and experimental values

No	A:Butanol ratio (%)	B: Engine speed (rpm)	Experimental			RSM		
			NOx (ppm)	CO (ppm)	HC (ppm)	NOx (ppm)	CO (ppm)	HC (ppm)
1	5	1400	1034	108	13.81	1031.99	107.54	13.73
2	10	1800	845	130	22.93	841.66	128.97	22.90
3	10	1800	845	130	22.93	841.66	128.97	22.90
4	10	1400	998	105	14.08	1006.53	103.92	14.06
5	10	1800	845	130	22.93	841.66	128.97	22.90
6	5	2200	725	534	26.87	723.15	529.87	26.70
7	10	1800	845	130	22.93	841.66	128.97	22.90
8	10	1800	845	130	22.93	841.66	128.97	22.90
9	10	2200	694	508	27.02	702.20	514.25	27.18
10	15	2200	687	502	27.48	680.65	499.87	27.49
11	5	1500	861	134	22.25	864.86	138.59	22.50
12	15	1400	987	100	14.12	980.49	101.54	14.22
13	15	1800	805	120	23.25	817.86	120.59	23.14

In this research, data analysis was conducted utilizing the trial version of Minitab software, with the central composite design (CCD) being favored to construct a second-degree model [31]. In this particular model, the independent parameters selected were the ratio of butanol and engine speed, while torque, power, and

exhaust emissions (NO_x, CO, HC) were considered dependent variables. Table 3 provides a list of independent parameters and their corresponding levels. Figure 2 illustrates the procedures for RSM optimization.

13 empirical trials were carried out on the system to gather responses. The first stage of

RSM involves establishing an appropriate correlation between input and output parameters. For this correlation, a second-order equation model is applied, as shown in Eq. 1. [32].

$$Y = \beta_0 + \sum_{i=1}^k \beta_i X_i + \sum_{i=1}^k \beta_{ii} X_i^2 + \sum_{i=1}^k \sum_{i < j}^k \beta_{ij} X_i X_j + \varepsilon \quad (1)$$

Y is response, β_0 is the constant coefficient, X_i are the main factors, β_{ii} , β_{ij} , are the linear, quadratic, and interaction between the variables i and j coefficients respectively, ε is the residual.

The obtained experimental and predicted values of engine performance (torque, power) and exhaust emissions (NO_x, CO, HC) are listed in Table 4 and Table 5, respectively. The experimental quadratic polynomial models presented below were utilized to predict engine performance and exhaust emissions by fitting the experimental results.

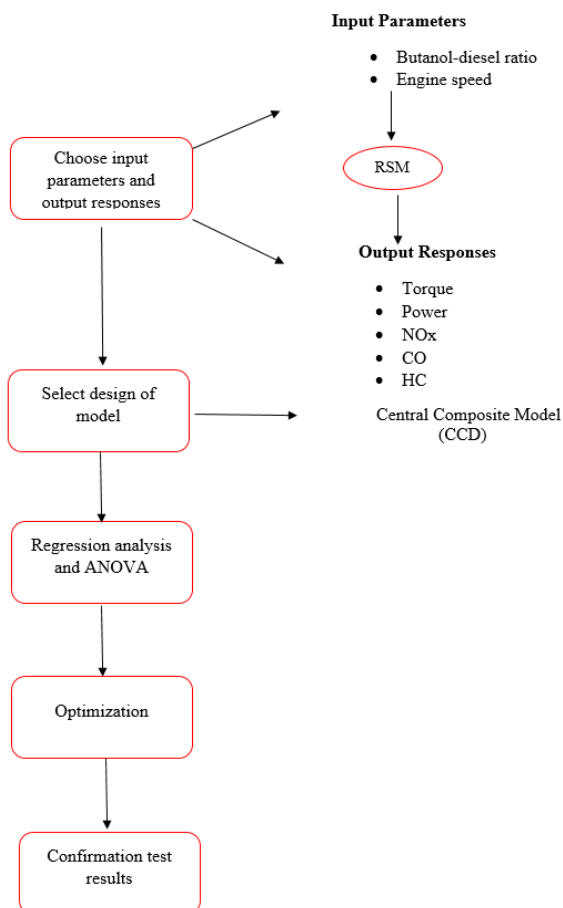


Figure 2. RSM flowchart

2.4. Desirability

Harrington introduced the desirability function as a method for optimizing multiple responses,

and it has since been extensively employed to optimize multiple responses simultaneously [33]. Every response was converted into a dimensionless desirability value (d), which varies between $d = 0$, implying the response was entirely unacceptable, and $d = 1$, implying the response was more favourable [34]. It's essential to either maximize, minimize, or keep a constant value for the response variable being optimized to ensure the accuracy of comparisons made with measurement outcomes. As a result, researchers establish the "response target" when developing the RSM model [35].

3. Results and Discussions

3.1 RSM model

Numerical evidence about the probability value is obtained through variance analysis (ANOVA) [36]. Using variance analysis (ANOVA), the significant values between the input variables and responses have been obtained. The fact that the R^2 values gathered from RSM for all responses are greater than 0.95 indicates that these results are statistically meaningful. In ANOVA results, the p-value holds significant importance. Generally, a p-value of 0.05 or less is considered significant. Models with p-values exceeding 0.05 are typically deemed insignificant. A factor is considered to have had a significant impact on the model if its p-value is less than 0.05 [37]. Table 6 and Table 7 demonstrate the stability of the model analyzed using ANOVA, respectively. According to the tables, it is observed that the model's p-values are less than 0.0001. In Response Surface Methodology (RSM), the primary indicators for assessing a model are the R^2 and adjusted R^2 values. R^2 values approaching 1 indicate strong significance, highlighting the model's explanatory power and goodness of fit [38]. Table 8 gives the R^2 , adj. R^2 and Pred. R^2 values for the model, respectively. The R^2 values for Torque, Power, NO_x, CO, and HC are respectively 99.02%, 99.98%, 99.67%, 99.97%, and 99.95%. Importantly, the fact that all models have R^2 values exceeding 0.9 indicates a strong fit of the regression model to the data. Table 9 gives the regression equations acquired from the model for each response.

Table 6. Variance Analysis for torque and power

Source	Torque		Power		Significant
	F-value	P-value	F-value	P-value	
Model	141.94	0.000	7271.38	0.000	Significant
A-Butanol ratio (%)	14.56	0.007	357.82	0.000	
B-Engine speed (rpm)	659.03	0.000	32478.93	0.000	
AB	0.17	0.0060	1.00	0.351	
A ²	0.00	0.954	3.71	0.095	
B ²	20.47	0.001	2925.35	0.000	

Table 7. Variance analysis for Exhaust emissions (NO_x, CO, HC)

Source	NO _x		CO		HC		Significant
	F-value	P-value	F-value	P-value	F-value	P-value	
Model	428.57	0.000	5504.41	0.000	2593.44	0.000	Significant
A-Butanol ratio (%)	49.73	0.000	37.33	0.000	28.85	0.001	
B-Engine speed (rpm)	2085.14	1	19400.75	0.000	12123.26	0.000	
AB	0.30	0.599	11.06	0.013	1.06	0.338	
A ²	0	0.954	0.08	0.783	0.90	0.374	
B ²	6.69	0.036	6883.19	0.000	676.16	0.000	

Table 8. Model Evaluation

Model	Torque	Power	NO _x	CO	HC
R ²	99.02%	99.98%	99.67%	99.97%	99.95%
Adj. R ²	98.33%	99.97%	99.44%	99.96%	99.91%
Pred. R ²	90.32%	99.84%	97.64%	99.78%	99.48%

Table 9. Regression Equations for responses

Regression Equations
Torque = 677.2 - 0.64A + 0.391B - 0.009A ² - 0.000134B ² - 0.00066AB
Power = -80.84 - 0.041A + 0.22524B - 0.01137A ² - 0.000050B ² - 0.000061AB
NO _x = 1850-6.49 A-0.678B-0.012A ² + 0.000079B ² + 0.00112AB
CO = 2819.6 + 3.10A - 3.5098B + 0.0248A ² + 0.001126B ² - 0.003000 AB
HC = -53.16 + 0.0633A + 0.06740B - 0.00334A ² - 0.000014 B ² + 0.000038AB

The engine performance (power, torque) and exhaust emissions (NO_x, CO, and HC) of a heavy-duty diesel engine running on butanol-diesel fuel mixes were compared between experimental and predicted values to assess the success of the RSM model. As seen in Figure 3, all response distributions are along or close to a straight line. The quality of model fit is assessed by the coefficient of determination (R²). The analysis of the regression equation by ANOVA showed that the R² value was 0.9887. The adjusted R² and predicted R² values were 0.9767 and 0.9461 respectively. There is a reasonable agreement between the predicted R² and adjusted R² values because the difference is less than 0.2. Therefore, this model could be used in the theoretical prediction of the pomegranate seed oil biodiesel production process.

Pareto chart and regression equation were created for each response. The Pareto chart displays the absolute magnitudes of the standardized impacts arranged from the most significant to the least significant.

Additionally, it includes the vertical dashed red line established by the model to highlight the statistically significant effects. If the bar graph representing selected variables lies to the right of this line, it signifies effectiveness; conversely, if it falls to the left, it denotes ineffectiveness. Figure 4 demonstrates the Pareto charts of responses respectively. According to Figure 4 the impact of engine speed seems to be more significant for all responses.

3.2. Effects of input parameters on torque and power

Figure 5 displays the effects of engine operating variables on torque and power, respectively. These variables are the butanol ratio and engine speed. As can be seen from Figure 5, increasing the amount of butanol in diesel fuel results in decreases in torque and power values which may be due to butanol having a lower calorific value than diesel fuel [39]. 3D surface and contour plot of power is shown in Figure 6. Power increases as engine

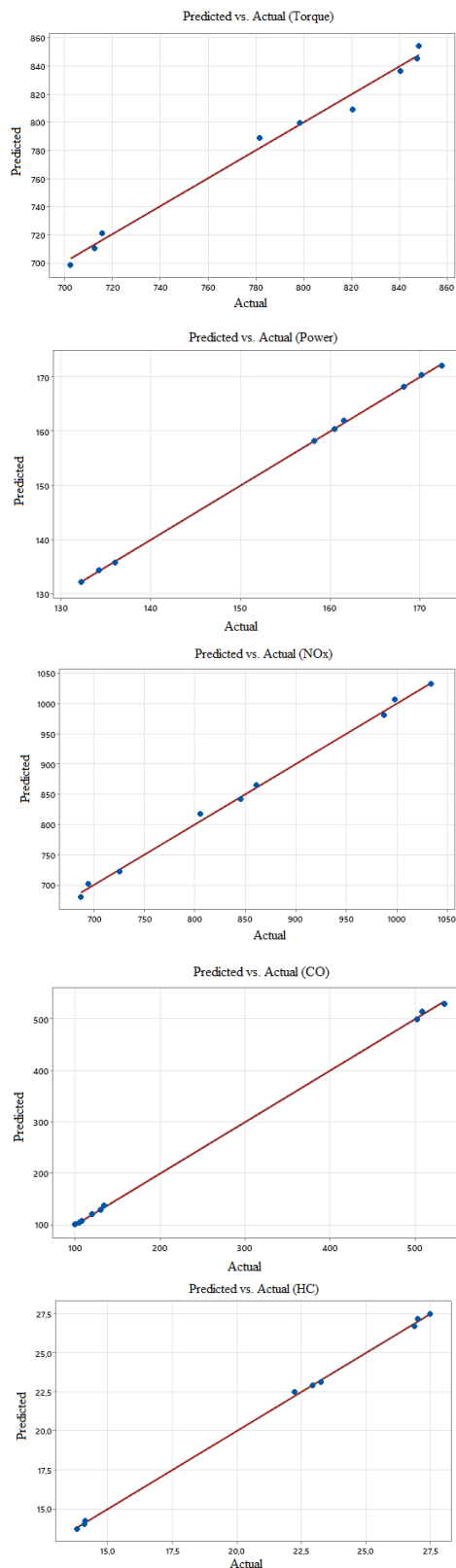


Figure 3. Comparison of predicted and experimental values of all responses

speed increases. The maximum engine power was obtained as 172.41 kW at 2200 rpm engine speed in a 5% butanol-diesel fuel mixture. A decrease in engine power is observed as the ratio of butanol in the fuel mixtures increases. Butanol has a lower calorific value compared

to diesel fuel. As the proportion of butanol in the butanol-diesel fuel blends increases, a decrease in engine power has been observed due to the lower energy content of these mixtures [40].

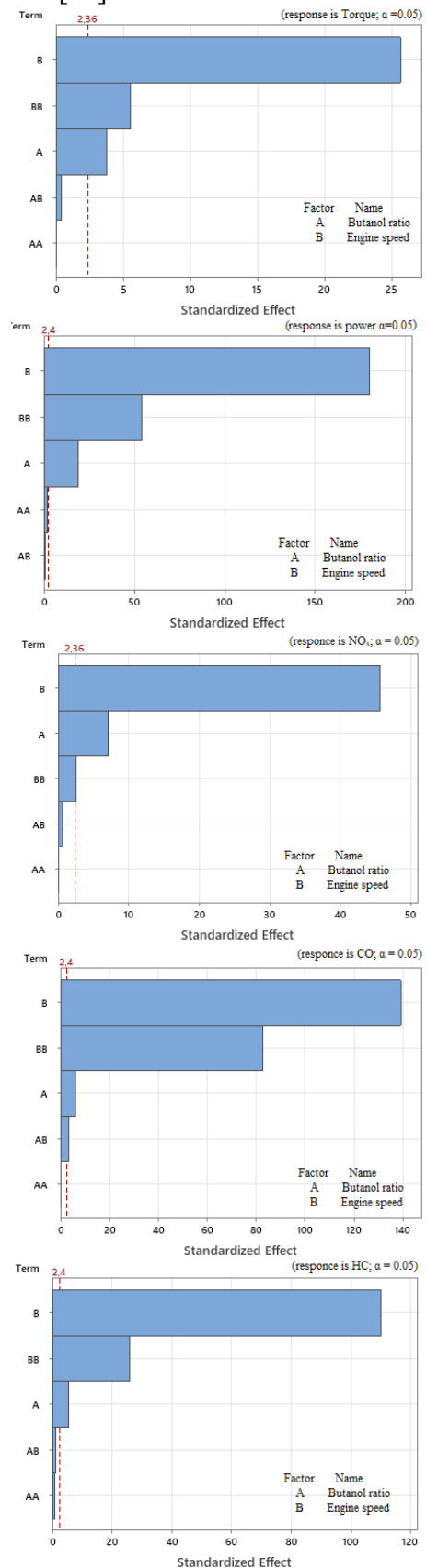
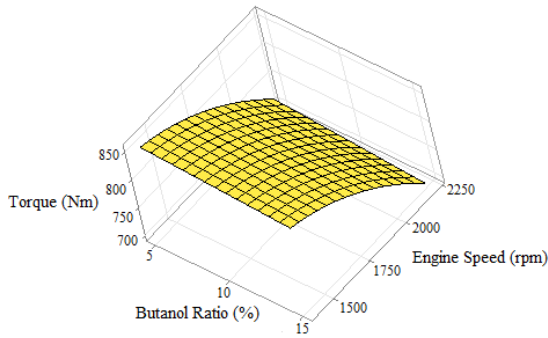
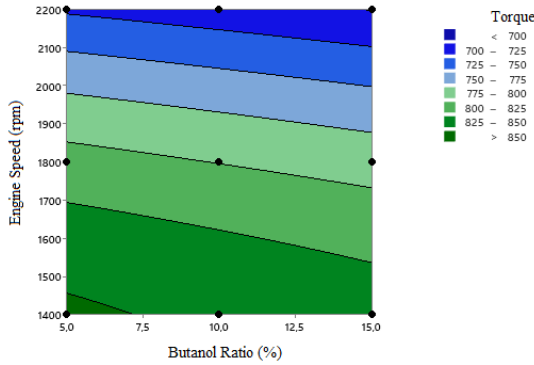


Figure 4. Pareto charts for all responses

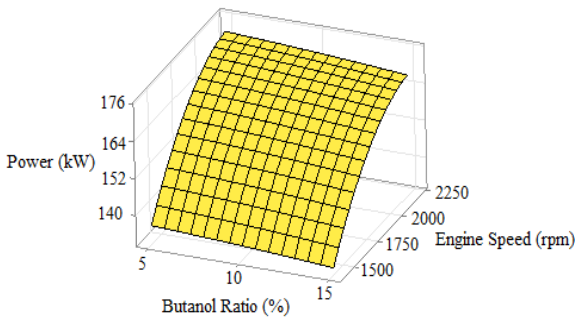


(a) 3D surface plot

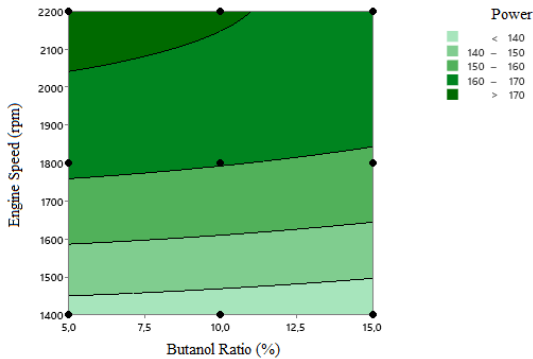


(b) Contour plot

Figure 5. (a) 3D surface plot and (b) Contour plot for Torque versus butanol ratio and engine speed



(a) 3D surface plot



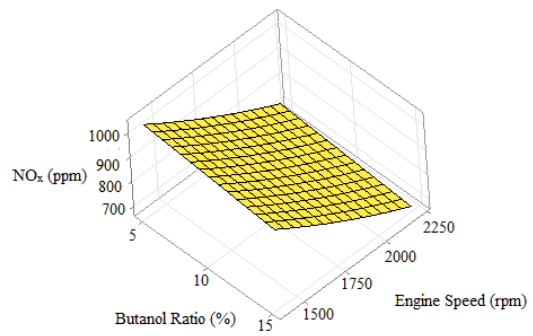
(b) Contour plot

Figure 6. (a) 3D surface plot and (b) Contour plot for Power versus butanol ratio and engine speed

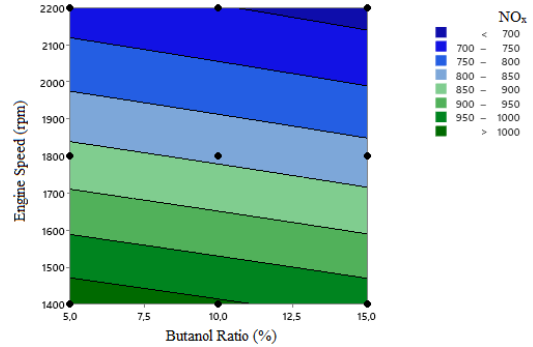
3.3. Effects of input parameters on NO_x, CO, HC

As depicted in Figure 7, increasing the proportion of butanol in fuel blends leads to a decrease in NO_x emissions. This reduction is primarily due to butanol's high latent heat of

vaporization. The elevated latent heat of vaporization facilitates greater heat removal from the combustion chamber, thereby reducing the peak temperature during combustion [41]. Figure 8 clearly shows that adding butanol to the blend reduces CO emissions. This reduction is attributed to butanol's inherent oxygen content within its molecular structure. Diesel-butanol blends increase the oxygen content in the air-fuel mixture, which enhances CO oxidation and promotes more complete combustion, potentially lowering CO emissions [42]. The rise in HC emissions observed when alcohol is added to fuel blends may be linked to the higher latent heat of vaporization characteristic of alcohol blends. This higher latent heat causes slower evaporation, which in turn can result in a slower and less homogeneous fuel-air mixture [43].



(a) 3D surface plot



(b) Contour plot

Figure 7. NO_x versus butanol ratio and engine speed in (a) 3D surface and (b) Contour plot

3.4. Optimization

The optimization of engine input parameters when using butanol as a fuel can be crucial for maximizing performance and minimizing emissions. RSM (Response Surface Methodology) is a statistical technique used for optimizing processes and finding the best combination of input variables to achieve desired outputs. When applied to engine

optimization, RSM can help identify the finest engine input parameter settings for butanol-diesel fuel blends. The results of multi-purpose optimization obtained from RSM based on the principle of maximizing or minimizing output responses (Torque, Power, NOx, CO, HC).

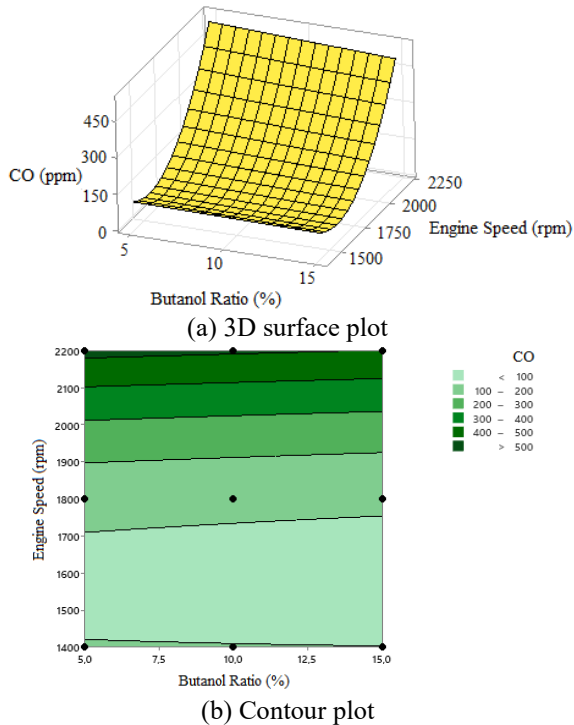


Figure 8. CO versus butanol ratio and engine speed in (a) 3D surface and (b) Contour plot

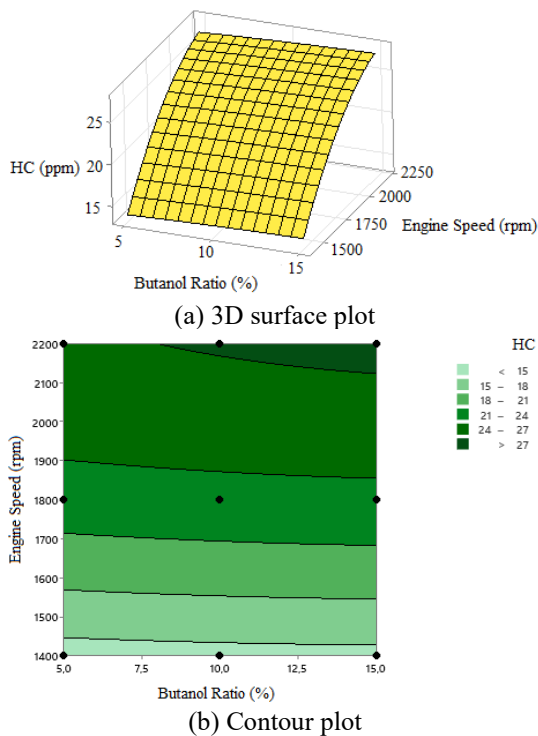


Figure 9. HC versus butanol ratio and engine speed in (a) 3D surface and (b) Contour plot

Table 10 provides the goals set for each

response, the lower and upper limits used, the weights, and the importance of the factors, which are optimization criteria. Figure 10 demonstrates the RSM optimizer outcomes. The optimum butanol ratio and engine speed were found as 5% and 1721.4 rpm, respectively.

Table 10. Details of RSM optimization

Response	Goal	Lower	Upper	Weight	Importance
Butanol Ratio (%)	In range	5	10	1	1
Engine Speed (rpm)	In range	1400	2200	1	1
Tork	Max.	702.44	848.15	1	1
Power	Max.	132.25	172.41	1	1
NOx	Min.	694	1034.00	1	1
CO	Min.	105	534.00	1	1
HC	Min.	13.81	27.48	1	1

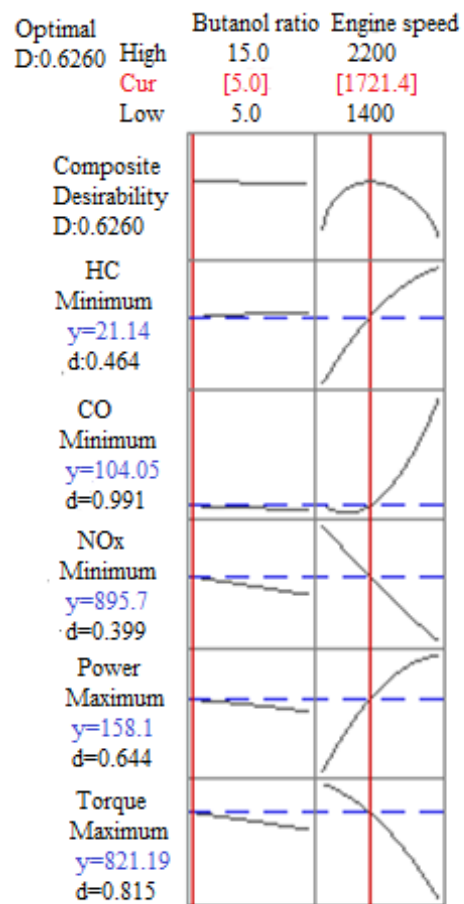


Figure 10. RSM Optimizer

4. Conclusion

In the current study, the effects of varying amounts of butanol additive and engine speed on the performance and emission characteristics of heavy-duty diesel engines have been investigated. The results obtained based on the RSM optimization approach by varying the engine speed and ratio of butanol at various levels are provided below:

- A strong agreement was observed between the experimental responses and the

predictions made by the RSM.

- The regression analysis identified a robust relationship between the independent variables and the responses, effectively explaining this relationship. The coefficient of determination R^2 for torque, power, NO_x , CO, and HC was found to be 99.02%, 99.98%, 99.67%, 99.97%, and 99.95%, respectively, which indicates the success of the model.
- The experiments conducted using Minitab software determined the optimum conditions as a butanol ratio of 5% and an engine speed of 1721.4 rpm. At these optimum conditions, the torque, power, NO_x , CO, and HC emission values were determined as 821.19 rpm, 158.1 Nm, 895.7 ppm, 104.05 ppm, and 21.14 ppm, respectively.
- Pareto charts indicate that engine speed has a more significant effect on engine responses compared to butanol ratio.
- This study emphasizes the optimization of the effects of butanol-diesel fuel blends on performance and exhaust emissions in a turbocharged diesel engine using Response Surface Methodology (RSM). The study demonstrates how factors such as butanol ratio and engine speed can be optimized to improve engine performance and reduce environmental emissions. Furthermore, the high R^2 values and ANOVA results obtained support the reliability and validity of the model. This research provides an important scientific foundation for engine optimization and the use of environmentally friendly fuels.

Credit Authorship Contribution Statement

The author accepts full responsibility for the content of this article and has approved its submission.

Declaration of Competing Interests

The author declares that there are no competing interests.

5. References

1. Zhang, Z., Li, J., Tian, J., Dong, R., Zou, Z., Gao, S., & Tan, D. "Performance, combustion and emission characteristics investigations on a diesel engine fueled with diesel/ ethanol /n-butanol blends", *Energy*, 249, 123733, 2022.
2. Wu, T., Shen, Q., Xu, M., Peng, T., & Ou, X. "Development and application of an energy use and CO2 emissions reduction evaluation model for China's online car hailing services", *Energy*, 154, 298-307, 2018.
3. Zhang, Z., Ye, J., Lv, J., Xu, W., Tan, D., Jiang, F., & Huang, H. "Investigation on the effects of non-uniform porosity catalyst on SCR characteristic based on the field synergy analysis", *Journal of Environmental Chemical Engineering*, 10, 107056, 2021.
4. Li, Y., Jia, M., Han, X., & Bai, X-S. "Towards a comprehensive optimization of engine efficiency and emissions by coupling artificial neural network (ANN) with genetic algorithm (GA)", *Energy*, 225, 120331, 2021.
5. Şahin, Z., & Aksu, O.N. "Experimental investigation of the effects of using low ratio n-butanol/diesel fuel blends on engine performance and exhaust emissions in a turbocharged DI diesel engine", *Renewable Energy*, 77, 279-290, 2015.
6. Jamrozik, A. "The effect of the alcohol content in the fuel mixture on the performance and emissions of a direct injection diesel engine fueled with diesel-methanol and diesel-ethanol blends", *Energy Conversion Management*, 148, 461-76, 2017.
7. Zhang, Z.H., Tsang, K.S., Cheung, C.S., Chan, T.L., & Yao, C.D. "Effect of fumigation methanol and ethanol on the gaseous and particulate emissions of a direct-injection diesel engine", *Atmospheric Environment*, 45, 2001-2008, 2011.
8. Tipanluisa, L., Fonseca, N., Casanova, J., & Lopez, J. "Effect of n-butanol/diesel blends on performance and emissions of a heavy-duty diesel engine tested under the World Harmonised Steady-State cycle", *Fuel*, 302, 121204, 2021.
9. Lapuerta, M., Hernandez, J., Rodríguez-Fernandez, J., Barba, J., Ramos, A., & Fernandez-Rodríguez, D. "Emission benefits from the use of n-butanol blends in a Euro 6 diesel engine", *International Journal of Engine Research*, 19(10), 1099-112, 2018.
10. Billa, K.K., Deb, M., Sastry, G.R.K., & Dey, S. "Experimental investigation on dispersing graphene-oxide in biodiesel/diesel/higher alcohol blends on diesel engine using response surface methodology", *Environmental Technology*, 43, 3131-3148, 2022.

11. Ma, Q., Zhang, Q., Liang, J., & Yang, C. "The performance and emissions characteristics of diesel/biodiesel/alcohol blends in a diesel engine", *Energy Reports*, 7, 1016-1024, 2021.
12. Atmanlı, A., İleri, E., & Yüksel, B. "Effects of higher ratios of n-butanol addition to diesel- vegetable oilblends on performance and exhaust emissions of a diesel engine", *Journal of the Energy Institute*, 88:209-220, 2015.
13. Emiroglu, A.O., & Şen, M. "Combustion, performance and emission characteristics of various alcohol blends in a single cylinder diesel engine", *Fuel*, 212, 34-40, 2018.
14. Zhu, Q, Zong, Y., Tan, Y.R., Lyu, J., Yu, W., Yang, W., & Kraft, M. "Evaluating the effect of n-butanol additive on particulate matter emission in diesel engine", *Fuel*, 332, 126003, 2023.
15. Yilmaz, N., Vigil, F., & Donaldson, B. "Effect of n-Butanol Addition to Diesel Fuel on Reduction of PAH Formation and Regulated Pollutants", *Polycyclic Aromatic Compounds*, 43, 8785-8799, 2023.
16. Doğan, O. "The influence of n-butanol/diesel fuel blends utilization on a small diesel engine performance and emissions", *Fuel*, 90, 2467–2472, 2011.
17. Bhan, S., Gautam, R., & Singh, P. "Application of response surface approach to optimize CI engine parameters fuelled by newly developed waste cooking biodiesel infused with Al₂O₃ nanoparticle", *Environmental Progress & Sustainable Energy*, 42, 14151, 2023.
18. Yaman, H., Yeşilyurt, M.K., & Uslu, S. "Combined effects of biodiesel – ULSD blends and EGR on performance and emissions of diesel engine using Response surface methodology (RSM)", *Energy Nexus*, 7, 100136, 2022.
19. Yıkımsı, S. "Effect of Thermosonication on Some Bioactive, Sensory Analysis and Microbiological Properties of Yellow Watermelon Juice Using Response Surface Methodology", *BSEU Journal of Science*, 6(2), 162-179, 2019.
20. Kumar, S.K., Surakasi, R., Patro, S.G.K., Govil, N., Ramis, M.K., Razak, A., Sharma, P., Alsubih, M., İslam, S., Khan, T.Y.M., Almakayeel, N., & Chintakindi, S. "Performance, Combustion, and Emission analysis of diesel engine fuelled with pyrolysis oil blends and n-propyl alcohol-RSM optimization and ML modelling", *Journal of Cleaner Production*, 434, 140354, 2024.
21. Esonye, C., Onukwuli, O.D., & Ofoefule, A.U. "Optimization of methyl ester production from Prunus Amygdalus seed oil using response surface methodology and Artificial Neural Networks", *Renewable Energy*, 130, 61-72, 2019.
22. Kumar, M., Gautam, R., & Ansari, N.A. "Optimisation of an experimental and feasibility research on a CRDI diesel engine based on a blend of waste cooking oil and waste plastic oil using RSM: A value addition for disposed waste oil", *Journal of the Energy Institute*, 117, 101564, 2024.
23. Sakthivel, R., Ramesh, K., Marshal, S.J.J., & Sadasivuni, K.K. "Prediction of performance and emission characteristics of diesel engine fuelled with waste biomass pyrolysis oil using response surface methodology", *Renewable Energy*, 136, 91-103, 2019.
24. Ramachander, J., Gugulothu, S.K., Sastry, G.R.K., Panda, J.K., & Surya, M.S. "Performance and emission predictions of a CRDI engine powered with diesel fuel: A combined study of injection parameters variation and Box-Behnken response surface methodology-based optimization", *Fuel*, 290, 120069, 2021.
25. Singh, D.K., Raj, R., & Tirkey, J.V. "Performance and emission of multiple engine parameters of a 1-heptanol / gasoline fuel blends operated a port-fuel injection spark ignition engine using response surface methodology approach", *Energy*, 238, 122019, 2022.
26. Dubey, A., Prasad, R.S., Singh, J.K., & Nayyar, A. "Performance and emission analysis of triple fuelled CI engine utilizing producer gas, biodiesel and diesel: An optimization study using response surface methodology", *Thermal Science and Engineering Progress*, 36, 101486, 2022.
27. Ghanbari, M., Mozafari-Vanani, L., Dehghani-Soufi, M., & Jahanbakhshi, A. "Effect of alumina nanoparticles as additive with diesel–biodiesel blends on performance

and emission characteristic of a six-cylinder diesel engine using response surface methodology (RSM)", *Energy Conversion and Management*: X, 11, 100091, 2021.

28. Sharma, A., Singh, Y., Singh, N.K., Singla, A., Ong, H.C., & Chen, W. "Effective utilization of tobacco (*Nicotiana Tabaccum*) for biodiesel production and its application on diesel engine using response surface methodology approach", *Fuel*, 273, 117793, 2020.

29. Simşek, S., & Uslu, S. "Determination of a diesel engine operating parameters powered with canola, safflower and waste vegetable oil based biodiesel combination using response surface methodology (RSM)", *Fuel*, 270, 117496, 2020.

30. Uslu, S., & Celik, M.B. "Performance and exhaust emission prediction of a SI engine fueled with I-amyl alcohol-gasoline blends: an ANN coupled RSM based optimization", *Fuel*, 265, 116922, 2019.

31. www.minitab.com

32. Kahveci, E.E., & Taymaz, I. "Hydrogen PEMFC stack performance analysis through experimental study of operating parameters by using response surface methodology (RSM)", *International Journal of Hydrogen Energy*, 47(24), 12293-12303, 2022.

33. Aziz, N.A., Awanis, N., & Noraziman, S.N. "Modified desirability function for optimization of multiple responses", *Journal of Mathematics and Computing Science*, 1(1), 39-54, 2018.

34. Hirkude, J.B., & Padalkar, A.S. "Performance optimization of CI engine fuelled with waste fried oil methyl ester-diesel blend using response surface methodology", *Fuel*, 119, 266-73, 2014.

35. Gokmen, M.S., Dogan, I., & Aydogan, H. (2021). "Investigation of the Effect of 1-Propanol / Gasoline Fuel Blends on Exhaust Emissions Using Response Surface Methodology", *European Journal of Science and Technology*, 24, 67-74, 2021.

36. Singh, V.K., Ansari, N.A., Sharma, A., Gautam, S., Kumar, M., & Singh, Y. "Exhaust gas recirculation effect on the performance of a CRDI diesel engine fuelled with linseed biodiesel/diesel blend through response surface methodology", *Proceedings of the*

Institution of Mechanical Engineers, Part C: Journal of Mechanical Engineering Science, 09544062211026348, 2021.

37. Bharadwaz, Y.D., Rao, B.G., Rao, V.D., & Anusha, C. "Improvement of biodiesel methanol blends performance in a variable compression ratio engine using response surface methodology", *Alexandria Engineering Journal*, 55(2), 1201-9, 2016.

38. Kumar, T., Mohsin, R., Majid, Z.A., Ghafir, M.F.A., & Wash, A.M. "Experimental study of the anti-knock efficiency of high-octane fuels in spark ignited aircraft engine using response surface methodology", *Applied Energy*, 259, 114150, 2020.

39. Tosun, E., Yılmaz, A.C., Ozcanlı, M., & Aydın, K. "Determination of effects of various alcohol additions into peanut methylester on performance and emission characteristics of a compression ignition engine", *Fuel*, 126, 38-43, 2014.

40. Ozgur, T. "A Study on the Performance and Emission Characteristics of a Diesel Engine Operated with Ternary Higher Alcohol Biofuel Blends", *Ingeniería e Investigación*, 43, 93696, 2023.

41. Joy, N., Balan, K.N., Nagappan, B., & Abraham baby, S.J. "Emission analysis of diesel and butanol blends in research diesel engine", *Petroleum Science and Technology*, 38(4), 289-296, 2020.

42. Kattela, S.P., Vysyaraju, R.K.R., Surapaneni, S.R., & Ganji, P.R. "Effect of n-butanol/diesel blends and piston bowl geometry on combustion and emission characteristics of CI engine", *Environmental Science and Pollution Research*, 26(2), 1661-1674, 2019.

43. Rakopoulos, D.C., Rakopoulos, C.D., Hountalas, D.T., Kakaras, E.C., & Giakoumis, E.G. "Effects of ethanol-diesel fuel blends on the performance and exhaust emissions of heavy duty DI diesel engine", *Energy Conversion and Management*, 49, 3155-3162, 2008.

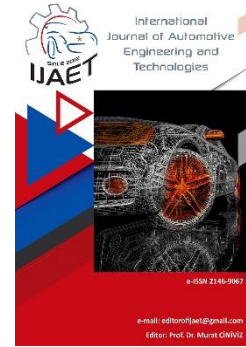


e-ISSN: 2146 - 9067

International Journal of Automotive Engineering and Technologies

journal homepage:

<https://dergipark.org.tr/en/pub/ijaet>



Original Research Article

Correlation between spark plug electrode gap and engine performance-emission characteristics in a single-cylinder petrol engine



Ali Can Yılmaz^{1*}, Özlem Erdem Yılmaz²

^{1,*}Department of Motor Vehicles and Transportation Technologies, Çukurova University, 01160, Adana, Türkiye.

²Department of Textile Technologies, Çukurova University, 01160, Adana, Türkiye.

ARTICLE INFO

Orcid Numbers

- 0000-0001-9832-9880
- 0000-0002-0976-2162

Doi: 10.18245/ijaet.1671992

* Corresponding author
acyilmaz@cu.edu.tr

Received: Apr 08, 2025
Accepted: May 27, 2025

Published: 30 Jun 2025

Published by Editorial Board Members of
IJAET

© This article is distributed by Turk Journal
Park System under the CC 4.0 terms and
conditions.

To cite this paper: Yılmaz, A.C., Erdem
Yılmaz, Ö., Correlation between spark
plug electrode gap and engine
performance-emission characteristics
in a single-cylinder petrol engine,
International Journal of Automotive
Engineering and Technologies. 2025,
14 (2), 111 – 111.
<http://dx.doi.org/10.18245/ijaet.1671992>

ABSTRACT

In this study, we conducted an experimental investigation into how five different spark plug ground electrode gap settings (0.5 mm, 0.75 mm, 1.0 mm, 1.25 mm, and 1.5 mm) affect the performance and exhaust emissions of a single-cylinder petrol engine. The experiments were conducted on a single-cylinder, four-stroke spark-ignition engine operated at constant speed and throttle, with a stoichiometric air-fuel mixture, and instrumented for in-cylinder pressure and full exhaust emission analysis. Key performance metrics including brake mean effective pressure (BMEP), brake specific fuel consumption (BSFC), and exhaust gas temperature (EGT) were assessed, along with exhaust emissions of carbon monoxide (CO), unburned hydrocarbons (HC), and nitrogen oxides (NO_x). The engine was operated at a constant speed and throttled with stoichiometric mixture to isolate the influence of spark gap. Among the tested configurations, the 1.0 mm spark gap delivered the best performance, achieving a peak brake mean effective pressure (BMEP) of 7.2 bar and the lowest BSFC of ~300 g/kWh. Emissions of CO and HC followed a U-shaped trend, minimizing at the 1.0 mm gap (CO: 0.48%, HC: 300 ppm), while NO_x peaked at this same setting (~2000 ppm) due to elevated flame temperatures. Wider gaps (1.5 mm) induced partial misfires, resulting in increased CO and HC emissions and a 17% drop in BMEP. The results confirm that spark gap size strongly influences combustion quality, and the optimal range of 0.9–1.0 mm offers a practical trade-off between efficiency and emissions. Smaller or larger gaps caused deteriorated performance: a narrow 0.5 mm gap produced weaker ignition leading to slower combustion, while an overly wide 1.5 mm gap caused partial misfires. Consequently, CO and HC emissions followed a U-shaped trend, minimizing at the ~1.0 mm gap and rising at the extreme small and large gaps because of incomplete combustion at those conditions. In contrast, NO_x emissions were the lowest at the smallest and largest gaps and peaked at the mid-gap, inversely tracking the combustion efficiency and peak temperature trends. It was concluded that a larger spark gap improves the initial flame kernel and combustion stability up to a point, beyond which ignition becomes erratic. The optimal spark plug gap ~0.9–1.0 mm achieved the best trade-off between complete combustion (low CO/HC) and high thermal efficiency/BMEP, at the cost of increased NO_x because of higher combustion temperatures.

Keywords: Spark plug gap, combustion efficiency, engine emissions, brake specific fuel consumption.

1. Introduction

Ignition by a spark plug is the initiating event for combustion in a spark-ignition engine, and the spark plug gap (distance between center

and ground electrodes) is known to critically influence the ignition process. The gap must be large enough to reliably ignite the air-fuel mixture with a strong spark, yet not so large

that the ignition voltage requirement causes misfire [1,2]. In practical engines, manufacturers specify a gap (typically around 0.6–1.1 mm in automobiles) that balances these factors. The gap effectively sets the size of the initial flame kernel; combustion in an SI engine begins with a flame kernel roughly on the order of the spark gap distance [3]. A larger gap can create a larger initial flame kernel volume and expose it to more mixture, promoting faster early flame growth [1]. However, too wide a gap may strain the ignition system's ability to produce a spark with sufficient energy and consistency, especially under high pressure conditions, potentially leading to misfires or high cycle-to-cycle variability [4]. Conversely, a very narrow gap concentrates the spark energy in a small volume and can quench the flame kernel because of proximity of the electrodes, yielding a weak or slow-burning flame [1].

Prior studies have shown that spark gap size has measurable effects on engine performance and emissions. Bas et al. [5] found that increasing the gap from 0.6 to 1.0 mm in a single-cylinder test engine enhanced the engine's power and lowered BSFC (improved fuel efficiency). Their best results were obtained with a 1.0 mm gap (using a high-energy ignition spark plug), which underscores that an optimally larger gap can improve combustion efficiency. These improvements are often attributed to the faster and more complete combustion from a larger initial flame kernel and longer spark discharge duration. On the other hand, excessively wide gaps have been linked to negative outcomes. Ozcelik and Gültekin [6] observed that when the gap of an iridium spark plug was increased beyond the stock setting (from 0.8 mm to 0.9 mm) in a small gasoline engine, the engine experienced higher cycle-to-cycle variability, resulting in increased vibration, noise, and a rise in HC emissions. This points to surpassing a certain gap threshold strains the ignition, causing incomplete combustion in some cycles. Another study by Bhaskar [7] focusing on cyclic combustion variability found that an intermediate gap (around 0.6 mm in that engine) minimized the coefficient of variation in IMEP, whereas both smaller and larger gaps caused less stable combustion. The existence

of an optimal gap for stability was also noted by Zhang and Chen [4], who showed that for a given ignition energy there is an ideal gap that maximizes flame kernel "quality" – too large a gap with insufficient ignition energy caused misfires, whereas with high ignition energy even a large gap could be used effectively. These findings collectively highlight that the spark gap has a non-linear effect: moderate increases in gap improve combustion and performance up to an optimum, beyond which further increase causes diminishing returns or adverse effects.

Spark plug gaps can also interact with fuel properties and mixture conditions. For example, in engines running lean mixtures or alternative fuels (which are harder to ignite), a larger gap can be beneficial. Dave and Shaikh [8] in a review on CNG-fueled SI engines noted that widening the spark gap (and using projected electrodes) was necessary to ignite lean CNG mixtures efficiently, thereby improving torque and efficiency in conversions of gasoline engines to gaseous fuel. Ceper [9] found similar advantages of larger gaps in a hydrogen-fueled engine, where a bigger gap extended the lean limit of operation and improved combustion completeness. These contexts emphasize that an optimal gap may depend on operating conditions: lean or high-dilution combustion benefits from a stronger spark (often achieved by a wider gap or higher ignition energy), whereas under stoichiometric conditions an extremely large gap may not yield further benefit and can induce misfire if the ignition system cannot support it.

From an emissions standpoint, the spark gap influences the formation of pollutants by altering the completeness and temperature profile of combustion. CO and HC primarily result from incomplete combustion. If the spark gap is suboptimal (too small or too large), the flame may propagate slowly or quench, leaving some fuel unburned (high HC) or only partially oxidized (high CO) [10]. Conversely, a gap that promotes a robust and timely ignition will tend to reduce CO and HC emissions by burning the fuel more completely within the cylinder [11].

NO_x emissions, however, are mainly a function of peak combustion temperature and oxygen

availability. Faster and more complete combustion (as facilitated by an optimal spark gap) usually raises the peak flame temperature, thus increasing thermal NO_x formation [12]. A trade-off often exists: the conditions that minimize CO and HC (hot, efficient combustion) tend to maximize NO_x , and vice versa. This implies that if a wider gap significantly improves combustion efficiency, one might observe lower CO/HC but higher NO_x . If the gap is too large and causes misfires, NO_x can drop drastically (because peak temperatures are never reached on misfiring cycles), while CO and HC surge because of unburnt fuel.

In summary, existing literature implies that an intermediate spark plug gap typically yields better engine performance (higher power/BMEP and lower BSFC) and lower CO and HC emissions, whereas very small or very large gaps can degrade performance and worsen incomplete-combustion emissions. NO_x emissions tend to increase with improved combustion efficiency and thus may peak at an optimal gap and decrease at the extremes. Building on these insights, the present experimental study systematically examines five gap sizes from 0.5 mm to 1.5 mm in a controlled single-cylinder gasoline engine environment. The goal is to quantify the trends in BMEP, BSFC, EGT, CO, HC, and NO_x across this range and to interpret the results in light of combustion behavior, providing a comprehensive and internally consistent picture of spark gap effects. While numerous studies have examined the influence of spark plug gap on ignition quality and engine emissions, many are limited in scope—either investigating a narrow range of gap values, focusing on a subset of engine parameters, or lacking quantitative insight into combustion stability. Additionally, the interplay between spark gap and combustion completeness is often described qualitatively, without rigorous analysis under controlled operating conditions. To address these limitations, the present study provides a systematic evaluation of five spark plug ground electrode clearances (0.5 mm to 1.5 mm) in a single-cylinder spark-ignition engine. The investigation includes simultaneous measurement of key performance metrics—BMEP, BSFC, and

EGT—alongside regulated emissions (CO, HC, NO_x), all under fixed engine speed and stoichiometric fueling. Moreover, the study introduces a quantitative assessment of misfire frequency based on in-cylinder pressure traces, offering deeper insight into combustion irregularities at extreme gap settings. The findings establish an experimentally validated optimal gap range (0.9–1.0 mm) that achieves high thermal efficiency and low CO/HC emissions, while also delineating the trade-off with NO_x formation. This integrated, gap-specific analysis provides new and practically relevant guidance for ignition system calibration in small spark-ignition engines.

2. Materials and Methods

2.1. Engine test setup

Experiments were conducted on a single-cylinder, four-stroke petrol engine designed for research use (Table 1). Fuel is supplied via port fuel injection with electronic control to maintain a stoichiometric air-fuel ratio ($\lambda \cong 1.0$) for all tests. The ignition system uses a coil-and-plug configuration with a programmable ignition timing; for all trials, the ignition timing was fixed at 28° BTDC (MBT timing for the baseline gap) to isolate the effect of gap changes. The stock spark plug is a single-electrode type (heat range suitable for this engine) originally gapped at 0.9 mm. For this study, the gap was adjusted to the specified values using feeler gauges and a calibrated bending tool. Five gap settings were tested: 0.5 mm, 0.75 mm, 1.0 mm, 1.25 mm, and 1.5 mm. These represent a range from a very tight gap to a very wide gap, spanning the range of typical automotive spark plug gaps and slightly beyond. Each gap was verified prior to installation. The same spark plug was used for all tests to keep electrode shape and orientation constant (only the ground strap was bent to adjust the gap, and a new plug was used to start, to avoid wear or deposit effects).

The engine was coupled with an eddy-current dynamometer (Schenck W130, 10 kW capacity, 0.1 Nm torque resolution) for loading. Tests were performed at a constant engine speed of 3000 ± 10 RPM and at WOT to measure maximum output (this yields a BMEP of around 6–7 bar for the baseline). For each spark gap setting, the throttle was kept

fully open and the engine was allowed to stabilize. The dynamometer was used to record torque output, from which BMEP was calculated (accounting for the displacement). Fuel flow was measured with a gravimetric fuel balance (± 0.1 g accuracy), enabling calculation of BSFC (in g/kWh). Cylinder pressure was monitored by a piezoelectric transducer (Kistler 6056A, 0.1°CA resolution) to make sure consistent combustion phasing and to detect misfires or abnormal combustion—this also provided qualitative insight into combustion speed and stability (though detailed pressure analysis is beyond the scope of this paper). An exhaust thermocouple in the exhaust manifold (just downstream of the exhaust valve) measured the EGT.

Table 1. Engine specifications

Parameter	Specification
Engine Brand & Model	Briggs & Stratton
Engine Type	Single-cylinder, four-stroke, air-cooled SI engine
Displacement Volume	400 cm ³
Compression Ratio	8.5:1
Bore \times Stroke	86 mm \times 68 mm
Rated Power	5.5 HP 3600 Rpm
Test Speed	2000 RPM (constant)
Fuel Type	Commercial unleaded gasoline (RON 95)
Ignition System	Transistorized magneto ignition
Cooling System	Forced air cooling
Measurement Mode	Steady-state, stoichiometric mixture

For emissions, a heated exhaust sampling line connected to a gas analyzer (AVL Digas 444 N-type 5-gas analyzer) bench was used (Table 2). The analyzer measured CO (vol.%) by nondispersive infrared (NDIR), O₂ (vol.%) by paramagnetic sensor, HC (ppm) by flame-ionization detector (FID), and NO_x (ppm) by chemiluminescence. Before each gap test, the gas analyzers were zeroed and spanned with calibration gases. The engine was run for several minutes at the test condition to allow emissions to stabilize (and for any transient effects to subside) before data recording. Each gap condition was tested at least twice on different days to make sure repeatability; reported data are averages of steady readings over a 30-second interval, after confirming that cycle-to-cycle variability or misfire rates were

stable. If a particular gap caused evident misfiring, longer sampling was done to get representative average emissions. The illustration of the experimental rig is shown in Fig. 1.

Table 2. Emission measurement device specifications

Parameter	Measurement Range	Sensitivity / Resolution
CO	0–10 vol.%	0.01 vol.%
HC	0–10000 ppm	1 ppm
NO _x	0–5000 ppm	1 ppm
O ₂	0–25 vol.%	0.01 vol.%

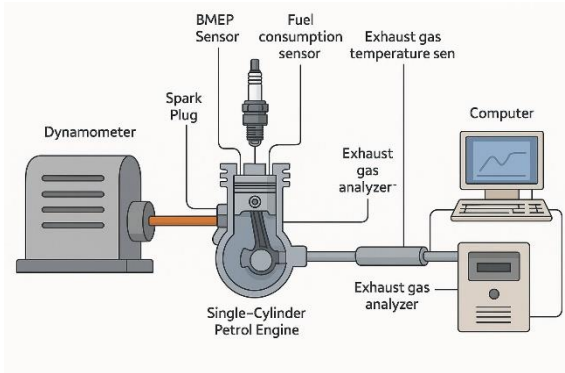


Fig. 1. Schematic of the experimental set-up

2.2. Experimental procedure

The engine was first baseline-tested at the manufacturer's recommended gap (~ 0.9 – 1.0 mm, actual measured ~ 0.95 mm). Then, the gap was reduced to 0.5 mm and gradually increased in steps: 0.75 mm, 1.0 mm, 1.25 mm, 1.5 mm (the plug was removed and regapped for each test). Between each configuration change, the engine was briefly motored and then fired to make sure any residual effects of the previous combustion conditions were minimized. Engine oil temperature and coolant temperature were kept around normal operating range ($\sim 85^\circ\text{C}$ coolant) to make sure consistency. The ignition coil's dwell time was kept constant; the coil is rated to deliver ~ 40 mJ spark energy at 0.9 mm gap – at larger gaps the delivered energy may drop if the coil cannot increase voltage sufficiently, potentially effecting the spark. We qualitatively monitored the ignition system – at 1.5 mm gap the coil was near its limit (some occasional miss sparks audible at high load), showing that this extreme gap was testing the ignition capability.

BMEP and torque (T) are directly proportional (Eq. 1) for each power stroke per revolution at 3000 RPM, so BMEP was used as a load-

normalized power metric (V_s : total swept volume of the cylinder, m^3). BSFC (g/kWh) was computed as the mass fuel flow (m_f in g/h) divided by brake power, P_b in kW (Eq. 2). The uncertainty in BSFC measurement was about $\pm 2\%$ considering fuel scale and torque sensor accuracy. Emissions were corrected for any slight differences in air-fuel ratio to make sure comparisons were at effectively stoichiometric combustion for all gaps. However, since fueling was actively control caused target $\lambda=1$, differences in CO/HC are indicative of combustion inefficiency rather than mixture changes. NO_x was measured on a dry basis and is reported in ppm at the analyzer (which correlates with g/kWh trends qualitatively). Cycle variability was observed via pressure data and noting any misfire count (an intermittent complete misfire would show up as a zero-pressure rise cycle and a sharp O_2 increase in exhaust). At the smallest and largest gaps, a few partial-burn or misfire cycles were observed, whereas the mid-gap runs were very stable. BMEP and BSFC were calculated referring to (1) and (2) [13]:

$$BMEP = \frac{4 \times \pi \times T}{V_s} \quad (1)$$

$$BSFC = \frac{m_f}{P_b} \quad (2)$$

3. Results and Discussion

3.1. BMEP, BSFC, EGT and combustion efficiency

The engine's BMEP exhibited a clear peak at an intermediate spark gap, confirming the existence of an optimal gap for maximum torque output. Fig. 2a shows that as the gap was increased from 0.5 to 1.0 mm, BMEP rose from about 6.4 bar to 7.2 bar, an increase of roughly 12%. However, when the gap was widened further to 1.25 mm, BMEP began to drop, and at 1.5 mm it fell sharply to ~ 6.0 bar, even lower than the 0.5 mm case. This non-monotonic trend aligns with prior findings that moderate gap enlargement improves combustion, but excessive gap causes misfire or slower combustion. The low BMEP at 0.5 mm is attributable to a weaker spark—a narrow gap, while easy to arc across, produces a very small flame kernel. The flame likely had a longer early growth phase and was more easily cooled by the electrodes, leading to slower

combustion and possibly incomplete burning by the time of exhaust opening. Consequently, less of the fuel's energy was converted to useful work (lower BMEP). As the gap increased to 0.75–1.0 mm, the spark could initiate a larger flame kernel that grew faster, accelerating the combustion rate. The faster heat release meant higher peak pressure closer to top dead center, improving torque. Additionally, a larger gap spark has been associated with longer spark discharge duration and higher ignition probability in borderline mixture conditions which could reduce cycle-by-cycle variability and ensure each cycle contributes good power. The 1.0 mm gap gave the highest and most consistent BMEP in our tests, which is in line with the manufacturer's gap (~ 0.9 mm) being near-optimal, and literature that found ~ 0.8 –1.0 mm optimal in similar engines [6].

When the gap was enlarged to 1.25 mm, BMEP dropped slightly ($\sim 4\%$ lower than peak). At this point, although the flame kernel was perhaps even larger, the ignition system may have been struggling – the spark might be weaker or the timing of ignition might be delayed (the ignition coil may take longer to reach breakdown voltage). There were a few detectable instances of partial-burn cycles at 1.25 mm (manifested as slightly lower pressures on random cycles). These occasional partial misfires reduce the average torque. By 1.5 mm, the situation was exacerbated: the coil was at its limit and we observed intermittent misfires (complete failure to ignite in some cycles) and frequent slow-burning cycles. The engine still ran, but with notably rough combustion. These misfires directly cause a large BMEP drop because those cycles contribute near-zero torque, dragging down the average. The result was a substantial performance deterioration at 1.5 mm gap. This agrees with the statement that a too-wide gap can lead to misfire and unstable operation [12]. In practical terms, this highlights that while a mild increase in gap from stock can be beneficial (if the ignition system is upgraded accordingly), going beyond the recommended range without sufficient ignition energy is detrimental.

BSFC showed an inverse trend to BMEP, as expected, since higher efficiency (more BMEP

per unit fuel) translates to lower BSFC. Fig. 2b presents the BSFC for each gap. It dropped from about 340 g/kWh at 0.5 mm to a minimum of 300 g/kWh at 1.0 mm, then rose steeply to ~380 g/kWh at 1.5 mm. Lower BSFC implies better fuel conversion efficiency. At the 1.0 mm gap, the engine achieved its highest thermal efficiency (around 26% if converted to efficiency), owing to the more complete and timely combustion. This represents roughly a 12% reduction in BSFC compared to the tight 0.5 mm gap – a significant improvement attributable solely to ignition differences. Indeed, the improved combustion because of larger gap shortened the combustion duration and likely allowed the engine to extract more work before the exhaust stroke. The trend of decreasing BSFC with increased gap (up to a point) is consistent with the findings of [8] for CNG operation, who observed on the order of 8–12% BSFC reduction when increasing gap from 0.6 to 0.8 mm. In our gasoline engine case, the improvement continued until 1.0 mm, reinforcing that within the stable combustion range, a bigger spark leads to more complete burning and better efficiency. However, as the gap went beyond optimal, BSFC worsened drastically. At 1.5 mm, BSFC was ~27% higher than at 1.0 mm. This large efficiency penalty is tied to the misfire and incomplete combustion issues at the wide gap. Essentially, fuel was being supplied at the same rate (since throttle and mixture were constant), but not all of it was being converted to useful work—some cycles didn't burn all the fuel (or at all), so the fuel energy was wasted (expelled as unburnt HC or as late combustion heat in the exhaust). This is evidenced by BSFC increasing (more fuel consumed per kWh of work) and will be corroborated by elevated CO/HC emissions for 1.5 mm gap (discussed later). It's worth noting that if the ignition energy could be increased (e.g., a higher-power coil or longer spark duration), the 1.25–1.5 mm gaps might have performed better [4], in our stock ignition case, though, 1.5 mm was beyond the limit.

Overall, the BMEP and BSFC results collectively indicate an optimal spark gap near 0.9–1.0 mm for this engine, which maximizes combustion efficiency and power. Gaps

smaller or larger than this optimum lead to reduced performance: small gap because of slow or incomplete combustion, and large gap because of ignition failures. The data are internally consistent; when BMEP was highest, BSFC was lowest, and vice versa, which is expected since at constant fueling, higher torque output means fuel is used more effectively, lending confidence that the measurements accurately capture the influence of spark gaps on combustion efficiency.

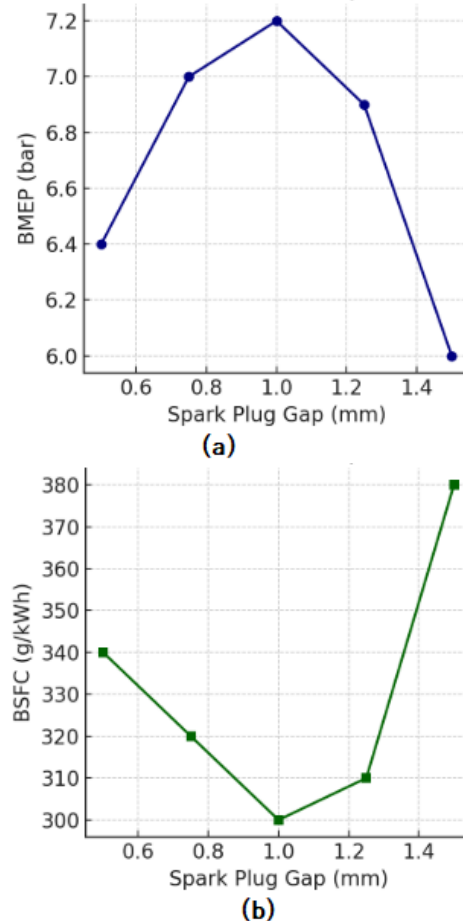


Fig. 2. Impact of spark plug gap on: (a) BMEP and (b) BSFC

The exhaust gas temperature provides additional insight into the combustion process and energy distribution. Interestingly, in our experiments the EGT decreased as the spark gap increased (Fig. 3). At the tight 0.5 mm gap, EGT was about 580°C, whereas at the optimal 1.0 mm gap it had dropped to ~540°C. With the further enlarged 1.5 mm gap, EGT was around 500°C, making the overall trend roughly a linear decline in EGT with increasing gap size. This may seem counter-intuitive at first, since one might expect that a more complete, efficient combustion (at larger gap) would release more heat. However, the key is where

that heat goes – either into useful work or out the exhaust. A high EGT at 0.5 mm reflects that a significant portion of the fuel's energy is leaving with the exhaust, likely because combustion was still incomplete or still burning during the exhaust stroke. In other words, a slow burn can push more of the heat into the exhaust rather than converting it to pressure during expansion. At 1.0 mm gap, combustion was faster and ended earlier in the cycle, allowing the gases to expand and cool more before the exhaust valve opened, thus EGT was lower despite overall higher combustion temperatures during the cycle. This implies improved conversion of fuel energy into work (and some into cylinder wall heat perhaps) rather than heat carried by exhaust. Our results mirror that—EGT went down as gap increased from 0.5 to 1.25 mm because of more complete combustion and less post-combustion heat loss.

At the extreme of 1.5 mm gap, EGT was lowest (~500°C). In this case, the low EGT is explained differently: with frequent misfires, many cycles had no combustion or very late combustion (after the exhaust opened). In a pure misfire cycle, unburnt air-fuel mixture would exhaust at near room temperature (which drastically lowers average EGT). Even partial burns would produce cooler exhaust because the burning might happen very late (some fuel may even burn in the exhaust manifold or not at all). The high CO and HC emissions observed at 1.5 mm (next section) support this interpretation. Essentially, EGT at 1.5 mm was low not because the engine was efficient (quite the opposite, BSFC was poor), but because so much fuel was not being burned at the proper time. This highlights an important point: low EGT can signify high efficiency or severe misfire, and one must use other data (BSFC, emissions) to distinguish. In our series, the monotonic decline of EGT with gap was a combination of both effects: the initial decline (580→540°C from 0.5 to 1.0 mm) signaled increasing efficiency, while the further decline (540→500°C at 1.5 mm) signaled incomplete combustion. If we had an intermediate gap like ~1.3 mm with minimal misfires, we might have seen EGT flatten out or even rise slightly if efficiency dropped without massive misfire. But at 1.5 mm, the misfire dominated.

A more efficient engine extracts more energy in-cylinder (raising indicated work and maybe coolant heat slightly) and leaves less in the exhaust. This has practical implications: a properly gapped spark plug can reduce exhaust thermal load, potentially benefiting turbocharger durability or catalyst warm-up strategies, but it might also reduce exhaust enthalpy available for turbocharging. The EGT data corroborate the BSFC findings – the 1.0 mm gap run had the highest efficiency (lowest BSFC) and indeed one of the lowest EGTs, indicative of minimal wasted heat.

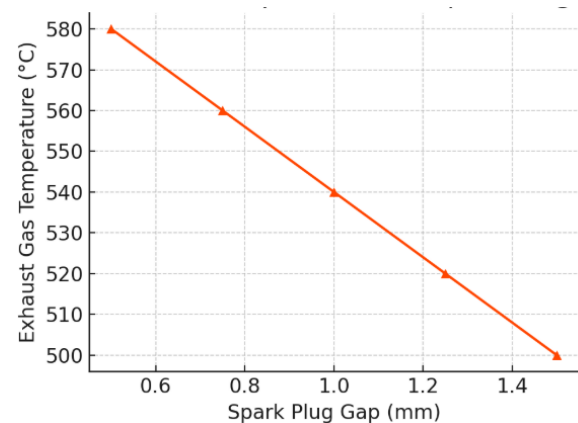


Fig. 3. EGT measured at the exhaust manifold for each spark gap

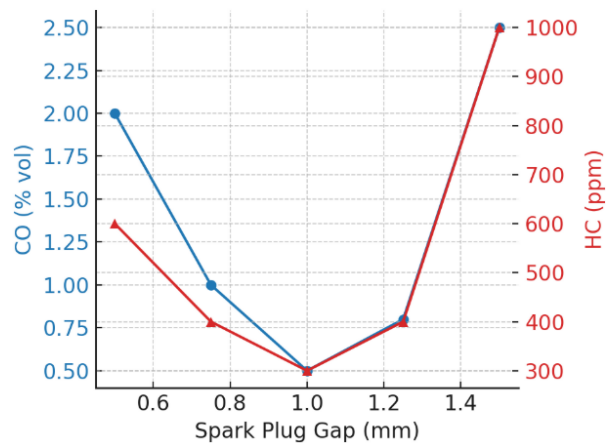


Fig. 4. CO and HC emissions as a function of spark plug gap

3.2. Assessment of CO, HC, and NOx

The emissions of CO and HC are indicators of incomplete combustion. Fig. 4 shows the measured CO (as a percentage of exhaust gas) and HC (in ppm) for the different gaps. The data show a strong dependence on spark gap, with a clear minimum in CO and HC at the 1.0 mm gap – the same gap that gave best performance. At 0.5 mm, CO was about 2.0% vol and HC around 600 ppm. As the gap was

increased to 0.75 mm, both emissions dropped markedly (CO ~1.0%, HC ~400 ppm). At the optimal 1.0 mm gap, CO reached its lowest value of 0.5%, and HC likewise hit a minimum ~300 ppm. However, when the gap was further widened to 1.25 mm, CO and HC rose again (CO ~0.8%, HC ~400 ppm), and at the extreme 1.5 mm gap they spiked to the highest levels of the series (CO ~2.5%, HC ~1000 ppm). This U-shaped pattern (high at both small and large gap, low in the middle) is a hallmark of how ignition quality affects combustion completeness. To provide a more quantitative basis for the observed emission spikes at the 1.5 mm spark gap, the misfire frequency was estimated using cylinder pressure traces recorded from the piezoelectric transducer. A cycle was considered a misfire if no discernible pressure rise was observed within the expected crank angle window after ignition. Based on 10,000-cycle data sampling, the estimated misfire rate at 1.5 mm was approximately 18 misfires per 1000 cycles (1.8%). For the 1.25 mm gap, the rate was reduced to about 5 misfires per 1000 cycles, while at 1.0 mm and lower, misfire frequency was negligible. These quantitative results correlate well with the sharp increases in CO and HC emissions at extreme spark gaps, confirming that incomplete combustion and total misfire events are the primary contributors. This also aligns with literature findings that identify misfire thresholds at high spark energy demand conditions [14].

The elevated CO and HC at 0.5 mm indicate that a significant fraction of fuel was not fully oxidized in the cylinder. Likely causes include flame quenching near the walls and electrodes because of the weak, small flame kernel, leading to pockets of unburned fuel-air mixture or partially reacted zones. A small gap might cause the flame to develop more slowly and even extinguish in the vicinity of the plug, leaving fuel that later oxidizes partially (producing CO) or exits unburnt (HC). The CO at 2% is quite high for stoichiometric combustion, suggesting some regions were effectively rich (locally fuel-rich combustion or incomplete mixing leading to CO formation). The HC of 600 ppm is also relatively high, reinforcing that not all hydrocarbons were consumed.

As the gap increased to 1.0 mm, the sharp drop in CO/HC reflects much more complete combustion. The 0.5% CO at 1.0 mm approaches what one might see in a well-tuned stoichiometric engine with near-complete combustion (some small CO presence is normal even at stoichiometry because of chemical equilibrium). The HC at 300 ppm implies a very good burn with minimal unburnt fuel (this level might be close to the limits imposed by oil-derived hydrocarbons and crevice storage effects). These minima coincide with the optimal gap that gave highest combustion efficiency, which makes sense—when the engine converts most of the fuel to CO₂ and H₂O in-cylinder, there is little CO or HC left in exhaust. In fact, at the 1.0 mm gap, the measured oxygen in exhaust was near zero and CO₂ highest, confirming almost complete combustion. The combined reduction of CO and HC underscores that the 1.0 mm gap optimizes the combustion process.

Beyond 1.0 mm, the rise in CO and HC signals the onset of incomplete combustion again, but because of different reasons than at 0.5 mm. At 1.25 mm, the increase was modest but notable, suggesting that a small fraction of cycles was not burning as well (consistent with slight BMEP decline). By 1.5 mm, CO and HC jumped dramatically. The HC level of ~1000 ppm and CO of ~2.5% indicate very poor combustion – indeed, these are values typically seen during misfire or very rich combustion. Given that our mixture was stoichiometric, rich pockets are unlikely; rather, the high CO implies partial oxidation of fuel in a lot of the cycles (e.g., the flame started but couldn't finish burning the charge, producing CO) and the extremely high HC implies many cycles where fuel remained nearly unburnt. We observed raw fuel odor and erratic running at 1.5 mm, confirming misfire. It's likely that in some cycles the mixture never ignited (contributing directly to high HC and O₂ in exhaust), and in others it ignited late and burnt incompletely (leading to CO).

In summary, CO and HC emissions were minimized at the optimal gap where combustion was fastest and most complete, and they were significantly higher at the smallest and largest gaps because of, respectively, flame quenching/slow burn and

misfire/partial burns. This U-shaped response is internally consistent with our performance data: poor combustion (low BMEP, high BSFC) at 0.5 and 1.5 mm gaps corresponded to high CO/HC, whereas good combustion (high BMEP, low BSFC) at 1.0 mm gave low CO/HC. Practically, this points to that keeping the spark plug at its proper gap is important not just for power but also for emissions; a plug gap that drifts too far (e.g., widening with wear) could significantly increase pollutant emissions.

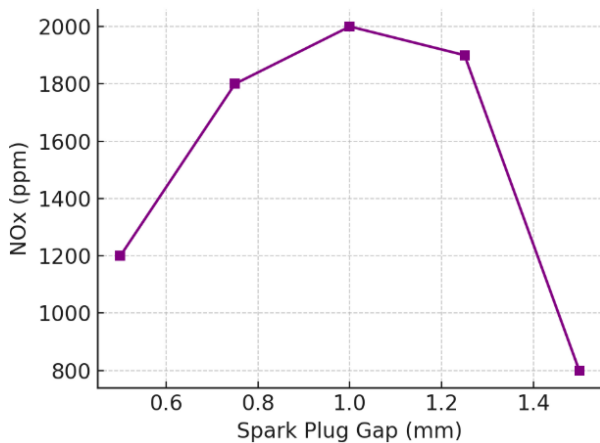


Fig. 5. NO_x emissions versus spark plug gap

The formation of NO_x is intimately tied to combustion temperature and the duration of high-temperature residence time. The measured NO_x emissions (Fig. 5) complement the story told by CO and HC. We observed that NO_x emissions were inversely U-shaped with respect to spark gap: they were relatively low at the extremes and peaked at the middle gap. Specifically, NO_x was about 1200 ppm at 0.5 mm, rose to ~2000 ppm at 1.0 mm, and then fell to roughly 800 ppm at 1.5 mm. The highest NO_x occurred at the 1.0 mm gap – the same setting that gave the most complete and hottest combustion. This is expected: NO_x (mostly NO in the exhaust) is produced via the thermal Zeldovich mechanism in the flame, which accelerates at high flame temperatures (typically significant above ~1800 K) [15-18]. When the spark gap was optimal and combustion was fast and complete, the flame temperatures likely reached their highest, promoting NO_x formation. Also, at this setting, virtually every cycle burned near perfectly, so there were many high-temperature cycles contributing to NO_x. The peak of ~2000 ppm in our single-cylinder engine at WOT

stoichiometric is in a reasonable range for NO_x (could be higher in a multi-cylinder engine with later combustion phasing optimized for NO_x, but our timing was set for torque, which tends to produce more NO_x).

At the 0.5 mm gap, NO_x was significantly lower (1200 ppm, about 40% lower than at 1.0 mm). This can be explained by the slower, less complete combustion producing lower peak temperatures and possibly longer combustion duration (which ironically can give more time for NO_x, but if temperature never got very high, the effect of time is secondary). The flame might have been cooling against surfaces and still burning during expansion, resulting in less of the high-temperature window needed for NO_x. Essentially, many parts of the mixture may have either burned at lower-than-ideal temperatures or not at all, limiting NO_x formation. Although 1200 ppm is not “low” in an absolute sense, within our context it is low relative to the optimal case. The trend that improved combustion (from 0.5 to 1.0 mm gap) increases NO_x is well-understood: other researchers have noted that strategies which reduce CO/HC (like better ignition or combustion timing) often increase NO_x because of higher combustion temperatures [1].

At the 1.5 mm gap, NO_x dropped even more dramatically to ~800 ppm, the lowest of all cases. This is clearly because of the misfires and incomplete burns at that large gap – many cycles did not reach the temperature needed to generate NO_x. When a misfire occurs, that cycle’s NO_x contribution is essentially zero (no combustion, no thermal NO_x). Even cycles that did burn likely had lower peak pressure and temperature (as indicated by lower BMEP and some late combustion), which means NO_x kinetics were much less favorable. The very high HC and CO at 1.5 mm also suggest lower combustion temperatures (as fuel didn’t fully oxidize). Thus, NO_x formation was highly suppressed. One might say the engine at 1.5 mm was “too cold” in-cylinder to make NO_x – the opposite of the 1.0 mm case which was hot and efficient but NO_x-rich. This inverse relationship between NO_x and CO/HC is a common feature of combustion systems tuning: our data reflects the classic emissions trade-off curve (often depicted as a “lean burn”

trade-off or ignition energy trade-off). When spark gap was optimal, high flame temperature and oxygen availability caused high NO_x, but when the gap was suboptimal, flame temperatures were lower or combustion incomplete, yielding lower NO_x but higher CO/HC. On the other hand, engine misfire is known to drastically cut NO_x (which is one reason vehicles with misfiring cylinders often pass NO_x emissions but fail HC/CO). Our result at 1.5 mm is essentially an example of that scenario.

Importantly, while a very low NO_x output was achieved at 1.5 mm gap, it came at an unacceptable cost of poor performance and high CO/HC. In real engine calibration, one balances these: one might not always run at the absolute NO_x-minimizing condition if it causes too much CO/HC or fuel penalty. Our results reinforce that the spark gap can be considered an emissions tuning parameter to some extent – a smaller gap might reduce NO_x but at the expense of fuel economy and HC/CO (not a favorable trade-off in most cases). Therefore, maintaining the optimal gap and controlling NO_x via other means (like EGR or aftertreatment) is the practical solution. The summary of the findings is given in Table 3.

Table 3. Summary of the results and discussion

Electrode clearance	Evaluation
Small (0.5 mm)	• Weak ignition
	• Slow flame development
	• Low BMEP
	• High BSFC
	• High CO and HC
Intermediate (0.9-1.0 mm)	• Limited NO _x
	• Enough flame kernel
	• Highest BMEP
	• Lowest BSFC
Large (1.25-1.5 mm)	• Minimum CO and HC
	• Maximum NO _x
	• High misfire tendency
	• Drastically reduced engine power
	• Soared HC/CO
	• Lowest NO _x

These observations align with the concept of a spark gap “window” for optimal engine operation. If the gap is too narrow or too wide, combustion quality suffers, albeit for different reasons. Our data empirically confirm the existence of such a window and place it around

0.9–1.0 mm for this particular engine.

It is also instructive to compare how changing the gap parallels other ways of influencing combustion. For instance, retarding ignition timing or EGR can also reduce peak temperatures and NO_x but at a fuel efficiency penalty, somewhat akin to using a smaller gap (leading to cooler, incomplete burns). On the flip side, increasing ignition energy (like using a high-energy ignition coil or multi-spark) could extend the benefits of a larger gap without the misfire drawback – effectively pushing the optimal point further out. Some modern engines and racing applications do run larger gaps (≥ 1.1 mm) in conjunction with powerful ignition systems to gain a few percentage points of efficiency.

Our results support that approach: if misfires can be avoided, a larger gap clearly improved performance and emissions (CO/HC) up to the point of ignition failure. The synergy between ignition energy and gap is highlighted by [3]: at low ignition energy, a gap of 1.2 mm was unstable, whereas at high energy it was stable. In our case, at the stock energy, 1.2 mm was barely stable and 1.5 mm unstable; a stronger ignition might make 1.5 mm viable and possibly further reduce HC/CO while maintaining low BSFC – likely at the cost of even higher NO_x unless other mitigation is used.

The emissions results also emphasize why regular maintenance of spark plugs (to make sure proper gap) is important. Over time, electrode erosion widens the gap; a plug that erodes from 0.9 mm toward 1.5 mm will gradually cause the engine to experience the symptoms we saw: rising HC/CO emissions, misfire, loss of power, and poor fuel economy. This study quantifies how bad it can get at 1.5 mm – effectively a severely worn plug scenario. It also quantifies the other extreme of a too-narrow gap which might occur if a plug is accidentally gapped incorrectly or if a maladjustment occurs.

The optimal gap delivered the best combination of low fuel consumption and low incomplete combustion products (HC, CO) because of superior flame propagation, whereas suboptimal gaps caused a loss in one or more aspects (either efficiency or emissions or both). The increase of NO_x with improved

combustion is expected from the temperature sensitivity of NO_x formation.

Each measurement (BMEP, BSFC, EGT, CO, HC, NO_x) supports the explanation for the others, giving a coherent overall interpretation. We also cross-validated our findings with literature at each step, finding good qualitative and quantitative agreement, which adds confidence that these trends are broadly applicable to SI engines (with potential shifts in the exact optimal gap depending on ignition system strength and engine geometry).

4. Conclusions

This experimental investigation assessed the influence of spark plug gap on engine performance and emissions using a single-cylinder petrol engine, with five discrete gap settings from 0.5 mm up to 1.5 mm. The following key conclusions are drawn, all of which are supported by the observed data and align with prior research:

- **Optimal gap for performance:** There exists an optimal spark plug gap (around 0.9–1.0 mm in this engine) that maximizes combustion efficiency. At this gap, the engine achieved the highest BMEP (~7.2 bar) and lowest BSFC (~300 g/kWh), corresponding to the best fuel conversion efficiency. Gaps smaller or larger than this optimal caused a decline in performance (up to ~17% lower BMEP and ~27% higher BSFC at 0.5 mm and 1.5 mm gaps) because of suboptimal combustion dynamics. This confirms that proper gap setting is critical for peak engine output.
- **Effect of small vs large gaps:** A too-small gap (0.5 mm) produced a weak spark that caused slower, prolonged combustion and partial flame quenching. This caused incomplete fuel burn – evidenced by higher CO (2.0%) and HC (~600 ppm) – and a loss of power. A too large gap (1.5 mm) exceeded the ignition system's capability, causing frequent misfires and very erratic combustion. This drastically increased HC (~1000 ppm) and CO (~2.5%) emissions and reduced BMEP. Thus, both extremes caused higher levels of incomplete combustion by different mechanisms (flame quench vs. misfire). The engine operated best in a moderate gap range where the spark was strong enough to ignite

the mixture reliably but not so demanding as to fail ignition.

- **CO and HC emissions minimization:** The study showed that CO and HC emissions can be minimized by using the optimal gap. At 1.0 mm gap, CO dropped to 0.5% and HC to ~300 ppm – roughly half to one-third of the values at the extreme gaps. This underscores that proper spark gapping improves combustion completeness, significantly reducing these harmful emissions. It was shown that deviating from the ideal gap in either direction will raise CO/HC because of less complete combustion.
- **NO_x emissions trade-off:** NO_x emissions were found to be inversely related to CO and HC with respect to gap changes. The highest NO_x (~2000 ppm) occurred at the 1.0 mm gap where combustion was hottest and most efficient, whereas NO_x was much lower at 0.5 mm and 1.5 mm because of cooler combustion or misfire. This highlights the classic trade-off: optimizing fuel efficiency and low CO/HC tends to increase NO_x due to higher combustion temperatures. Any ignition improvement strategy (like widening gap or increasing spark energy) should therefore consider NO_x mitigation (e.g., via EGR or spark timing adjustments) if necessary.
- **Exhaust temperature and energy distribution:** As the spark gap was optimized, exhaust gas temperature decreased (580°C at 0.5 mm to 540°C at 1.0 mm) showing more energy converted to work and less wasted as exhaust heat. Extremely large gap caused low EGT (~500°C) primarily because of misfire (unburnt mixture cooling the exhaust). Thus, EGT data corroborate the shift in energy utilization – efficient combustion yields cooler exhaust despite higher internal temperatures, whereas misfire yields cool exhaust because of lack of combustion.
- **Consistency with literature:** All observed trends – improvement of power and efficiency with increasing gap up to an optimum, U-shaped CO/HC responses, and opposite NO_x behavior – are consistent with previously published experimental studies. This consistency lends validity to the results. It also points to that the findings are generalizable to other SI engines: typically, an optimal gap exists near manufacturer spec, and

significant deviation will hurt performance and/or emissions.

- Practical implications: Maintaining the spark plug at its proper gap is essential for sustained engine performance and emissions compliance. A gap that becomes too wide with wear will cause misfires, increased fuel consumption, and high HC/CO emissions as our 1.5 mm results vividly show. Similarly, using an incorrect (too small) gap setting to “fix” misfires can actually degrade efficiency and is not recommended except to resolve very specific ignition problems. Engine tuners may exploit a slightly larger gap (within the ignition system’s capability) to gain efficiency and power, as evidenced by the gains from 0.5→1.0 mm in this study but should monitor for NO_x increases and ensure the ignition energy is sufficient to avoid misfire.

In conclusion, the spark plug gap exerts a significant influence on the combustion process in SI engines. By providing a larger initial flame kernel, a properly widened gap can enhance flame propagation, improve engine efficiency, and reduce incomplete combustion emissions (CO, HC). However, exceeding the ignition system’s limits with an overly large gap leads to instability and performance collapse. There is therefore an optimal gap range that yields the best compromise. The experimental results presented in this paper quantify these effects in detail for a single-cylinder engine, reinforcing the importance of ignition system optimization as a means to improve engine performance and emissions. Importantly, the study introduces a quantitative analysis of misfire frequency, strengthening the causal link between gap-induced combustion instability and emission behavior. These results define a practical and experimentally validated spark plug gap range (~0.9–1.0 mm) that balances engine performance with emissions compliance. The findings provide both a methodological advancement and an actionable recommendation for engine designers and calibration engineers seeking to optimize ignition systems under modern emissions constraints. Future work could explore coupling a high-energy ignition source with larger gaps to see if the benefits can be extended without incurring misfire, as well as

testing at different engine speeds, loads, and with lean mixtures to map out a full regime of gap effects. In addition, future investigations could benefit from examining the combined effects of spark plug gap size and ignition energy level on combustion performance and emissions. As spark energy demand increases with gap size, a controlled increase in ignition energy may counteract misfire tendencies or extend the stable gap range. Conversely, elevated ignition energy may exacerbate NO_x formation under stoichiometric or lean conditions. A detailed parametric study across a matrix of gap–energy combinations would provide valuable insight into the optimal ignition strategies for advanced SI engine operation. Nevertheless, the trends observed here serve as a valuable guideline for engineers and researchers in understanding and leveraging spark plug gaps as a tunable parameter in engine design and maintenance.

Nomenclature

Symbol Description

BMEP	Brake Mean Effective Pressure (bar)
BSFC	Brake Specific Fuel Consumption (g/kWh)
EGT	Exhaust Gas Temperature (°C)
CO	Carbon Monoxide (%)
HC	Unburned Hydrocarbons (ppm)
NO _x	Nitrogen Oxides (ppm)
T	Brake Torque (Nm)
N	Engine Speed (RPM)
V _s	Swept Volume or Displacement Volume (m ³)
P _b	Brake Power Output (kW)
m _f	Fuel Mass Flow Rate (g/h)
λ	Air-Fuel Ratio Equivalence Ratio

CRedit Taxonomy

Ali Can YILMAZ: Investigation, Conceptualization, Supervision, Writing-original draft, Writing-Review & Editing; Ozlem ERDEM YILMAZ: Investigation, Validation, Data curation, Formal analysis

Declaration of Competing Interest

The authors declare that they have no known competing financial interests or personal relationships that could have appeared to influence the work reported in this paper.

5. References

1. Badawy T, Bao Z, Xu H. "Impact of spark plug gap on flame kernel propagation and engine performance", *Applied Energy*, Volume: 191, pp: 311–327, 2017.
2. Yang Z et al. "The optimization of leading spark plug location and its influences on combustion and leakage in a hydrogen-fueled Wankel rotary engine." *International Journal of Hydrogen Energy*, Volume: 48, pp: 20465-20482, 2023.
3. Giménez B, Melgar A, Horrillo A, Gabana P. "Prediction of the flame kernel growth rate in spark ignition engine fueled with natural gas, hydrogen and mixtures", *Fuel*, Volume: 339, pp: 126908, 2023.
4. Zhang X, Chen L. "The synergy effect of ignition energy and spark plug gap on methane lean combustion with addressing initial flame formation and cyclic variation", *ACS Omega*, Volume: 8, Issue: 7, pp: 7036–7044, 2023.
5. Bas O, Akar MA, Serin H, Ozcanli M, Tosun E. "Variation of spark plug type and spark gap with hydrogen and methanol added gasoline fuel: Performance characteristics", *International Journal of Hydrogen Energy*, Volume: 45, Issue: 38, pp: 26513–26521, 2020.
6. Ozelik Z, Gultekin N. "Effect of iridium spark plug gap on emission, noise, vibration of an internal combustion engine", *International Journal of Energy Applications and Technologies*, Volume: 6, Issue: 2, pp: 44–48, 2019.
7. Bhaskar HB. "Effect of spark plug gap on cycle-by-cycle fluctuations in four stroke spark ignition engine", *International Journal of Innovative Research and Development*, Volume: 5, Issue: 11, pp: 85–90, 2016.
8. Dave DM, Shaikh MA. "Effect of ignition parameters for enhancement of performance and emissions of a four stroke single cylinder SI engine fuelled with CNG: a technical review", *International Journal of Engineering Research & Technology*, Volume: 2, Issue: 4, pp: 2354–2358, 2013.
9. Ceper BA. "Experimental investigation of the effect of spark plug gap on a hydrogen fueled SI engine", *International Journal of Hydrogen Energy*, Volume: 37, Issue: 22, pp: 17310–17320, 2012.
10. Tucki K, Orynych O, Mieszkalski L, Reis JG, Matijošius J, Wocial M, et al. "Analysis of the influence of the spark plug on exhaust gas composition", *Energies*, Volume: 16, Issue: 11, Article: 4381, 2023.
11. Shaikh MA, Dave DM, Vala DJ. "Optimization of ignition parameters for enhancement of performance and emissions of a four-stroke single cylinder si engine fueled with CNG", *International Journal for Scientific Research & Development*, Volume: 1, Issue: 3, 2013.
12. Birkavs A, Smigins R. "Effect of single-contact spark plug electrode gap on composition of engine exhaust emissions", *Engineering for Rural Development*, Volume: 20, pp: 353–358, 2021.
13. Doppalapudi AT, Azad AK, Khan MMK. "Exergy, energy, performance, and combustion analysis for biodiesel NO_x reduction using new blends with alcohol, nanoparticle, and essential oil." *Journal of Cleaner Production*, Volume: 467, pp: 142968, 2024.
14. Heywood J. "Internal combustion engine fundamentals", 2nd edition, McGraw-Hill, 2018.
15. Zeldovich YB. "The oxidation of nitrogen in combustion explosions", *Acta Physicochimica U.S.S.R.*, Volume: 21, pp: 577–628, 1946.
16. Dehai Y, Chen Z. "Premixed flame ignition: Theoretical development." *Progress in Energy and Combustion Science*, Volume: 104, pp: 101174, 2024.
17. Xiangtao L et al. "Nitrogen sources and formation routes of nitric oxide from pure ammonia combustion." *Energy*, Volume: 315, pp: 134455, 2025.
18. Baris O. "Prediction of NO_x emissions for hydrogen combustion engines using thermodynamical model in steady and transient conditions." *International Journal of Hydrogen Energy*, Volume: 110, pp: 138-143, 2024.

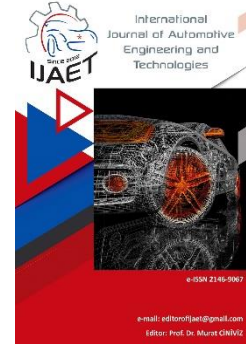


e-ISSN: 2146 - 9067

International Journal of Automotive Engineering and Technologies

journal homepage:

<https://dergipark.org.tr/en/pub/ijaet>



Review Article

Investigation of changes in body-in-white components and their impact during the transition from internal combustion engine vehicles to electric vehicles

Murat Onat^{1*}

^{1,*} TOYOTETSU Turkey, Kocaeli, 41420, Türkiye.



ARTICLE INFO

Orcid Numbers

1. 0000-0002-9602-3893

Doi: 10.18245/ijaet.1630727

* Corresponding author
onatm@toyotetsu.com.tr

Received: Jan 31, 2025
Accepted: Jun 28, 2025

Published: 30 Jun 2025

Published by Editorial Board Members of
IJAET

© This article is distributed by Turk Journal
Park System under the CC 4.0 terms and
conditions.

To cite this paper: Onat, M.,
Investigation of changes in body-in-
white components and their impact
during the transition from internal
combustion engine vehicles to electric
vehicles, International Journal of
Automotive Engineering and
Technologies. 2025, 14 (2), 112 – 130.
<http://dx.doi.org/10.18245/ijaet.1630727>

ABSTRACT

In this study, the impact of improvements and modifications to the chassis framework components, referred to as the Body-in-White (BIW), during the transition from internal combustion engine (ICE) vehicles to electric vehicles (EVs) is examined. Additionally, the material requirements and structural differences compared to ICE vehicles are analyzed. In this context, the literature has been reviewed and presented in a structured flow. The battery requirement of EVs emerges as a factor that increases weight compared to internal combustion engine vehicles. Although advancements in battery technologies have improved the maximum driving range of vehicles, they remain insufficient on their own, necessitating additional efforts towards vehicle lightweighting. The integration of these lightweighting efforts with new technologies has paved the way for the development of new production methods and assembly techniques. Studies examining the compliance of evolving vehicle structures with safety standards, as well as the impact of weight reduction on vehicle emissions, highlight the necessity of addressing this transformation holistically. Therefore, this study investigates the body-in-white structures of vehicles produced by various manufacturers, closely analyzing the changes in materials, weight reduction, and safety considerations during the ICE to EV transition process. Furthermore, the new production methods—such as pressing, welding, and assembly technologies—that companies have integrated into their mass production lines to contribute positively to this transition process and weight reduction have become another focal point of research. These innovations in part manufacturing methods have also played a significant role in the evolution of the body-in-white concept during the ICE to EV transition.

Keywords: Body-in-White; Electrical Vehicle; Internal Combustion Engine; Light weight Design.

1. Introduction

The historical development of EVs can be traced back to the early 19th century. It is

known that in 1828, Ányos Jedlik created a model car powered by a small electric motor, followed by Robert Anderson's prototype electric car in 1832, which ran on non-

rechargeable primary batteries and could reach a maximum speed of 12 km/h [1,2]. In 1835, Thomas Davenport produced an electric motor-powered vehicle, which is now considered a cornerstone in the history of electric vehicles [3].

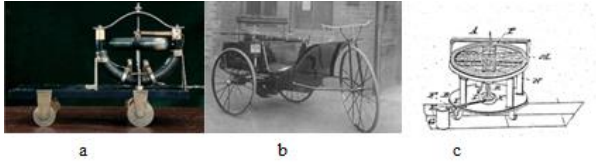


Figure 1.1 Examples of early EVs (A: 1828 Jedlik design, B: 1832 Anderson design, C: 1834 Davenport DC motor) [4,5,6]

Following the development of the electric motor, the idea of using these motors to provide propulsion for vehicles emerged. Between 1897 and 1900, EVs outnumbered ICE vehicles, accounting for 28% of all cars [7]. These early vehicles allowed electric cars to be briefly more popular than fossil fuel-powered engines. However, the advancement of internal combustion engines and the easy access to petroleum caused EVs to fall largely into the background by the early 20th century. General Motors' release of the EV1 prototype in 1996 reignited hope for EVs, gaining significant popularity almost immediately [8]. Other major automakers, including Ford, Toyota, and Honda, also produced electric vehicles. The Toyota Prius, introduced to the Japanese market in 1997, became the world's first mass-produced hybrid electric vehicle (HEV) [9].

EVs have rapidly evolved into a growing global market. Significant progress has been made, particularly in EV powertrain technologies and energy efficiency, which are seen as key components of the evolution and transformation of these vehicles. This increase in efficiency has also been an important factor in extending the maximum driving range of the vehicle [10]. In addition to advancements in powertrain technologies and energy efficiency, improvements and modifications to the chassis framework components, known as the BIW, during the transition from ICE vehicles to BEVs, have been shown to have significant impacts on both road and battery efficiency. This study examines the effects of these systems, as well as the material requirements and structural differences compared to ICE-

supported vehicles. The current range of steel used in vehicles addresses safety concerns in the front, side, and rear body designs. However, with evolving technological needs, the use of aluminum and magnesium has been steadily increasing. Furthermore, the development of plastics and composites in body design is encouraged, as they demonstrate good performance in pedestrian collision scenarios, opening the door to research into effective recycling solutions for these materials [11].

2. Materials and Methods

2.1 BIW concept and its role in the ICE to EV transition process

In the literature, BIW refers to the stage in automotive manufacturing where the body structure is assembled before the installation of components such as the engine, chassis, and other subsystems. It is also referred to as the "white body" or "unpainted body" process. This phase involves methods like assembly, welding, riveting, and laser brazing to form the vehicle body [12].



Figure 2.1 BIW design and monocoque structure [12]

As the primary load-bearing structure, the BIW constitutes a significant portion of the vehicle's weight. Reducing BIW weight contributes directly to the overall mass reduction of vehicles. The BIW is a highly complex and extensive system, so its design must take into account various disciplines, such as structural durability, stiffness, noise, vibration, and safety performance. The traditional body design process, including both preliminary and technical design phases, is often complex. During the transition from ICE to BEVs, the automotive industry faces two major challenges:

1. Meeting safety standards
2. Reducing emissions, improving fuel efficiency, and controlling pollution

While some advancements have been made in

battery, motor, and control technologies, development continues in light of technological progress. In this context, automotive lightweighting has emerged as an effective and relatively straightforward solution to address these challenges. Lightweight vehicles have taken a prominent position in 21st-century automotive technology development and have become a hot topic of research [13].

Reducing vehicle weight has become a key area of research in the automotive industry. To lower development costs and shorten the time-to-market for new vehicles, it is crucial to optimize BIW design during the concept design phase [14].

In this context, vehicle chassis components are typically divided into three main sections:

1. Front engine compartment
2. Passenger cabin
3. Rear trunk

Each section has its own specific purpose and characteristics. The BIW is produced using sheet metal, which is shaped into the desired form and then joined using spot welding. The resulting structure is highly rigid, and since it operates as a unified system, it is referred to as a monocoque. The monocoque distributes the dynamic loads of normal vehicle operations across its entire surface, making it a highly intricate structure. In the event of a crash, the monocoque transfers forces through side rails or lateral elements to the base and roof structures. In modern vehicles, the engine compartment is used as a crumple zone, designed to absorb energy during a collision and slow down the vehicle [15]. The objectives that automakers aim to achieve as part of the BEV transition can be examined under key themes.

2.2 Meeting safety standards

The expectations from safety regulatory bodies, such as the U.S. National Highway Traffic Safety Administration (NHTSA), the European Safety Council, and other safety oversight organizations, are that vehicles continue to be built in a way that ensures greater safety for passengers. At the same time, automakers are increasingly focused on enhancing the safety of travel. One of the challenges faced by manufacturers of BEVs is

protecting the battery with minimal weight increase due to its addition. Typically placed in the lowest part of the vehicle, the battery pack must be shielded from all potential leaks while also maintaining thermal stability in the event of a crash, as any breach could pose a serious fire hazard [16]. In terms of vehicle body designs, the front and rear sections of electric vehicles exhibit several differences when compared to ICE vehicles. These differences can vary depending on the production platform, brand, and model of the vehicle. At the core of these differences are crash tests conducted to ensure safety and the structural integrity of the vehicle body. EVERSAFE conducted frontal crash tests on two first-generation vehicles (Volvo C30 and Toyota Yaris), examining how differences in the design of the front bumper impact vehicle safety.

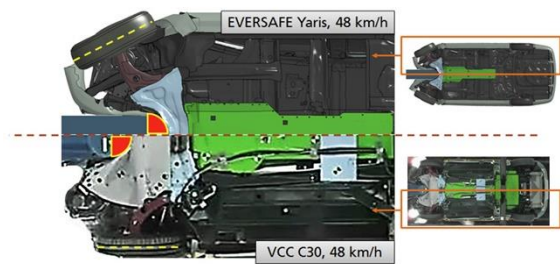


Figure 2.2 Eversafe front crash test (Top: Toyota Yaris, Bottom: Volvo C30) [16]

As part of the test, both vehicles crash into a fixed barrier at a speed of 48 km/h, with the impact directed at the center of the vehicle. Since first-generation EVs were the initial transition from ICE vehicles, their body compositions had significantly more similarities with ICE vehicles compared to the current generation of EVs. Many of these early EVs still had a transmission tunnel underneath the vehicle, and their BIW structures remained largely unchanged. According to this crash test, first-generation EVs converted from ICE vehicles failed to provide adequate stabilization in the front area. The absence of powertrain components and the engine block, which are present in ICE vehicles, resulted in increased deformation. When comparing the two vehicles, it was observed that the front bumper and attached components of the Volvo C30 more effectively transmitted the impact force. This finding indicates that the front bumper designs in EVs need to be improved to

enhance protection for the centrally located battery within the vehicle body [16].

2.3 Reducing emissions, fuel efficiency and pollution control

To combat climate change, the Paris Climate Agreement was established in 2015 with the goal of reducing global warming. One approach to lowering greenhouse gas (GHG) emissions is the adoption of BEVs. This can decrease emissions per kilometer by up to 40% when renewable energy is used to power BEVs during their operational phase [17].

Vehicles, particularly in countries where demand for automobiles is growing, are among the most polluting sources globally. Since 2000, China has experienced a rapid increase in automobile usage, reaching a growth rate of 17.5% [18]. Reducing fuel consumption is the only way to control GHG emissions, as 97% of automobile-related GHG emissions stem from the combustion process, which is directly tied to fuel consumption [19].

Figure 2.3 above illustrates the fuel consumption pathways and the outcomes of vehicle technologies for mid-sized sedans. The current technology assesses fuel production and vehicle technologies using existing raw materials and process fuel mixes. Future technologies, on the other hand, represent advanced powertrain technologies and low-emission fuel pathways. In this context:

Black Line: The GHG emissions associated with current technology for the respective pathways.

Red Line: Projected future vehicle efficiency gains. The fuel economy improvement estimates are based on the adoption of advanced vehicle and powertrain technologies within the 2030-2035 timeframe. For electric vehicles, this line represents the state of a vehicle using the U.S. electric grid mix in 2035 with projected future technology gains.

Blue Line: The GHG emissions associated with the production of future technology vehicles, amortized over the vehicle's lifetime. This represents the lifecycle GHG emissions from vehicle manufacturing, assuming the vehicle operates at 0 gCO₂e/mile fuel. The vehicle production assumptions here use baseline assumptions for the electric grid mix, materials, and vehicle production practices from the GREET model, and do not consider additional solutions such as electrification or the use of low-carbon fuels for vehicle manufacturing decarbonization.

Downward Arrows: Potential GHG emissions reductions from low-carbon fuels and electricity in addition to vehicle efficiency gains. The gap between the arrows and lines can be considered the lifecycle emissions associated with fuel cycles or vehicle operation [20].

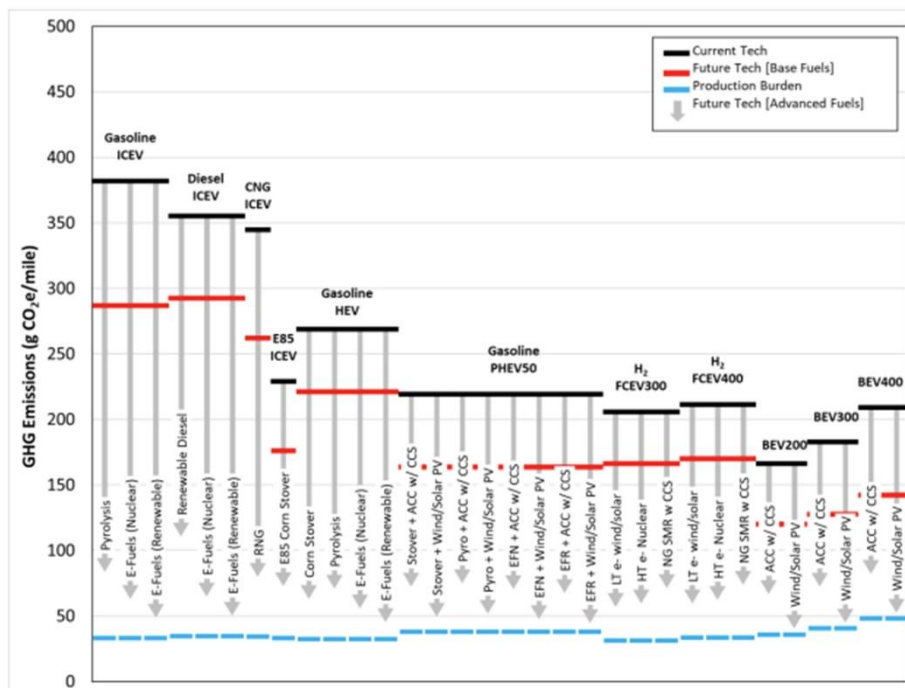


Figure 2.3 Fuel consumption rates for mid-sized sedans according to technological developments [20]

The use of lightweight BIW structures produced from aluminum and advanced high-strength steel, which are increasingly employed in the transition from internal combustion engines to electric vehicles, significantly reduces greenhouse gas emissions. Furthermore, the utilization of aluminum in BIW contributes to substantial reductions in life cycle energy consumption and greenhouse gas emissions, while advanced high-strength steels achieve greater energy savings per unit mass [21]. The substitution of steel with aluminum in automotive bodies demonstrates significant potential for increasing energy efficiency and reducing CO₂ emissions [22]. However, the adoption of aluminum in the automotive industry faces several challenges, including high material costs, the design of safety structures, advanced manufacturing technologies, and supply chain issues [19].

2.3.1 Vehicle dynamics

Vehicle dynamics and behavior are among the characteristics significantly influenced by vehicle weight on performance. Many driving parameters, such as cornering stability, responsive suspension, high-speed stability, acceleration, and braking, are directly dependent on the vehicle's weight [23]. Also, the total vehicle mass has a direct impact on performance by increasing inertia, contributes to environmental effects by accelerating tire and road wear, and affects fuel efficiency due to the higher engine load [24]. Vehicle longitudinal dynamics describe the movement and response of a vehicle along its longitudinal axis. This motion encompasses various factors, including acceleration, deceleration, velocity, position, and the forces influencing the vehicle's behavior [25].

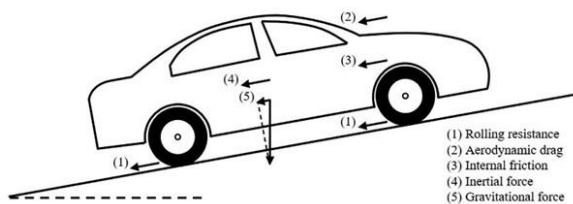


Figure 2.4 Illustration of the different factors affecting vehicle driving resistance [25]

The total tractive force F_t is given by:

$$F_t = F_r + F_a + F_d + F_g \quad (1)$$

In this equation F_t represents total tractive force (N) which sum of F_r rolling resistance force (N), F_a acceleration resistance force (N), F_d aerodynamic drag force (N) and F_g gravitational force (N)

The rolling resistance at the wheels, is given by:

$$F_r = f \times m \times g \quad (2)$$

Where m represent vehicle mass (kg) and g represent acceleration due to gravity (m/s^2)

The acceleration resistance is given by:

$$F_a = m \times a \quad (3)$$

Where a represent vehicle acceleration (m/s^2)

The aerodynamic drag, is given by:

$$F_d = \frac{1}{2} C_D \times \rho_{air} \times v^2 \times A \quad (4)$$

Where C_D represent drag coefficient, ρ_{air} represent air density (kg/m^3), v represent vehicle speed (m/s) and A represent vehicle frontal area (m^2)

Gravitational force is given by;

$$F_g = m \times g \times \sin(\alpha) \quad (5)$$

Where α represent road grade($^\circ$)

Rolling resistance coefficient is given by:

$$f = a + bv + cv^4 \quad (6)$$

In equation (6), the coefficients usually have the following values for passenger car tire [26]:

$$a = 0,4$$

$$b = 2,5 \times 10^{-5}$$

$$c = 3,5 \times 10^{-10}$$

The previous equations clearly indicate that the primary sources of resistance are directly dependent on the mass (m).

This situation leads to improved damping characteristics in roll motions, thereby benefiting driving dynamics. With reduced weight, inertial masses decrease during rolling and yawing movements, positively affecting steering control and the vehicle's overall handling behavior [27].

2.3.2 Passive Safety

Weight reduction through material substitution and compact packaging has significant effects on safety [28]. Detailed CAE (Computer-Aided Engineering) analyses Noise, Vibration, and Harshness (NVH), crash tests, and the durability of structures demonstrate the safety of lightweight structures [29]. Passive safety systems are activated when a crash becomes inevitable. Honeycomb structures have provided lighter and much safer options for

advanced vehicles. These structures can be made from aluminum and various thermoplastic materials. The application of honeycomb structures depends on the required level of safety and whether they are used on the exterior or interior of the vehicle. As illustrated in Figure 2.5 below, the use of honeycomb structures clearly shows the advantage of absorbing a large portion of the impact energy [30].

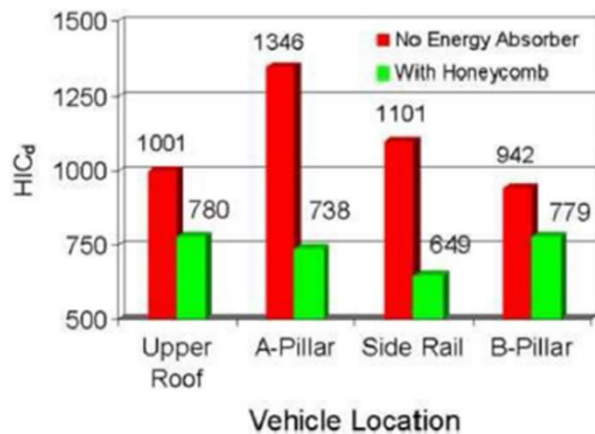


Figure 2.5 Impact absorption responses of honeycomb structures based on vehicle chassis regions [30]

A lightweight material not only reduces the weight of the BIW but also minimizes the risk to both the occupants inside and those around the vehicle [31]. The BIW structure, designed with multi-material usage, has enhanced performance while successfully reducing both weight and cost. By combining aluminum extrusions, castings, and steel press-formed parts, the structure maximizes stiffness while minimizing weight. The selection of multiple materials in BIW manufacturing offers the best optimization in terms of material cost and strength, rather than choosing a single material for the entire body [32]. The adoption of a multi-material approach has led to a 35% reduction in vehicle body weight [19].

2.4 Weight reduction and BEV material usage

Weight reduction in automotive research is not only limited to conventional fossil fuel vehicles but also extends to the rapidly developing electric and FCEV [19]. In recent years, numerous studies on lightweight automotive body components and BIW structures have been conducted and published. Many of these studies have shown excellent potential for reducing mass while maintaining performance. Achieving significant weight

reductions in vehicle packaging, while preserving safety and performance, requires substantial changes in the body assembly and paint workshops. To avoid multi-material joints and galvanic corrosion issues, material selection in the design of lightweight vehicle BIW structures is typically limited to a single material, leading to "all-steel" or "all-aluminum" designs [33]. To keep the processing methods as simple as possible and the final product prices as low as possible, special high-strength steels began to be developed in the last decades of the 20th century. Compared to conventional steel, these new materials have much higher strength and meet the required levels for cutting, forming, and weldability [34]. In this context, the percentage of hot-stamped components in BIW structures is steadily increasing. A clear example of this trend can be observed in the evolution of Volvo's BIW design. In 2002, only 7% of the first-generation XC90 SUV was made from hot-stamped steel; these components were particularly used in the B-pillars and bumper beams. By 2015, this figure had risen to 38% in the second-generation XC90, with more parts being produced using Ultra High Strength Steel (UHSS). In 2015, around 360 million hot-stamped steel parts were produced, representing a significant increase from the 124 million parts produced in 2010 [35].

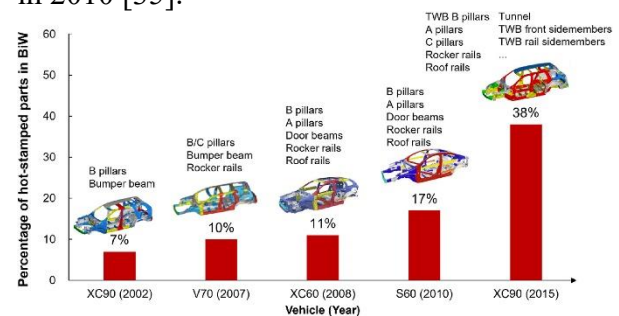


Figure 2.6 Use of hot-stamped components in Volvo [35]

The rise of BEVs represents another factor in the growth of the hot stamping market. Due to the weight of the battery itself and the increasing demand for the protection of the battery pack, the curb weight of a typical BEV is approximately 10% higher than that of an internal combustion engine vehicle [36]. This increases the need for weight reduction, making hot stamping a more prominent option for BEVs. According to a recent report,

automaker Hyundai Motors uses hot-stamped steel in approximately 15% of all steel components in its internal combustion engine vehicles, while this figure rises to 20% for electric vehicles. With the growing need for lightweight solutions in automobile manufacturing, third-generation advanced high-strength steels (AHSS) have been introduced. The design of 3rd Generation AHSS provides both exceptional mechanical properties such as strength and ductility at reduced thickness while maintaining superior safety standards compared to the first-generation AHSS. Additionally, these steels overcome issues such as the high costs associated with using large amounts of alloying elements and the decreased weldability observed in second-generation AHSS. A notable type among these steels is MMn steels, which contain approximately 3-12% Mn, 0.05-0.6% C, 0-3% Si, and 0-6% Al [35]. A lightweight material not only reduces the weight of the BIW but also minimizes the risk for both the passengers inside and those around the vehicle [31]. The BIW structure, designed using multiple materials, has enhanced performance while successfully reducing both weight and cost. By utilizing a combination of extrusion, casting, and pressed aluminum and steel parts, stiffness has been maximized, and weight has been minimized. Selecting multiple materials for BIW production provides the best optimization in terms of material cost and strength, rather than using a single material for the entire body. The use of a multi-material approach has resulted in a 35% reduction in the vehicle body's weight [19].

The use of aluminum in the automotive industry has steadily increased over the years. In the North American market, the use of aluminum per vehicle increased from 154 kg in 2010 to 208 kg in 2020, and it is expected to reach 258 kg by 2030. This increase is primarily due to the growing use of aluminum in areas such as BIW, closures, and chassis components [37].

It is particularly observed that the use of aluminum (alloy, casting, extrusion) and hybrid metals is becoming increasingly widespread. While the use of soft metals is decreasing, the utilization of AHSS steel and

composite materials is on the rise.

According to a statement by the World Steel Association (WSA), the types of steel used in BEVs vary depending on technology and needs. It is predicted that in future EVs, 48% of the steel used will be next-generation materials with over 1000 MPa, which will directly impact production methods, and the equipment used [38]. In terms of weight reduction using steel and aluminum materials, the use of hydroformed structures and Tailored Blanks has been shown to provide a 25% weight reduction compared to a standard vehicle. Additionally, lightweight aluminum usage offers a 50% weight reduction [39].

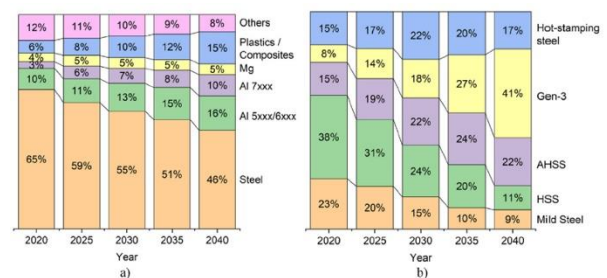


Figure 2.7 General materials used in BIW(a) and the ratio of steel materials over the years (b) [35]

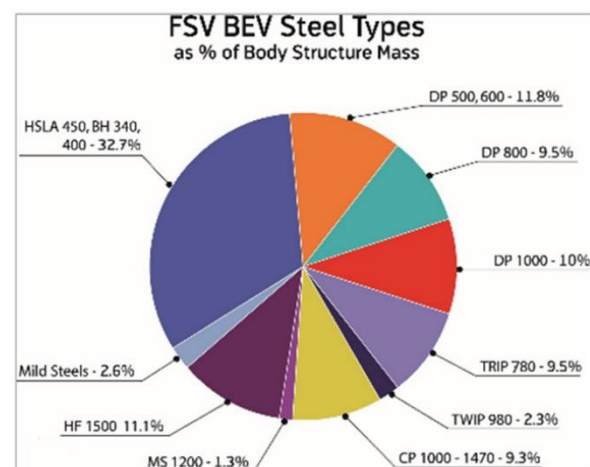


Figure 2.8 Steel types used in BEVs [38]

Studies have explored carbon fiber parts and carbon fiber-reinforced polymers to provide ultra-lightweight solutions, enhance crash performance, and achieve better acoustic properties [40]. The use of polymeric materials, despite a 14% cost increase, has reduced weight by 51% and improved performance by 10%. Carbon Fiber Reinforced Polymer (CFRP) has been successfully investigated for application in lightweight body structures for electric vehicles. The microstructure model of carbon fiber fabric has been examined, and the properties in each axis

have been defined. These properties were then applied to the Finite Element Analysis (FEA) package, and the entire body structure was analyzed under various loading and impact conditions, resulting in improved crash resistance. This CFRP structure achieved 28% weight savings compared to Glass Fiber Reinforced Polymer [19].

3.Results and Discussion

3.1. Transition from ICE to BEV platforms

The transition from ICE platforms to BEVs has presented challenges, particularly around battery protection. Passenger safety has always been a priority that drives the scope of engineering improvements. Continuous development has been an ongoing effort across various areas of the vehicle, from the advancement of AHSS for structural components to specially designed crumple zones and airbags.

The addition of batteries in BEVs has introduced the need to protect the battery pack from both overheating and intrusion. Although each automaker has developed its own unique approach, most have positioned the batteries in modules and placed them at the lowest level of the vehicle. Automakers have focused their efforts on reducing the risk of intrusion and crashing in the event of an accident. Manufacturers have implemented various design improvements in line with these primary objectives during the BEVs transition process.

3.1.1 EV body front-end modifications

According to the figure above, 6000 series aluminum extrusion plates are used in region 1, while AHSS is applied in regions 3 and 4. At this point, the modifications made to the front provide a 10% deformation advantage during a collision compared to an ICE vehicle. The front bumper beam has been extended laterally (along the Y-axis) and its cross-sectional width has increased compared to ICE vehicles. Collision boxes have been added to the front bumper attachment to reduce impact during a crash. The connection parts between the front bumper and the upper body have been extended to increase load transmission. Bolt connections have been added to the front door hinge pillar to increase load capacity [41].

One of the efforts to minimize the impact of damage in the front-end sections of ICE and BEVs has been to increase the number of front bumper support barriers. This application has been implemented on the Volvo XC40 model.



Figure 3.1 Ford Mustang Mach-E front support component modifications [41]

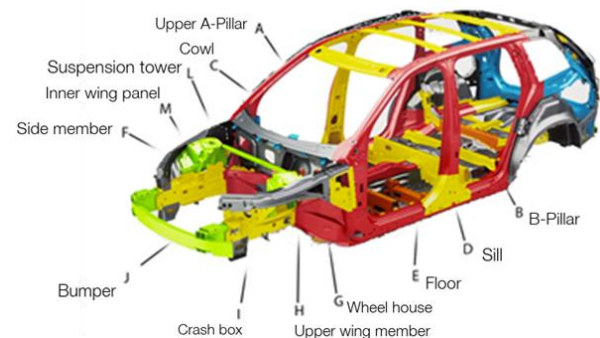


Figure 3.2 Volvo XC40 BIW Representation [10]

Three innovations stand out when compared to ICE vehicles. The front bumper support group extended using aluminum extrusion, the AHSS steel connection group establishing a link between this group and the vehicle's lower chassis frame, and the aluminum extrusion connection brackets. As part of the studies conducted, there are other investigations that directly affect both the vehicle's range and weight.



Figure 3.3 Magnesium alloy cross bar production via die casting method [42]

The example of a magnesium cross bar produced by "GF Casting Solutions" using the die casting method is shown in Figure 4.3 above. Magnesium alloy provides a lightweight advantage of 37% compared to aluminum [42].

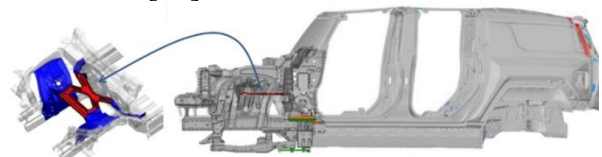


Figure 3.4 Addition of front support bracket for GM

Hummer BEVs [42]

GM has added a "K bracket" in the vacant area on the front engine side of the ICE to enhance the front strength of the Hummer BEV model. This not only provides support for the trunk located at the front of the BEV but also acts as a shock absorber, reducing the impact that may reach the front panel on the driver's side [42].

3.2. EV body mid-side body modifications

Within the scope of BEV, particularly considering impact resistance, side impacts pose a greater threat to the battery group compared to the front and rear sections of the vehicle. New methods and designs that combine lightweight with robustness and safety elements are being applied to vehicles by manufacturers. The traditional material used in the B-pillar of a lightweight utility vehicle is low-carbon steel, which offers strong safety performance at a relatively low material cost. However, steel can be heavy compared to lightweight composites and metals, leading to higher fuel consumption during vehicle operation. Opportunities for reducing the weight of the B-pillar involve replacing steel with alternative materials such as advanced high-strength steel, fiber-reinforced polymer composites, and aluminum [43].

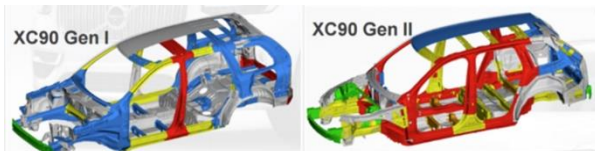


Figure 3.5 Volvo XC90 ICE B-Pillar replacement [10]

Volvo has implemented Tailor Welded material in the Center pillar component of the XC90 vehicle, which is equipped with an internal combustion engine, in its second-generation body design. Sheets with different material properties and thicknesses have been combined to form the B-pillar. This method is also applied in the XC40 model, which is the first-generation EV model.

Audi has implemented a "soft zone" application on the B-Pillar. In this application, the base of the 1500 MPa hot-pressed B-pillar body is made of 550-650 MPa AHSS steel. Due to its ability to dampen side impacts and the weight reduction in the relevant part, this design is also planned for use in future BEVs [44].

Ford has utilized 1500-1700 MPa three-part martensitic roll-formed sheet material in the Mach-E model. This material is connected to the main body using a bolt connection method, positively contributing to energy damping. Additionally, to achieve both lightness and strength, vehicle manufacturers are applying the aluminum extrusion method [41].

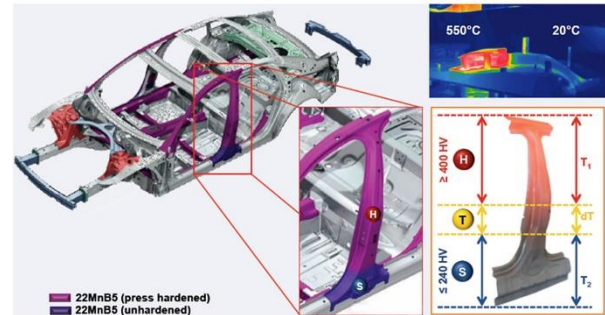


Figure 3.6 Audi soft zone B-Pillar [44]



Figure 3.7 Ford Mach-E Rocker design changes [41]

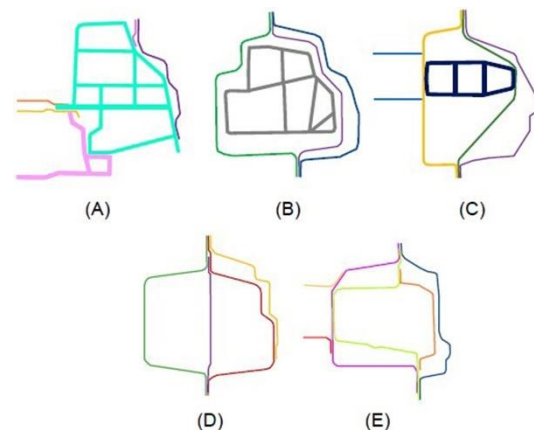


Figure 3.8 BEVs Rocker designs [45]

The above image shows the schematic representations of aluminum extrusion panels used as vehicle rocker panels. The structures indicated by A, B, and C represent multi-chamber aluminum extrusion structures, while D and E illustrate sheets with different thicknesses and strength values that are pressed together. In the component development studies, analyses have shown that the rocker part is examined in two main sections: energy damping and battery protection, depending on the manufacturing method. The homogeneity of structures in aluminum extrusion and the ability to alter pore numbers through design changes provide

advantages for vehicle manufacturers. Additionally, the combination of different sheets with various thicknesses and strengths to create damping and protection layers is seen as a continuation of the ICE production method. However, regardless of the method applied, the primary goal is to achieve maximum lightness in the vehicle while ensuring safety [45].

3.3. EV body floor structure modifications

During the transition from ICE to BEV, one of the most notable changes in vehicle body components occurs in the central floor section. With the removal of the driveshaft tunnel in 2nd-generation EVs, which was present in 1st-generation EVs, battery and battery pack designs are playing an increasingly active role in ensuring the structural integrity of the vehicle body.



Figure 3.9 Vehicle floor structure design (Left: Monocoque body, Center: Body-on-frame, right: Skateboard architecture) [12,46,47]

As battery designs have evolved, the vehicle's floor structure has also undergone significant changes. The use of a skateboard-type frame structure has become more prevalent between 1st- and 2nd-generation BEVs. Brands such as Audi e-tron, Nissan Leaf, Chevrolet Bolt, Tesla Model S, and Jaguar I-Pace have started adopting this method as part of their battery protection strategies. Various design modifications have been implemented by manufacturers to integrate the battery into the vehicle and ensure its safety [48].

The most significant difference in the design of the Jaguar I-Pace is the use of a front bumper support block with a 45-degree angled structure, compared to the 90-degree connection to the main body in ICE vehicles. This block also houses the torque box. At the rear, a similarly angled body design helps to evenly distribute the shock across the body in the event of a crash. The rear torque box is integrated into the system from the area indicated in section 2 of the figure.

Additionally, the side rocker panels are broader in design.

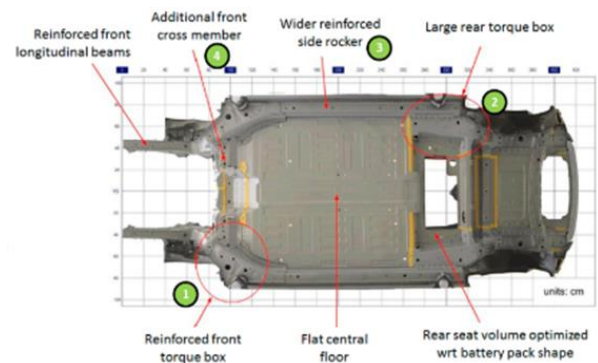


Figure 3.10 Jaguar I-Pace floor structure (Left: ICE, right: BEVs) [48]



Figure 3.11 Ford Mach-E ICE-BEVs floor structure comparison [41]

The floor geometry used in the Jaguar I-Pace model is also observed in the Ford Mach-E model. The front support panels connect to the rocker panel by enclosing the torque box in a monoblock structure.

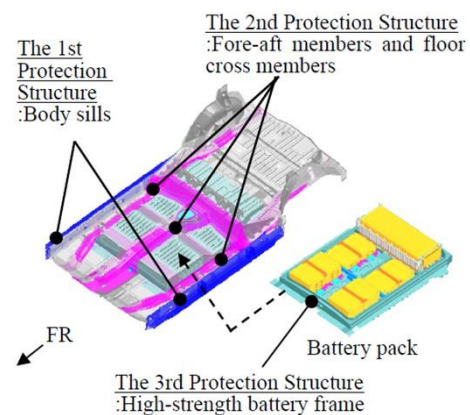


Figure 3.12 Central floor structure connections [49]

When examining the central floor structure connections, it can be seen that protective cross members made of UHSS steel surround the battery. In addition to these connections, the rocker design is also optimized to provide a protective layer for the battery pack. In vehicles with internal combustion engines, the floor structures typically use 600-980 MPa steel sheets; however, for battery protection, these have been replaced with lighter yet stronger 1300-2000 MPa steel materials. Since 2019, VW's electric vehicle ID.3 has featured two seat cross members made from MBW 1900 steel, as seen in Figure 4.13. These

components are part of the MEB platform (Modularer E-Antriebs-Baukasten) and can be used in other electric vehicles in the VW Group. MBW 1900 is the trade name for a press-hardened steel with a tensile strength of 1900 MPa. A properly designed MBW 1900 B-pillar can provide 22% weight savings compared to a Dual-Phase (DP) 600 design and is 9% less costly than the original Dual-Phase design [51].

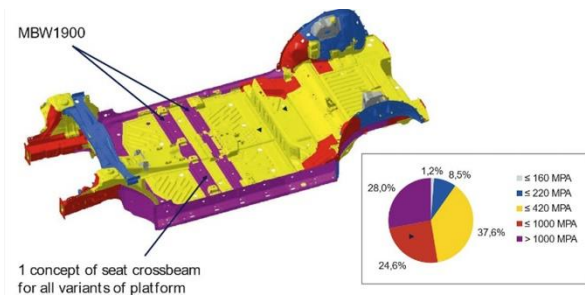


Figure 3.13 Sheets used in the Volkswagen ID.3 platform's floor structure [50]

Ford has also demonstrated that using MBW 1900 instead of PHS 1500 can lead to 15% more weight savings [52]. In line with the design of 2nd-generation BEVs, alternative materials have also been tested in the top and bottom protective plates of battery packs. While 1st-generation BEVs used soft steel battery pack plates, the increasing need for safety and vehicle integrity has shown that Dual-Phase steels make much more positive contributions in 2nd-generation BEVs.

3.4 Production Methods

Advancing technology has positively contributed to the change in manufacturing methods of vehicle chassis parts during the transition from ICE vehicle to BEVs. Some of these methods include aluminum casting, mega casting, patchwork, and new laser welding methods.

3.4.1 Aluminum casting

Aluminum is one of the three most widely used metals in modern society due to its excellent properties such as lightness, good electrical and thermal conductivity, high strength, corrosion resistance, and easy machinability. Aluminum is often alloyed with other elements [53]. Over the past decade, studies aimed at energy savings have revealed that the production of light and economical vehicles plays a significant role in reducing fuel

consumption. Aluminum alloys are widely preferred in the construction of passenger cars, buses, and especially maritime applications such as trains [54]. Casting aluminum alloys is quite common and are increasingly finding more applications in modern industry. According to various estimates, 20-30% of all aluminum products produced worldwide are used as aluminum castings [55]. With CO₂ emissions becoming a significant issue in the automotive sector, the properties of aluminum alloys, such as energy and fuel savings, as well as lightness, have been emphasized. The largest volume of aluminum components in vehicles includes cast aluminum for engine blocks, cylinder heads, and chassis parts [56]. New aluminum casting techniques offer improved material properties and functional integration to meet the desired requirements. This trend is driven by the need for automotive manufacturers to significantly reduce the weight of powertrain and chassis components. Additional features to improve vehicle performance may lead to an unacceptable increase in vehicle weight [57]. Significant weight reduction can be achieved in smaller but high-volume compact vehicles through the use of aluminum casting, which is already widely used in high-end car engines [56].

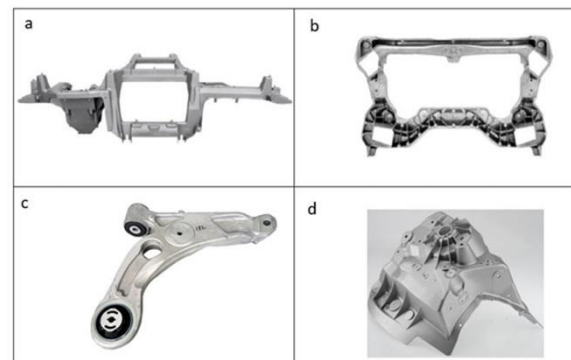


Figure 3.14 Examples of aluminum cast structural parts: cross car beam (a), engine cradle (b), control arm (c), shock tower (d) [58]

Since 1997, high-vacuum aluminum casting technology, which provides weight savings, has been applied in vehicle body structures despite increasing vehicle weights due to market forces beyond fuel economy. Using lightweight aluminum casting technology for net weight reduction is likely to contribute significantly to fuel economy at a reasonable cost. The wider application of aluminum castings and the weight savings achieved

through best design practices have been demonstrated in the MMLV (Multi-Material Lightweight Vehicle) program. The MMLV body structure was a good engineering exercise in using commercially available different structural materials, forming operations, and joining techniques for engineers. Overall, high-pressure vacuum aluminum castings offer the possibility of lower mass, part integration, and fewer assembly processes [59].

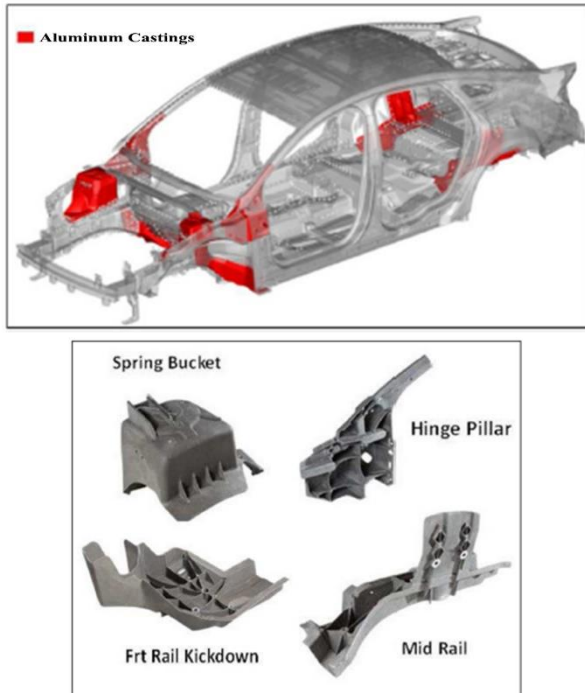


Figure 3.15 MMLV body aluminum casting parts [33]

The eight castings in the MMLV consist of the front shock tower, hinge pillar, kick-down rail, and rear mid-rail castings on the left and right sides. Most of the aluminum castings in the MMLV are mechanically joined to steel materials using a structural adhesive. The most commonly used method for such connections is SPR (Self-Piercing Rivets).



Figure 3.16 Example of a SPR [33]

SPR is a cold mechanical joining process in which a rivet passes through the top sheet or both the top and intermediate sheets and locks into the bottom sheet with the help of a suitable die. SPR is currently the primary method used

in the assembly of lightweight automotive structures made from aluminum and composite materials. SPR emerged half a century ago but has made significant progress in the last 25 years due to the automotive industry's need to join lightweight materials, especially aluminum alloy structures, aluminum-steel structures, and other composite materials [59]. The automotive industry is the largest consumer of aluminum casting alloys, where they are used in various components such as engine blocks and transmissions in ICE vehicles and BEVs. Additionally, the urgent need for the transition to carbon neutrality is accelerating trends in weight reduction (lightweighting) that contribute to energy savings and the reduction of greenhouse gas emissions in the automotive industry. The application of lightweight materials in automobiles, combined with increasing electrification, will lead to changes in the demand for processed and cast alloys in the near future [60].

3.4.2 Mega-giga casting

Numerous studies have demonstrated that the use of aluminum in lightweight vehicles has been increasing for decades. Specifically, it has been observed that aluminum usage per vehicle has surpassed 227 kg in North America and 180 kg in Europe. Although casting has been the dominant product form until now, in recent years sheet and extrusion applications are expected to show the highest growth rates [61]. The primary reason for using aluminum has always been to achieve weight reduction. However, higher aluminum content, particularly in sheet metal and extrusion assemblies, also translates into higher costs. Moreover, if primary aluminum is being used, it results in a higher carbon footprint. Original equipment manufacturers (OEMs) and their suppliers are working to reduce the material and processing costs of their components, improve production quality, and enhance sustainability—meaning, increasing the recycled content in all types of aluminum parts [62].

In the automotive industry, trends have emerged among OEMs toward producing Mega-Cast body components. As of May 5, 2024, Tesla and Volvo have shown on their

websites that they are adopting approaches to producing Mega-Cast aluminum components in the underbody of their vehicles [63]. In 2018, the electric car manufacturer Tesla patented Mega-Casting, making it possible to produce an entire car body in one operation using aluminum high-pressure die casting (HPDC) in the future [64]. The aim of this invention is to reduce operating, production, and tooling costs, along with cycle time. Other companies planning to use Mega-Casting include Mercedes-Benz, which refers to this technology as “Bionic Cast,” as well as Chinese OEMs XPeng and Nio [63].

In recent years, with the trend initiated by Tesla, giga-castings (referred to as “mega-castings” by some OEMs) have started to be used in BEVs components. With this method, it is possible to combine many parts used in the vehicle body into a single component [61]. Examples of this application can be seen in Tesla’s Model Y. In Figure 3.17 below, the design of the front and rear body parts of the Tesla Model 3 and Model Y is shown.



Figure 3.17 Giga casting example: TESLA Model 3 (left) – Model Y (right) [58]

Compared to the Model 3, these two castings replaced 171 parts and 1,600 welds, removing 300 robots from the assembly line, which significantly reduced the necessary capital investment and floor space. Additionally, it made a significant contribution to lowering the logistical costs and carbon footprint associated with the 171 parts [58].

Recently, Volvo and the premium electric vehicle brand Polestar have adopted giga-presses, also referred to as mega-castings, and begun using this technology. As shown in Figure 3.18, Volvo plans to use this technology to create a single-piece mega-cast aluminum base [58].

The mega-cast bases for Volvo’s next-generation BEVs will already be designed to include mounting points for parts like suspension arms and electric motors, which will eliminate the need for a rear subframe. Compared to using methods like welding

multiple small parts in chassis production, mega-casting is expected to enable the production of monolithic chassis components. This way, many additional steps in the assembly phase are removed, aiming to reduce costs and provide energy-efficient vehicles. German automaker Mercedes-Benz is targeting maximum cost and weight reduction (enabled by mega-casting) to extend the electric vehicle range by managing energy consumption [58].

There are several brands that either following this method or have announced plans to do so. Among these brands are Mercedes-Benz, Volkswagen, Toyota, General Motors, Hyundai, and Chinese BEVs manufacturers Nio and Xpeng.



Figure 3.18 Volvo mega-casting example [58]

3.4.3 Patchwork and BEVs relationship

Today, reducing the weight of components in the aerospace and automotive industries has become a crucial step toward lowering gas emissions and fuel consumption. One of the most commonly used manufacturing processes is sheet metal forming, and in this process, continuous optimization is carried out regarding the weight, strength, and thickness of the formed sheets. For this purpose, designers need to predict the strain limits and localized necking of the formed part; this subject has been extensively studied in the scientific literature [65]. With environmental issues becoming increasingly severe, energy conservation and environmental protection have become two critical problems that need to be addressed in the automotive industry. Patchwork hot forming technology can be used to produce lightweight and high-strength parts, and it is increasingly being applied in the production of automotive body components. Since the main sheet and the patchwork sheet must be joined with spot welds before forming,

the arrangement of these weld points has a significant impact on the formability of part [66].

In recent years, to enhance crash safety, it has become necessary to design special components with segmentation of strength and toughness in some structural parts made of boron steel. Patchwork hot forming technology is a new method that offers good applicability and low-cost advantages, and it is being increasingly used in the production of such special components. Currently, the primary welding methods used in patchwork hot forming are resistance spot welding, laser welding, and arc welding [67]. Considering automotive manufacturing costs and efficiency, resistance spot welding is a widely used joining method. In the patchwork sheet hot forming, the main sheet and the patchwork sheet are first joined by spot welding, and then both are heated and hot-formed together. As a result, patchwork parts with a specific segmentation of strength and toughness are obtained [66]. In patchwork sheets, one or more “patch sheets” (reinforcements) are superimposed on a “main sheet” and joined by spot welding. These spot-welded sheets are then heated in a furnace and hot-formed in a single operation. The final part will have increased thickness in the areas of interest. As shown in Figure 5.6, patchwork sheets can reduce the need for reinforcement assemblies after forming.

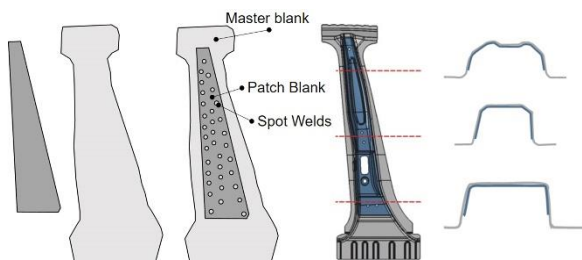


Figure 3.19 Geometries of the main blank and patch for the B-pillar: (a) before, (b) after the spot welding process, (c) after hot forming [68]

Since the spot welds in the patchwork process are also austenitized and annealed, the hardness distribution is generally better than that of spot welds made after hot forming [68]. Overlap patch blanks are a subset of patch sheets. As shown in Figure 3.20, instead of a shaped main sheet and bracket, two (or more) flat sheet sub-parts are joined over the “overlap zone” using the spot welding method, creating

a structure like a specially laser-welded part. This technology was initially applied to cold-formed components [69].

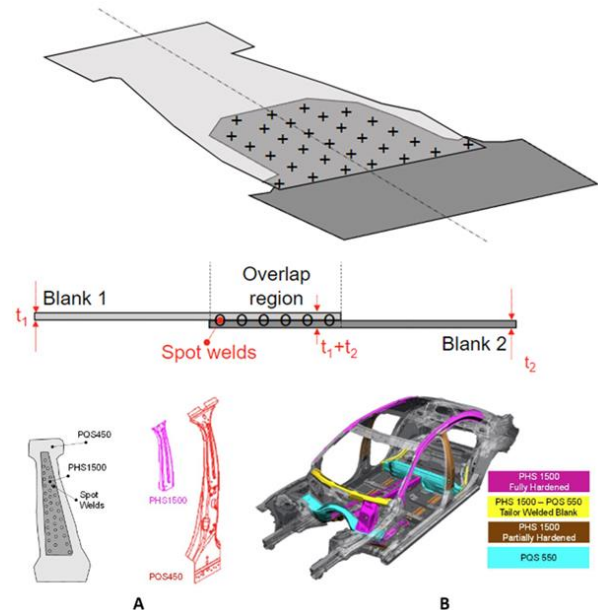


Figure 3.20 Overlapped patch sheet welding (a) and Jaguar I-Pace B-pillar (b) [70,71]

The B-pillar reinforcement of the Jaguar I-PACE, an aluminum-intensive electric SUV introduced in 2018, was made from a patchwork sheet. Unlike previous applications, the main sheet was made of PQS450, which can be easily added to the rest of the vehicle through mechanical joining. The patch was made of PHS1500, improving side impact and roof crush performance [71].

In the automotive sector, many companies, including Honda, Volvo, Jaguar, Ford, and Mercedes, are known to apply the patchwork method to produce high-strength lightweight body parts, reducing the need for spot welding processes, thereby achieving cost and equipment savings. This method also plays a significant role in the global reduction of greenhouse gas emissions.

3.4.4 Laser screw welding

Elements such as formstly, reliability, and chassis stiffness, which form the basis of vehicle performance, play a crucial role in the assembly of the vehicle body’s structure. Most of these assembly processes are carried out with spot welding. However, due to current distribution, it is not possible to shorten the welding intervals, limiting the number of joining points, and it is difficult to fully reveal the strength and stiffness of the structural

components. The LSW (Laser Screw Welding) technology developed by Toyota was introduced to resolve the problem of narrow plate gap tolerance, which was previously an issue with laser welding technology. By applying laser welding to the vehicle body's structure, the goal is to enhance vehicle performance [72].

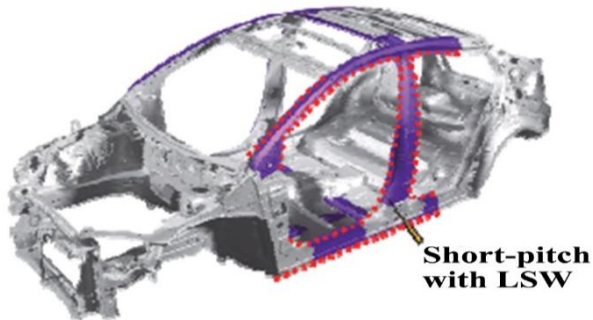


Figure 3.21 Toyota factory Lexus LSW application method [73]

In 2011, the LSW process was integrated into Toyota's Lexus production factory, adding approximately 150 LSW welding points, thus commercializing this technology as a means to enhance driving stability and comfort. From the early stages of development, the primary purpose of LSW has been to renew the structural integrity and improve vehicle performance, such as crash safety [73].

LSW is approximately three times faster than traditional spot welding and can be applied throughout the vehicle. Replacing some of the thousands of spot welds in a vehicle structure with LSW can increase productivity. The welding process in the vehicle chassis with LSW can be shortened by up to 40% by replacing the spot welds with LSW. The main objective of LSW development is to enhance the fundamental performance of the vehicle structure. LSW is also used flexibly between aluminum and steel materials on assembly lines. Toyota claims that thanks to the versatility and speed of this technology, assembly line length has been reduced by approximately 50%. This also brings with it a reduction in factory CO₂ emissions [73].

4. Conclusions

The ongoing efforts to generate and store electrical energy from renewable energy sources, combined with advancements in automotive technology, have played a significant role in reducing fossil fuel

consumption and carbon footprints. These developments have contributed greatly to the transition from ICE vehicles to BEVs. Efforts to reduce the weight of electric vehicles, driven by the added weight of batteries, have opened the door to new technologies and the use of innovative materials in the automotive industry. It can be concluded that vehicle lightweighting is not only important for increasing battery range but also for enhancing fuel efficiency by reducing emissions and controlling pollution. The trend toward producing lighter vehicles has also necessitated changes in materials and manufacturing methods in the vehicle's welded underbody parts to meet safety standards. In particular, the integration of aluminum casting methods with giga-mega presses and the use of hot-formed sheet materials have demonstrated that electric vehicle dynamics can yield better results than the monocoque body structures of internal combustion engine vehicles. Emerging technologies, such as LSW, Patchwork, and Giga-Mega aluminum casting methods, are expected to facilitate the transition from internal combustion engine vehicles to electric vehicles by offering advantages in lightness, durability, cost efficiency, and safety, while also enabling longer ranges and more environmentally friendly features.

Declaration of Competing Interest

The authors declare that they have no known competing financial interests or personal relationships that could have appeared to influence the work reported in this paper.

CRedit authorship contribution statement

Murat Onat: Conceptualization, Data curation, Formal analysis, Investigation, Methodology, Software, Validation, Visualization, Writing – original draft, Writing – review & editing.

5. References

1. D. Maresch and J. Gartner, "Make disruptive technological change happen - The case of additive manufacturing," *Technol. Forecast. Soc. Change*, vol. 155, p. 119216, 2020. <https://doi.org/10.1016/j.techfore.2018.02.009>
2. Yong J, Ramachandaramurthy VK, Tan KM, Mithulananthan N. A review on the

state-of-the-art technologies of electric vehicle, its impacts and prospects. *Renewable and Sustainable Energy Reviews*. 2015;49:365-385.

<https://doi.org/10.1016/j.rser.2015.04.130>

3. Molina-Ibáñez EL, Rosales-Asensio E, Pérez-Molina C, Mur Pérez F, Colmenar-Santos A. Analysis on the electric vehicle with a hybrid storage system and the use of superconducting magnetic energy storage (SMES). *Energy Reports*. 2021;7(Suppl. 5):854-873.

<https://doi.org/10.1016/j.egy.2021.07.055>

4. Sabonnadière JC, editor. *Renewable Energies*. London (UK), Hoboken (USA): ISTE, John Wiley & Sons; 2009.

5. Guarnieri M. Looking back to electric cars. In: *Proceedings of the 3rd IEEE History of Electrotechnology Conference (HISTELCON '2012)*; 2012 Sept 5-7; Pavia, Italy.

6. Davenport T. Improvement in propelling machinery by magnetism and electro-magnetism. US patent 132A. 1837 Feb 25.

7. Rahman M, Wang X, Wen C. A review of high energy density lithium-air battery technology. *J Appl Electrochem*. 2014;44:5–22.

8. Chang C. Factors affecting capacity design of lithium-ion batteries. *Batteries*. 2019;5:58.

9. Ntombela M, Musasa K, Moloji K. A comprehensive review for battery electric vehicles (BEV) drive circuits technology, operations, and challenges. *World Electr Veh J*. 2023;14:195.

<https://doi.org/10.3390/wevj14070195>

10. Enriquez J. Body in white architecture for an electric vehicle concept [Master's thesis]. Chalmers University of Technology, Sweden; 2016.

11. Davis G. *Materials for Automobile Bodies*. ISBN: 978-0-08-096979-4, 2012.

12. Pradeep SA, Pilla S. *Applied Plastics Engineering Handbook*. 2nd ed., 2017.

13. Zhang J, Hu S, Guo X, Zhou Q. Multidisciplinary Design Optimization of BEV Body Structure. *SAE Technical Paper 2015-26-0229*, 2015.

<https://doi.org/10.4271/2015-26-0229>.

14. Liu B, Zhan Z, Zhao X, Chen H, et al.

A Research on the Body-in-White (BIW) Weight Reduction at the Conceptual Design Phase. *SAE Technical Paper 2014-01-0743*, 2014. <https://doi.org/10.4271/2014-01-0743>.

15. European Aluminium Association. *The aluminium automotive manual*. Version 2013. European Aluminium Association; 2013.

16. Léost Y, Boljen M. Crash simulations of electric cars in the EVERS SAFE project. In: *XIII International Conference on Computational Plasticity: Fundamentals and Applications (COMPLAS XIII)*. Fraunhofer Institute for High-Speed Dynamics, Ernst-Mach-Institut (EMI), Freiburg, Germany; n.d.

17. E. G. Vogt, L. Gebel, C. Meyer, M. Mennenga, and C. Herrmann, "Methodology for qualifying the use of green steel in body components: A contribution to the life cycle engineering of steel," *Procedia CIRP*, vol. 122, pp. 473–478, 2024.

<https://doi.org/10.1016/j.procir.2024.01.069>.

18. Hao H, Wang S, Liu Z, Zhao F. The impact of stepped fuel economy targets on automaker's light-weighting strategy: The China case. *Energy*. 2016;94:755-765.

<https://doi.org/10.1016/j.energy.2015.11.051>.

19. Shinde P, Ravi K, Nehru N, Pawar S, et al. Light Weight BIW Solutions for Improving Functional Properties: A Review. *SAE Technical Paper 2016-01-8138*, 2016. <https://doi.org/10.4271/2016-01-8138>.

20. Kelly JC, Elgowainy A, Isaac R, Ward J, Islam E, Rousseau A, Sutherland I, Wallington TJ, Alexander M, Muratori M, Franklin M, Adams J, Rustagi N. *Cradle-to-Grave lifecycle analysis of U.S. light-duty vehicle-fuel pathways: A greenhouse gas emissions and economic assessment of current (2020) and future (2030-2035) technologies (ANL-22/27 Rev.1)*. Argonne National Laboratory; 2020.

21. Lewis A, Keoleian G, Kelly J. The Potential of Lightweight Materials and Advanced Combustion Engines to Reduce Life Cycle Energy and Greenhouse Gas Emissions. *SAE Technical Paper 2014-01-1963*, 2014. <https://doi.org/10.4271/2014-01-1963>.

22. Muttana S, Mubashir S. Lightweighting of Passenger Cars: A Comparative Lifecycle Analysis of Energy Consumption and CO2 Emissions. *SAE Technical Paper 2013-26-0072*, 2013.

<https://doi.org/10.4271/2013-26-0072>.

23. Li L, Sandu C. On the impact of cargo weight, vehicle parameters, and terrain characteristics on the prediction of traction for off-road vehicles. *Journal of Terramechanics*. 2007;44:221-238.

<https://doi.org/10.1007/s11044-006-9007-5>.

24. Sun, Z., Premarathna, W. A. A. S., Anupam, K., Kasbergen, C., & Erkens, S. M. J. G. (2024). A state-of-the-art review on rolling resistance of asphalt pavements and its environmental impact. *Construction and Building Materials*, 411, 133589.

<https://doi.org/10.1016/j.conbuildmat.2023.133589>

25. Abdullah, M., Idros, S., Toha, S. F., & Md Said, M. S. (2024). Modelling of Vehicle Longitudinal Dynamics for Speed Control. *Journal of Advanced Research in Applied Mechanics*, 123(1), 56–74.

<https://doi.org/10.37934/aram.123.1.5674>

26. Candela, A., Sandrini, G., Gadola, M., Chindamo, D., & Magri, P. (2024). Lightweighting in the automotive industry as a measure for energy efficiency: Review of the main materials and methods. *Heliyon*, 10(8), e29728.

<https://doi.org/10.1016/j.heliyon.2024.e29728>

27. Shevket C, Re P, Ciulla L. Development of Low Friction and Light Weight Wheel Hub Units to Reduce Both the Brake Corner Un-Sprung Mass and Vehicle CO2 Emission - Part 2 - Weight Reduction. *SAE Int. J. Passeng. Cars - Mech. Syst*. 2011;4(3):1422-1431.

<https://doi.org/10.4271/2011-01-2375>.

28. An F, DeCicco J, Ross M. Assessing the Fuel Economy Potential of Light-Duty Vehicles. *SAE Technical Paper 2001-01-2482*, 2001. <https://doi.org/10.4271/2001-01-2482>.

29. Sithik M, Vallurupalli R, Lin B, Sudalaimuthu S. Simplified Approach of Chassis Frame Optimization for Durability Performance. *SAE Technical Paper 2014-01-0399*, 2014. <https://doi.org/10.4271/2014-01-0399>.

30. Hallas A, Carruthers J. Honeycomb Materials: A Solution for Safer, Lighter Automobiles. *SAE Technical Paper 2002-01-2113*, 2002. <https://doi.org/10.4271/2002-01-2113>.

31. Evans L. How to make a car lighter and

safer. *Traffic Safety*. 2004.

<https://doi.org/10.4271/2004-01-1172>.

32. Skaszek T, Zaluzec M, Conklin J, Wagner D. MMLV: Project overview. *SAE Technical Paper 2015-01-0407*, 2015. <https://doi.org/10.4271/2015-01-0407>.

33. Conklin J, Beals R, Brown Z. BIW design and CAE. *SAE Technical Paper 2015-01-0408*, 2015. <https://doi.org/10.4271/2015-01-0408>.

34. Lesh C, Kwiaton N, Klose F. Advanced high strength steels (AHSS) for automotive application – Tailored properties by smart microstructural adjustments. *Steel Research International*. 2017; 88(10):1700210.

<https://doi.org/10.1002/srin.201700210>.

35. Li J, Tong C, Zhang R, Shi Z, Lin J. A data-informed review of scientific and technological developments and future trends in hot stamping. *International Journal of Lightweight Materials and Manufacture*. 2024; 7(2):327-343.

<https://doi.org/10.1016/j.ijlmm.2023.11.003>.

36. China Society of Automotive Engineers. Annual evaluation of technology roadmap for energy saving and new energy vehicle 2019. Beijing: China Machine Press; 2020.

37. The Aluminum Association. Roadmap for automotive aluminum; 2022.

38. Czerwinski F. Current trends in automotive lightweighting strategies and materials. *Materials*. 2021; 14(21):6631. <https://doi.org/10.3390/ma14216631>.

39. Langerak N, Kragtwijk S. The application of steel and aluminum in a new lightweight car body design. *SAE Technical Paper 982285*, 1998.

<https://doi.org/10.4271/982285>.

40. Adam H. Carbon fibre in automotive applications. *Materials & Design*. 1997; 18(4-6):349-355. [https://doi.org/10.1016/S0261-3069\(97\)00076-9](https://doi.org/10.1016/S0261-3069(97)00076-9).

41. Mikolaiczik M. Ford's 2021 Mustang Mach-E. *Great Designs in Steel Symposium*; 2021. Track 1 - Session 1.

42. Seiter D, Veal Jr J, Dissler S, Perry W. GMC Hummer EV SUV body structure. Presented at: *Great Designs in Steel 2023 Symposium*; 2023; USA. Track 1 - Session 1.

43. Ivković D, Adamovic D, Arsic D, Ratkovic N, Mitrović A, Nikolić RR. Review

of the advanced high-strength steels used in the automotive industry: Review of advanced high-strength steels and their manufacturing procedures. *Mobility and Vehicle Mechanics*. 2023; 49(3):47-64.

<https://doi.org/10.24874/mvm.2023.48.03.04>.

44. Taylor T, Clough A. Critical review of automotive hot-stamped sheet steel from an industrial perspective. *Materials Science and Technology*. 2018; 34:1-53. <https://doi.org/10.1080/02670836.2018.1425239>.

45. Great design in Steel presentation. EV structure lightweight combo made of OLPB door ring wave rocker; 2023.

46. Sarmiento A, Luiz A, Pereira J, Barbieri C, Sakuramoto C. Body structure contribution for automotive energy efficiency improvement - INOVAR Auto program. *SAE Technical Papers*. 2013; 13.

<https://doi.org/10.4271/2013-36-0142>.

47. Kumar S, Verma A, Kumar K, Baburajan A. Skateboard chassis system with battery for a three-wheeler electric vehicle. *USD919026S1*; 2021 May 11.

48. Singh H. Body structure evolution from internal combustion engine to electric vehicles. In: *Global automotive lightweight materials*; 2019 Feb 20.

49. Uwai H, Isoda A, Ichikawa H, Takahashi N. Development of body structure for crash safety of the newly developed electric vehicle. 2011.

50. Lüken I, Tenneberg N. Volkswagen ID.3. Presented at: Aachener Karosserietage; 2019 Sep 17-18; Aachen, Germany.

51. Hoffmann O. Lightweight steel design in the modern vehicle body. In: *Werkstoff-Forum Intelligenter Leichtbau*; 2011; Hannover, Germany.

52. Lanzerath H. Simulation: Enabler for the efficient design of lightweight boron intensive body structures. Presented at: Insight Edition Conference; 2011 Sep 20-21; Gothenburg, Sweden.

53. Graedel TE, Reck BK, Miatto A. Alloy information helps prioritize material criticality lists. *Nat Commun*. 2022; 13:150. <https://doi.org/10.1038/s41467-021-27829-w>.

54. Zeytin H. Aluminum alloys and automotive applications in future. *MAM MKTAE Project Number: 50H5602*; 2000.

55. Criqui B. Proc. Int. SLC Conference on innovative developments for lightweight vehicle structures; 2009 May; Germany. p. 157.

56. Kaufman JG, Rooy EL. Aluminum alloy castings: properties, processes, and applications. ASM International; 2004.

57. Baser TA. Aluminum alloys and automotive applications. *Journal of Engineering and Machine*. 2012; 53(635):51-58.

58. Baser TA, Umay E, Akinci V. New trends in aluminum die casting alloys for automotive applications. In: *International Conference on Technology, Engineering and Science (IConTES)*; 2022 Nov 16-19; Antalya, Turkey. ISSN: 2602-3199; 2022. p. 79-87.

59. Li D, Chrysanthou A, Patel I, Williams G. Self-piercing riveting—a review. *International Journal of Additive Manufacturing Technology*. 2017; 92(7):1777–1824.

<https://doi.org/10.1007/s00170-017-0156-x>.

60. Wang B, Zhang Z, Xu G, Zeng X, Hu W, Matsubae K. Wrought and cast aluminum flows in China in the context of electric vehicle diffusion and automotive lightweighting. *Resources, Conservation and Recycling*. 2023; 191:106877.

<https://doi.org/10.1016/j.resconrec.2023.106877>.

61. Hartlieb A, Hartlieb M. The impact of giga-castings on car manufacturing and aluminum content. *Light Metal Age: The International Magazine of the Aluminum Industry*. 2023; 18. p. 1-3. June 12, 2023.

62. Hart C, Afseth A, Zuidema B. Aluminum value in battery electric vehicles. *The Aluminum Association*; 2022.

63. Burggräf P, Bergweiler G, Kehrer S, Krawczyk T, Fiedler F. Mega-casting in the automotive production system: Expert interview-based impact analysis of large-format aluminium high-pressure die-casting (HPDC) on the vehicle production. *Journal of Manufacturing Processes*. 2024; 124:918-935. <https://doi.org/10.1016/j.jmapro.2024.06.028>.

64. Schuh G, Fiedler F, Bergweiler G, Dworog L. Chancen und Risiken von Mega-Casting in der Fahrzeugproduktion - Die Karosserie aus dem Aluminium-Druckguss. *wt Werkstattstechnik online*. 2022; 112:580-585.

<https://doi.org/10.37544/1436-4980-2022-09-52>.

65. Sorrentino L, Parodo G, Giuliano G. Lightweight structures: An innovative method to uniform the thickness of metal sheets by patchwork blanks. *International Journal of Lightweight Materials and Manufacture*. 2022; 5(1):20-28.

<https://doi.org/10.1016/j.ijlmm.2021.08.003>.

66. Li W, Zhang Z, Jia H, Ren M. The optimization of welding spots' arrangement in A-Pillar patchwork blank hot stamping. *Metals*. 2023; 13:1409.

<https://doi.org/10.3390/met13081409>.

67. Yang J, Xiao M, Wu L, Li Z, Liu H, Zhao Y, Guo W, Tan C. The influence of laser power on microstructure and properties of laser welding-brazing of Al alloys to Al-Si coated 22MnB5 steel. *Optics & Laser Technology*. 2023; 162:109318.

<https://doi.org/10.1016/j.optlastec.2023.109318>

68. Lei C, Xing Z, Xu W, Hong Z, Shan D. Hot stamping of patchwork blanks: Modelling and experimental investigation. *The International Journal of Advanced Manufacturing Technology*. 2017; 92:Article 10.1007/s00170-017-0351-9.

69. Pinard F, Cretteur L, Sener JY. State of the art regarding design, modeling and processing of spot-welded patched blanks for the automotive industry. In: *Proceedings of the 2004 International Deep Drawing Research Group (IDDRG) Conference*; 2004; pp. 174–181.

70. Bodin H. Method of hot-shaping and hardening an object from a metal sheet, and a B-pillar for a vehicle. US Patent US10155545B2; 2018.

71. Black S, Rowlings S, Dietrich C. Jaguar I-PACE. Presented at: EuroCarBody; 2018 Oct 16-18; Bad Nauheim, Germany.

72. Koreishi T, Makino J, Ogura S, Kumagai T, Cheng M. レーザー円形走査溶接法を用いた車体骨格開発 [Development of Vehicle Body Structures Using Laser Circular Scanning Welding Method]. *Toyota Technical Review*. 2018; 64(122). ISSN: 0916-7501.

73. Lane M. Auto body technologies: A look into Toyota / Lexus welding methods on the production line. PanelTalk. 2018 Dec; 64-

67. Technical Report I-CAR New Zealand.